CHAPTER IV

RESULT AND DISCUSSION

4.1 Synthesis of the SWCNTs by laser ablation

Referring to many experimental results reported in other previous works, this part has set its aim to study effect of synthetic parameters on the morphology, size and purity of the airborne SWCNTs synthesized by Nd:YAG pulsed laser ablation of C/Ni/Co rod. Effect of laser intensity and synthesizing temperature on the morphologies, size and purity of the synthesized SWCNTs were thoroughly investigated and then reported and discussed in this part.

4.1.1 Effect of laser intensity

In this part, the effect of the laser intensity at the intensity of 0.4, 0.5 and 0.6 W on morphology, particle size distribution and crystallinity of the synthesized carbon nanoparticles in aerosol was studied under the same condition of nitrogen flow rate of 1.5 L/min, temperature of 25°C and atmospheric pressure.

The morphology of the synthesized carbon nanoparticles at different laser intensities of 0.4, 0.5 and 0.6 W was shown in Figure 4.1. Agglomerated primary carbon nanoparticles without fibrous particles could be clearly observed although the laser intensity was increased.

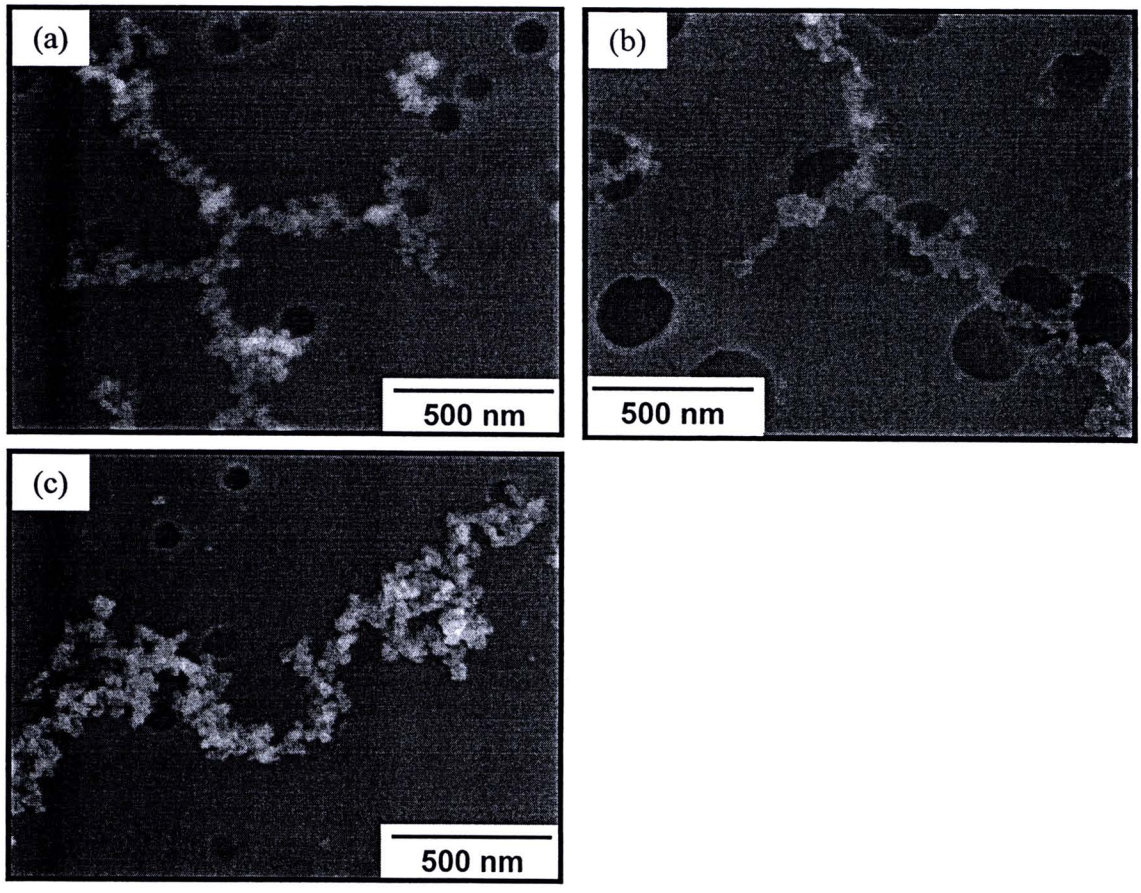

Figure 4.1 SEM images of the synthesized carbon nanoparticles at different laser intensities: (a) 0.4 W, (b) 0.5 W and (c) 0.6 W.

The size distributions based on electrical mobility of the agglomerated carbon nanoparticles synthesized at the laser intensity of 0.4, 0.5 and 0.6 W as shown in Figure 4.2 are similar normal curve with nearly same average sizes about 100 nm. At the laser intensity of 0.4 W, the number concentration of the synthesized carbon nanoparticles was 10.8×10^4 particles/cc. While at higher laser intensity the concentration was significantly increased. The number concentrations of the synthesized carbon nanoparticles were 31.0×10^4 and 35.6×10^4 particles/cc at the laser intensity of 0.5 and 0.6 W, respectively.

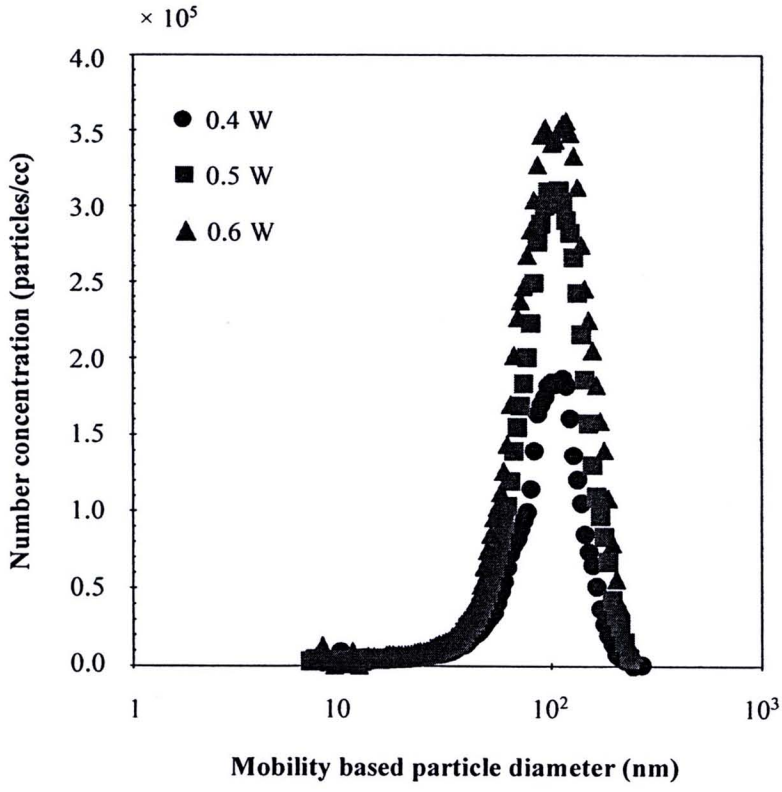

Figure 4.2 Size distributions of the agglomerated carbon nanoparticles synthesized at different laser intensities: (a) 0.4 W, (b) 0.5 W and (c) 0.6 W.

Similarity of the mobility size distributions was considered to be corresponding to the similarity of generated any fibrous particles as shown in the typical SEM images. From the relation of the images and size distributions, we could conclude that increasing the laser intensity while the controlled temperature at 25 °C did not effect on the morphology, which carbon nanoparticles were only formed, but effect on the concentration of the synthesized carbon nanoparticles.

Raman spectrum of the agglomerated carbon nanoparticles synthesized at the laser intensity of 0.6 W as shown Figure 4.3 shows its strong responses at about 1,590 cm^{-1} from graphitic bonding in crystalline carbon which known as G peak, and another peak at about 1,350 cm^{-1} from disorder and defective carbon which known as D peak. The I_D to I_G ratio of the carbon nanoparticles was 0.81.

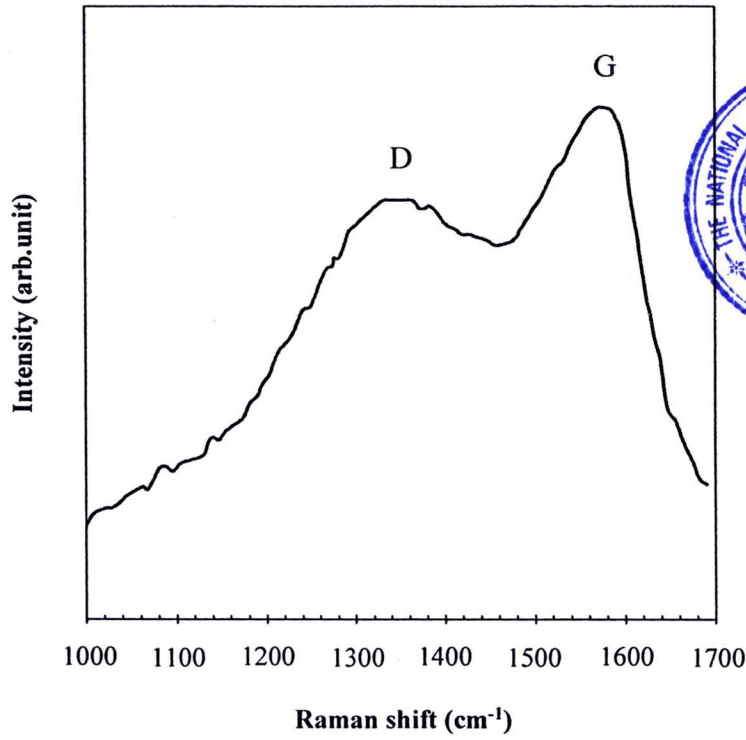

Figure 4.3 Raman spectrum of the agglomerated carbon nanoparticles synthesized at the laser intensity of 0.6 W.

These results could be ascribed that at a low temperature, vapor of the catalytic Ni and Co produced by the irradiation of the rod was condensed and then solidified rapidly because temperature difference between the furnace and laser irradiation was so high, leading to C atoms could diffuse and dissolve into the solidified catalytic nanoparticles difficultly (Yudasaka et al., 1999). Therefore, any fibrous could not be formed. However, the laser intensity effected on the number concentration of the synthesized carbon nanoparticles because C, Ni and Co vapor could be higher produced at increasing of laser intensity, leading to higher number concentration of the synthesized carbon nanoparticles.

4.1.2 Effect of temperature

In this part, the effect of the temperature in a range of 25, 200, 400, 600, 800, 1000 and 1080 °C on the morphology, size distribution and crystallinity of the synthesized SWCNTs was investigated under the condition of the laser intensity of 0.6 W, atmospheric pressure and nitrogen flow rate of 1.5 L/min.

The synthesized airborne carbon nanoparticles at different temperatures were collected on a membrane filter. The morphology of those carbon nanoparticles was observed using SEM as shown in Figure 4.4. At the temperature of 25, 600 and 800 °C, agglomerates of spherical nanoparticles were observed without any fibrous particles as shown in Figure 4.4(a), (b) and (c), respectively. While a higher concentration of fibrous and spherical products could be obtained at the temperature of 1000 and 1080 °C as shown in Figure 4.4(d) and (e), respectively. All fibrous particles have the average diameter less than 20 nm and length of longer than 500 nm while the spherical primary particles were in a size range of 10–20 nm, which were agglomerated each other. It is inferred that the fibrous products were CNTs and the spherical products were amorphous carbon or metallic nanoparticles.

These results would be ascribed to the fact that at a low temperature, carbon clusters and catalytic Ni and Co nanoparticles would undergo very slow diffusion process, leading to insufficient supply of carbon precursor (Yudasaka et al., 1999). Therefore, lower quantity of nanostructure products was synthesized.

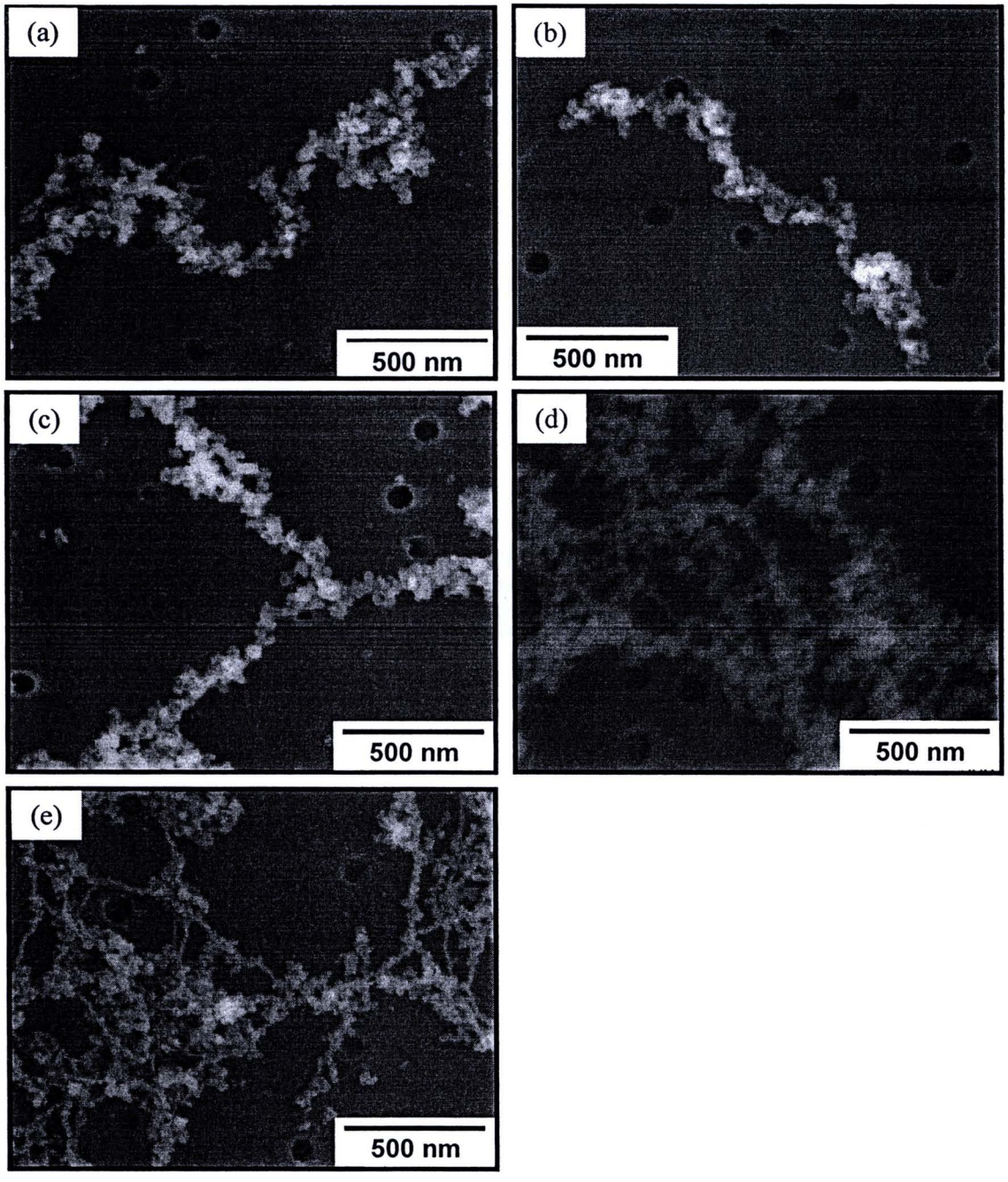

Figure 4.4 SEM images of the synthesized carbon nanoparticles at different temperatures on membrane filter: (a) 25 °C, (b) 600 °C, 800 °C, (d) 1000 °C and (e) 1080 °C.

Size distributions of the produced airborne carbon nanoparticles measured by SMPS system are shown in Figure 4.5. In the measurable size range (20–600 nm in mobility diameter), highly carbon nanoparticles were synthesized in aerosol form. At the temperature of 25 °C, relatively narrow size distribution with the peak diameter around 100–200 nm could be observed. Size distributions with the

same of the peak diameter become broader at higher temperatures (200, 400, 600 and 800 °C). It could be clearly observed that at higher temperature, their size distribution was much broader, especially at the temperature of 600 and 800 °C. While at the temperature of 1000 and 1080 °C, size distributions were as similar as those of the temperature of 600 and 800 °C. However, new peak around 20 nm was observed. The total number concentration of the synthesized CNTs could be synthesized by this system in the order of 10^6 particles/cc. It is corresponding to mass concentration in the order of ten mg/m^3 with an assumption of uniform density.

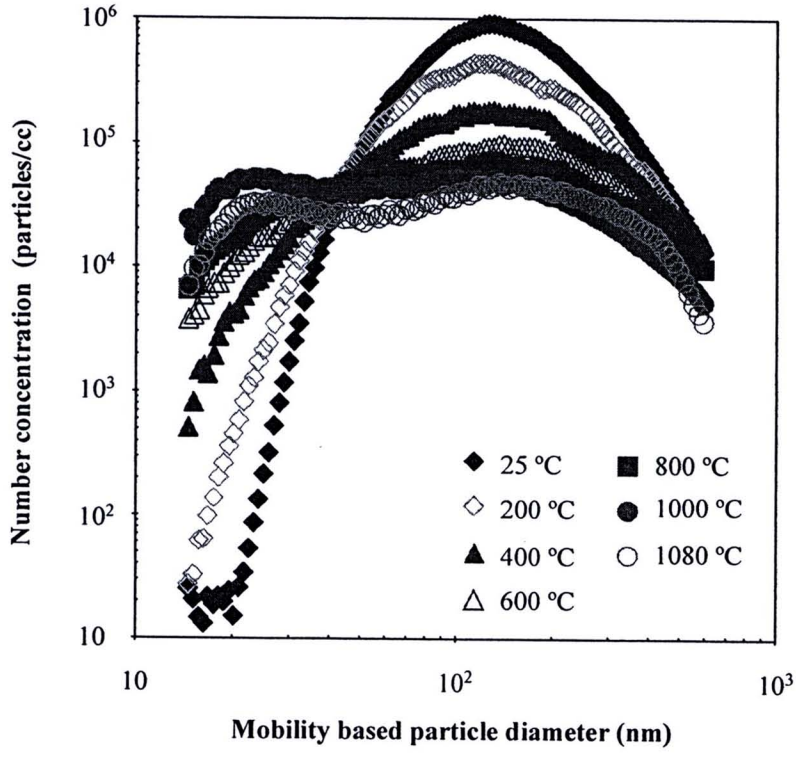

Figure 4.5 Mobility based size distribution of the synthesized carbon nanoparticles at different temperatures.

Changes in the mobility size distribution would be attributed to the generation of fibrous particles which could be observed in the typical SEM images. At the temperature of 25, 200, 400, 600 and 800 °C, any fibrous particles could be observed in the SEM image because the catalyst particles could not activate majority of carbon atoms to form CNTs (Kataura et al., 2000). Therefore, only spherical (primary) particles formed and then agglomerated while the particles suspended in gas. On the other hand, at the temperature of 1000 and 1080 °C, the temperatures were

high enough for stimulating the formation of the CNTs. Carbon atoms could be activated on the catalyst surface to grow CNTs. Furthermore, some agglomerated particles were simultaneously formed and adhered on the outer wall of the fibers in the gas phase.

In addition, the correlation between the geometric dimensions of CNT measured from SEM images (Figure 4.4) and mobility spectrum of those in the gas phase (Figure 4.5) was analyzed. The monodispersed aerosol of the synthesized SWCNTs at the temperature of 1080 °C was prepared by the size classification using DMA.

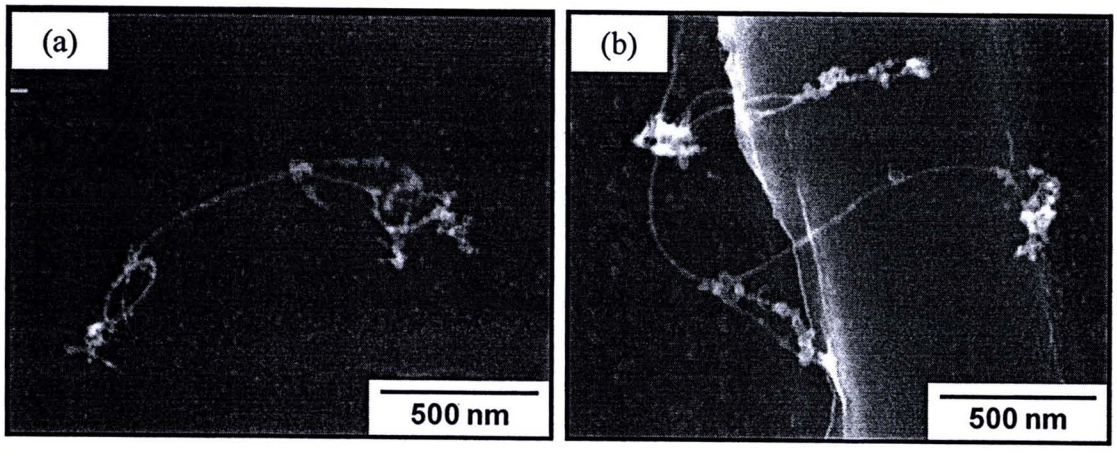

Figure 4.6 SEM images of the classified particles by DMA synthesized at the temperature of 1080 °C with different classified size: (a) 100 nm and (b) 200 nm.

Figure 4.6 shows typical SEM images of particles classified to be (a) 100 nm and (b) 200 nm in mobility-based diameter by DMA. Figure 6(a) exhibits fibrous structured particles with diameter less than 10 nm and length of more than 1 micrometer. Some spherical particles, which would potentially be amorphous carbon or catalytic particles, coagulate on to the surface of the fiber. The diameter of the fiber classified at 200 nm as shown in Figure 4.6(b) was similar to those of 100 nm. However, the length is much larger than the particle shown in Figure 4.6(a).

The mobility based particle diameter is known to be proportional to projected area equivalent diameter in the case of non-spherical particles (Kim, and Zachariah, 2006) as shown in equation 4.1

$$L_f D_f = \frac{\pi D_A^2}{4} \tag{4.1}$$

where L_f = The length of the CNT,

D_f = The diameter of the CNT

D_A = The projected area diameter of the CNT

Kim et al., 2006 reported that the mobility diameter (D_m) of CNTs was determined by linearly proportional to the projected area diameter (D_A), which was obtained from the combination of TEM images and digital image software analysis. Therefore, it is acceptable that the projected area diameter (D_A) of carbon nanoparticles could be estimated from the mobility diameter (D_m) as shown in 4.2. Constants were obtained in a prior study where mobility classified fibers were deposited on TEM grids and digitized to obtain the projected area diameter.

$$D_A = 1.1621 D_m - 8.9131 \tag{4.2}$$

Therefore, the similar size distributions of the synthesized SWCNTs at 1000 and 1080 °C could imply the similar projected area equivalent diameter of them which corresponded to the similar morphology of them as shown in Figure 4.4(b) and (c), respectively.

The similarity of the fiber diameter classified at 100 and 200 nm seems to be affected by the formation of uniform catalysts. After the ablation of the target, catalyst nanoparticles were generated by the vapor phase condensation. Then, carbon atoms diffused into the catalysts to form the tubes and became fibers. In other words, the numbers of the SWCNTs in each classified fiber diameter were close each other because the fibers originated from that of isolated tubes became lower energy after a certain fiber diameter was reached. Then, the addition of further isolated tubes might not been energetically favorable (Wang et al., 2006), leading to the nearly same numbers of the tubes in each fiber.

In order to characterize crystallinity of the synthesized carbon nanoparticles, Raman spectroscope was employed. Raman spectra of the airborne carbon nanoparticles synthesized at the different temperatures were shown in Figure 4.7. It is well recognized that the Raman shift band in the range of 100–300 cm^{-1},

which is known as the radial breathing mode (RBM), is a signature of SWCNTs (Saito, Dresselhaus, and Dresselhaus, 1998). Those RBM frequency ω_{RBM} (cm^{-1}) depends strongly on the SWCNT diameter (d_t), as could be described by equation 4.3.

$$\omega_{RBM} = \frac{A}{d_t} + B \tag{4.3}$$

where A (in nm cm^{-1}) and B (in cm^{-1}) are constants and vary between isolate tube and bundle tubes.

Regarding to the low Raman shift range, broad spectrum in Figure 4.7(a) reveals that negligible amount of SWCNTs were synthesized at the temperature of 25 °C, while the distinctive RBM signal at 220–240 cm^{-1} could assure the presence of SWCNTs within the airborne carbon nanoparticles synthesized at higher temperatures of 1000 and 1080 °C, respectively. Regardless the effect of single tube–tube interaction within tube bundle, the respective values of parameter A and B equal to 248 nm cm^{-1} and 0 cm^{-1} (Jorio et al., 2001). As a result, the calculated diameter of the SWCNTs synthesized at 1000 and 1080 °C were equivalent to 1.1 and 1.2 nm, respectively.

In the high Raman shift region (1,300–1,600 cm^{-1}) which is associated with the tangential C–C stretching mode of their radiated carbon nanoparticles, a stronger band at 1,590 cm^{-1} known as the G band, and another band at 1,350 cm^{-1} known as the D band are distinctively observed. The presence of graphitic bonding due to the periodic sp^2 valance in crystalline carbonaceous material would strengthen the intensity of the G band scattering (Ganter et al., 2009). This band shows two different components, the lower frequency component (G^-) and higher frequency component (G^+) which associated with vibration along the circumferential direction and direction of the CNT axis, respectively (Liu et al., 2009). Meanwhile, the D band would reflect the present of disorder and defective carbonaceous constituents. Therefore, the intensity of D to G band (I_D/I_G ratio) could represent the relative existence of amorphous carbon to crystalline components within the irradiated sample.

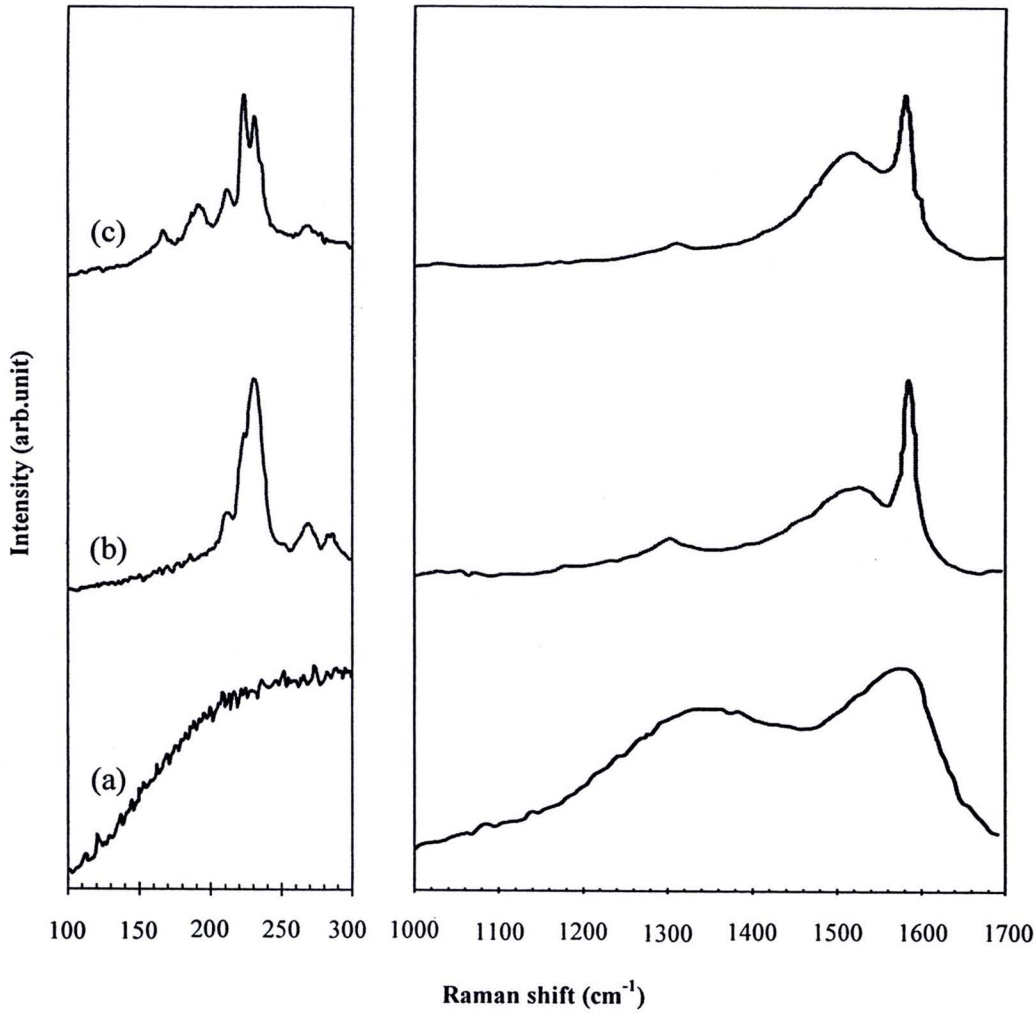

Figure 4.7 Raman spectra of the airborne SWCNTs synthesized at different temperatures: (a) 25 °C, (b) 1000 °C and (c) 1080 °C.

As could be observed in Figure 4.8, the I_D/I_G ratios of the synthesized carbon nanoparticles were 0.81, 0.20 and 0.15 at the temperature of 25, 1000 to 1080 °C, respectively. In consistent with previous works (Kokai et al., 1999), these lower I_D/I_G ratios reveal the higher graphitic crystallinity of the airborne SWCNTs synthesized at the elevated temperature. Based on both lower and higher Raman shift signals, it could be anticipated that the airborne carbon nanoparticles synthesized at 1080 °C would contain the highest content of SWCNTs.

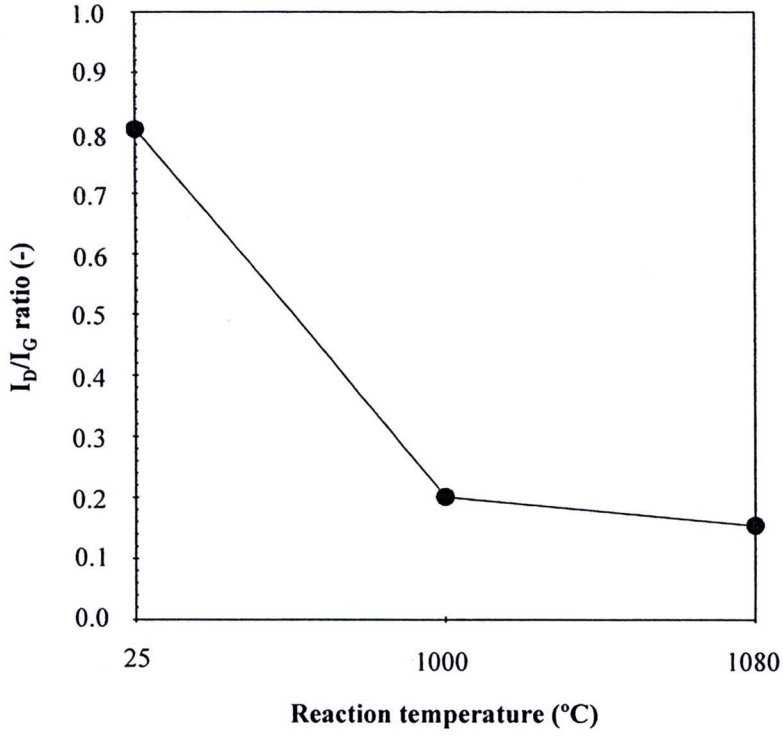

Figure 4.8 The I_D/I_G ratios of the synthesized carbon nanoparticles at different temperature.

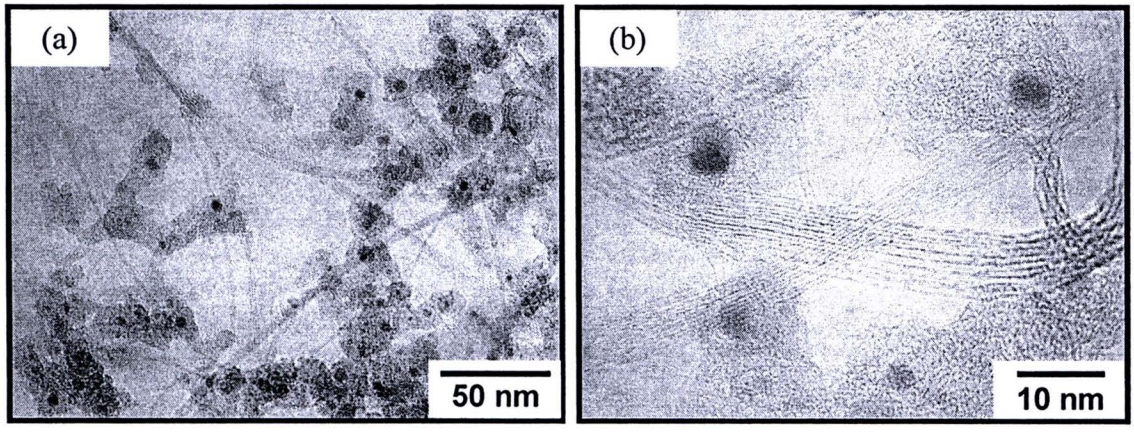

Figure 4.9 TEM images with different magnifications of the airborne SWCNTs synthesized at temperature of 1080 °C.

In order to finding the existence of SWCNTs within the airborne carbon nanoparticles, TEM analysis of as-prepared products was performed. HRTEM micrographs of the airborne product synthesized at 1080 °C were shown in Figure 4.9. It could be clearly seen the presence of isolated and bundling SWCNTs coexisting with amorphous carbon and catalyst nanoparticles.

Based on the TEM images, the diameter distribution of the isolated SWCNT is in a narrow range of 1.0–1.7 nm, which is in acceptable agreement with the calculated results using equation 4.3. Further quantitative analysis of SWCNT diameter was also conducted and plotted in Figure 4.10. It could be clearly observed that the modal diameter of the SWCNTs was about 1.2 nm.

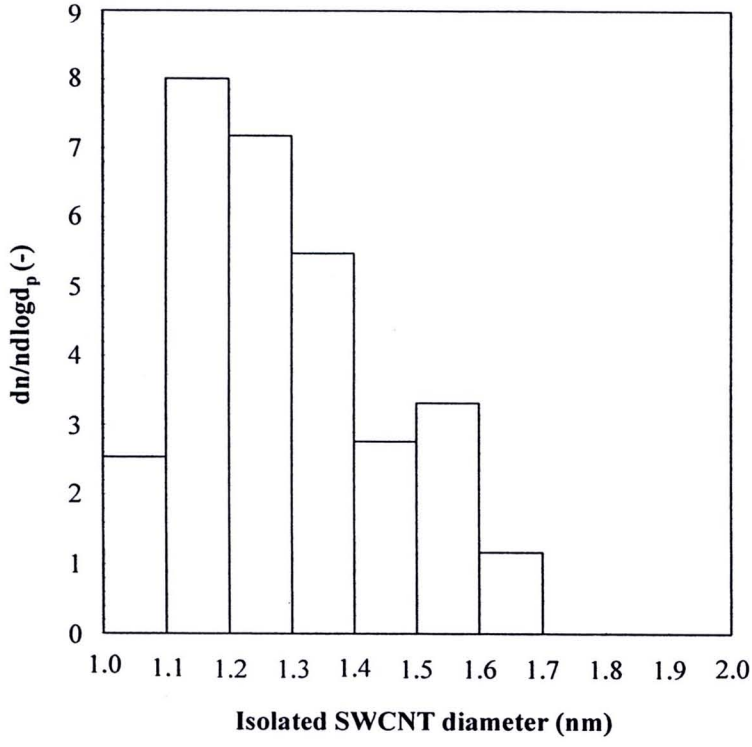

Figure 4.10 Size distribution of the isolated SWCNTs at the temperature of 1080 °C measured by TEM image processing.

4.1.3 Possible mechanisms

SWCNT formation mechanism, proposed here, is believed that vapor-liquid-solid (VLS) mechanism of carbon catalyzed by molten metal nanoparticles (Gorbunov et al., 2002). At first, carbon, nickel and cobalt vapors are produced from laser irradiation on the C/Ni/Co target rod. The metal catalyst particles act as nuclei for the growth of the tubes in the gas phase (Nyamori, Mhlanga, and Coville, 2008) are formed which shown in Figure 11. The Ni/Co catalyst vapors initially form nuclei in nucleation process, after that the nuclei condense and coagulate in condensation and particle coagulation, respectively. C vapors around the catalyst particles diffuse

on catalyst surface and dissolute until saturate inside the catalyst particles in carbon diffusion, dissolution and saturation of carbon process, respectively. Because of carbon saturation inside the catalysts, carbon atoms segregate from the catalyst particles and then form into SWCNTs.

This proposed mechanism also explains how the SWCNTs growth is influenced by the temperature. At the temperature of 1080 °C, the initial Ni/Co catalyst vapors gradually form into the molten catalytic particles because of gradual decreasing of temperature from laser source to temperature. The Ni/Co catalyst vapors can be transformed their phase into liquid droplets. Therefore, carbon vapors from laser vaporized C/Ni/Co target rod can highly diffuse into the molten catalytic particles. While the temperature of 1000 °C, amount of the molten catalytic particles are decreased gradually leading to lower dissolution of the carbon vapors. Therefore, the SWCNTs synthesized at the temperature of 1000 °C have lower purity than those of 1080 °C as shown in Figure 5. However, at the temperature of 25 °C, the catalytic particles are no longer molten in form of the liquid droplets but in solid particles because of rapid decreasing of the temperature from the laser source to the temperature. None of carbon vapors can dissolve into the catalytic particles at all, leading to none of the formation of the SWCNTs (Yudasaka et al. (1999)). This is reason of the SWCNTs at the higher temperature more clearly seen in Figure 4 which is good agreement with the formation behavior of the SWCNTs from size classification by DMA.

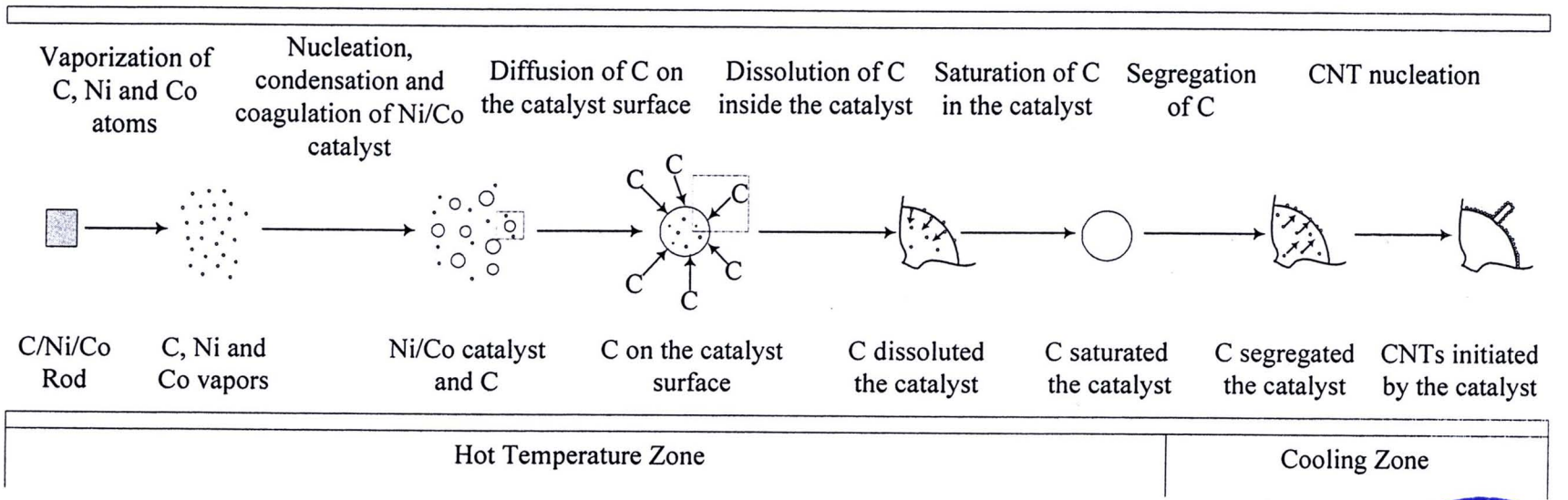

Figure 4.11 Vapor-liquid-solid Mechanisms of the SWCNTs synthesized by laser ablation

4.2 Synthesis of the carbon nanoparticles by CVD of glycerol and ferrocene

From many experimental results reported in other previous works, this part has set its aim to study effect of synthetic parameters on the morphology, size, crystallinity and purity, and yield of the carbon nanoparticles synthesized by CVD of the mixture of glycerol and ferrocene. Effect of synthesizing temperature, nitrogen flow rate and glycerol to ferrocene molar ratio on the morphology, size, crystallinity and purity, and yield of the synthesized carbon nanoparticles were thoroughly investigated and then reported and discussed in this part.

Referring to temperature profiles as shown in Appendix A, it could be clearly seen each profile consisted of 3 temperature gradients along flow direction including zone 1 (0-15 cm from inlet) where the temperature increased from the lowest to the highest, zone 2 (15-45 cm from inlet) where the temperature was the highest and zone 3 (45-60 cm from inlet) where the temperature decreased from the highest to the lowest. It is well known that the temperature gradients and velocities gradients took place throughout the quartz tube reactor and could affect on the morphology, size, crystallinity and purity, and yield of the synthesized carbon nanoparticles. Therefore, the synthesized carbon nanoparticles were distinguish studied into 3 different zones as presented above.

4.2.1 Effect of nitrogen flow rate

In this part, the effect of nitrogen flow rate on the morphology, size, crystallinity and purity, and yield of the synthesized carbon nanoparticles was studied under the same condition of synthesizing temperature of 800 °C and glycerol to ferrocene molar ratio of 5 to 1.

Zone 1

SEM images as shown in Figure 4.12 revealed the carbon nanoparticles deposited at zone 1 within the quartz tube reactor with different nitrogen flow rates. At nitrogen flow rate of 50 mL/min, the morphology of the synthesized carbon nanoparticles shown in Figure 4.12(a) was warm-like MWCNTs with outer diameter and length of the tubes in range of 175-200 nm and 600-750 nm,

respectively. While the longer MWCNTs were clearly seen at higher nitrogen flow rate. At nitrogen flow rate of 200 mL/min, the MWCNTs with outer diameter of about 180 nm and length of about 10 μm, respectively were synthesized as shown in Figure 4.12(b). At nitrogen flow rate of 350 and 500 mL/min, the synthesized carbon nanoparticles were carpet-like MWCNT structure as shown in Figure 4.12(c) and (d), respectively. The diameters of the tubes at nitrogen flow rate of 350 mL/min were in range of 30-80 nm. While the diameters of the tubes at nitrogen flow rate of 500 mL/min were in range of 30-60 nm. Furthermore, it could be clearly seen some amorphous carbons deposited on the outer wall of the synthesized MWCNTs.

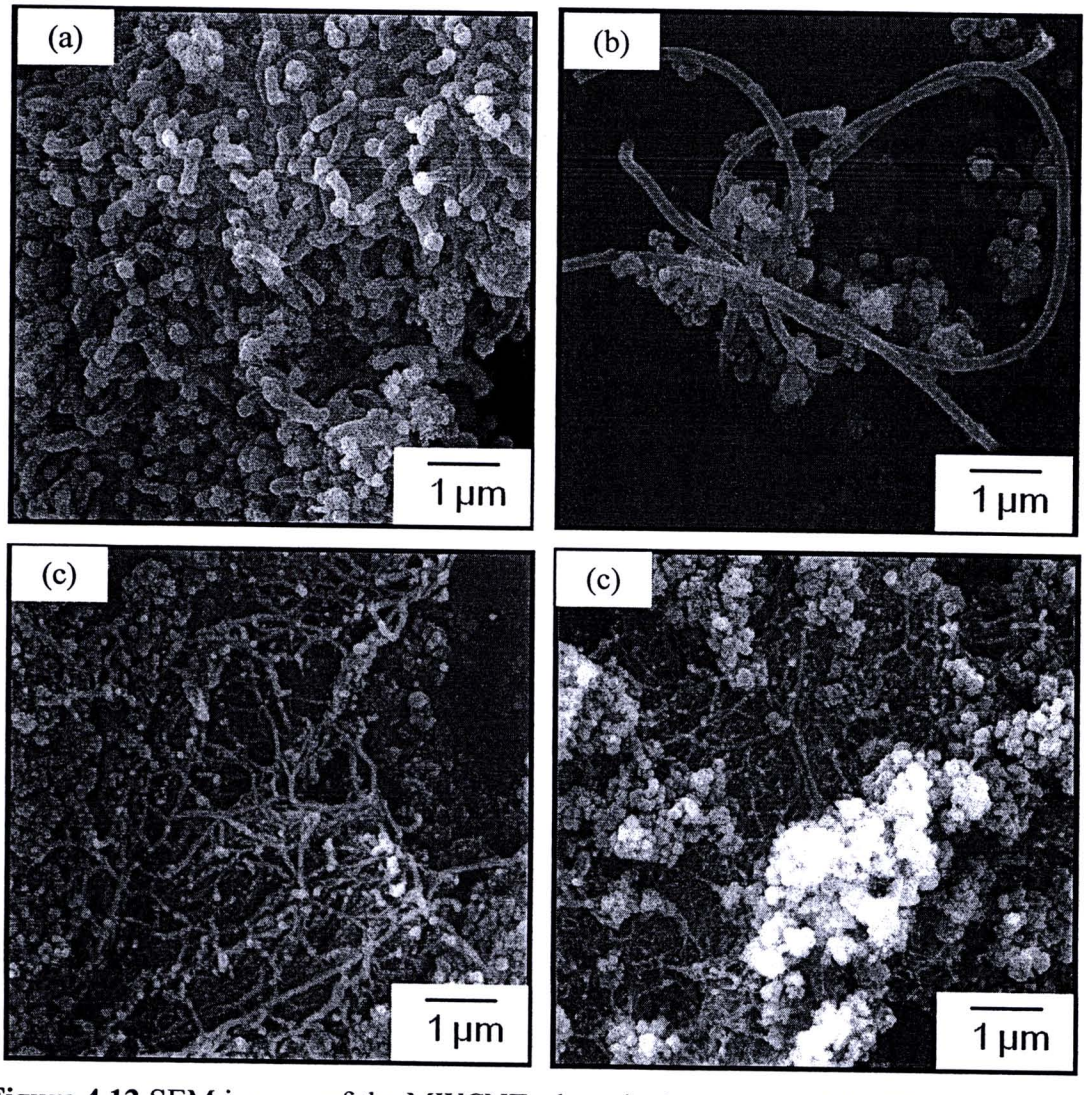

Figure 4.12 SEM images of the MWCNTs deposited at zone 1 with different nitrogen flow rates: (a) 50 mL/min, (b) 200 mL/min, (c) 350 mL/min and (d) 500 mL/min.

Raman spectra of the MWCNTs deposited at zone 1 with different nitrogen flow rates as shown Figure 4.13 exhibited their strong response at about 1,590 cm^{-1} from graphitic bonding in crystalline carbon which known as G peak, and another peak at about 1,350 cm^{-1} from disorder and defective carbon which known as D peak. The I_D to I_G ratios of the MWCNTs deposited at zone 1 with the nitrogen flow rate of 50, 200, 350 and 500 mL/min were 0.66, 0.33, 0.24 and 0.28, respectively.

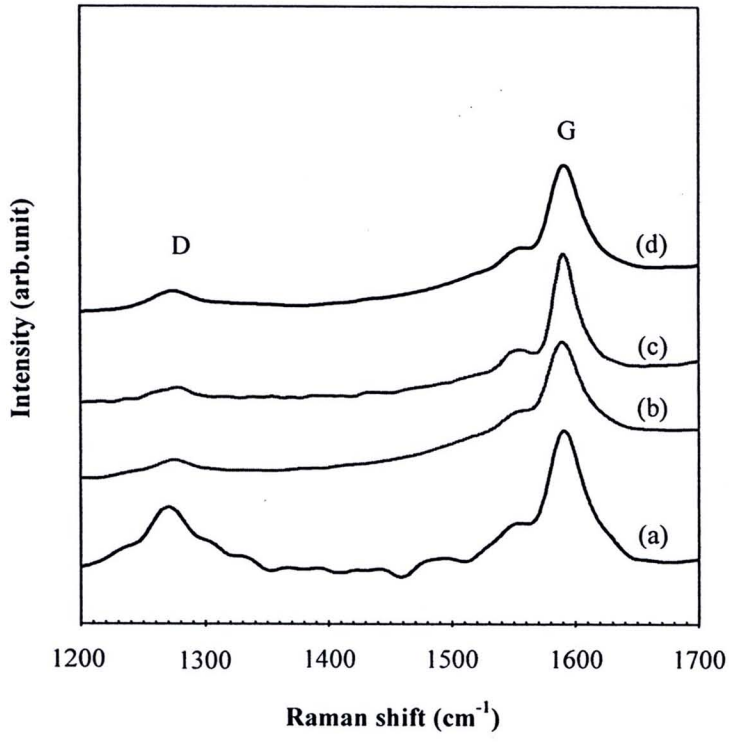

Figure 4.13 Raman spectra of the MWCNTs deposited at zone 1 with different nitrogen flow rates: (a) 50 mL/min, (b) 200 mL/min, (c) 350 mL/min and (d) 500 mL/min.

Zone 2

SEM images of the carbon nanoparticles deposited at zone 2 with different nitrogen flow rates were shown in Figure 4.14. At nitrogen flow rate of 50 mL/min, the synthesized carbon nanoparticles shown in Figure 4.14(a) was warm-like MWCNTs with outer diameter and length of the tubes in range of 125-200 nm and about 1 μm, respectively. While the longer MWCNTs were clearly seen at higher

nitrogen flow rate. At nitrogen flow rate of 200 mL/min, the curvature of MWCNTs with outer diameters in range of 40-150 nm were synthesized as shown in Figure 4.14(b). At nitrogen flow rate of 350 mL/min, the synthesized carbon nanoparticles were straight MWCNTs with the outer diameters in range of 40-80 nm as shown in Figure 4.14(c). While the morphology of synthesized carbon nanoparticles at the nitrogen flow rate of 500 mL/min was urchin-like MWCNT structure which the tubes with the outer diameter and length of their tubes in range of 30-60 nm and about 1 μm, respectively were grown from agglomerated catalytic particles as shown in Figure 4.14(d).

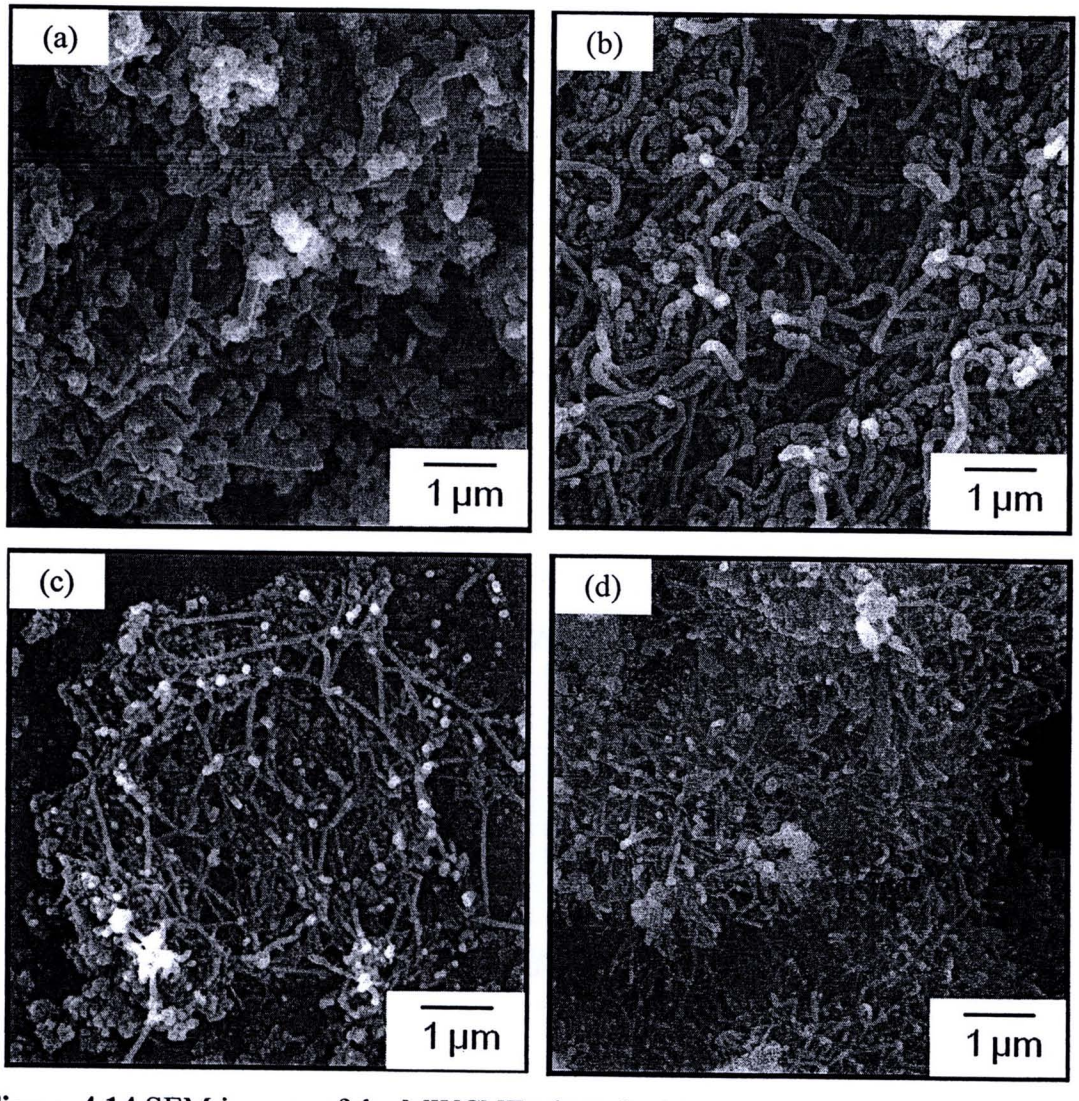

Figure 4.14 SEM images of the MWCNTs deposited at zone 2 with different nitrogen flow rates: (a) 50 mL/min, (b) 200 mL/min, (c) 350 mL/min and (d) 500 mL/min.

Raman spectra of the MWCNTs deposited at zone 2 with different nitrogen flow rates in Figure 4.15 exhibited the same of 2 responses at G peak and D peak which the I_D to I_G ratios of the MWCNTs deposited at zone 2 with the nitrogen flow rate of 50, 200, 350 and 500 mL/min were 0.88, 0.43, 0.21 and 0.31, respectively.

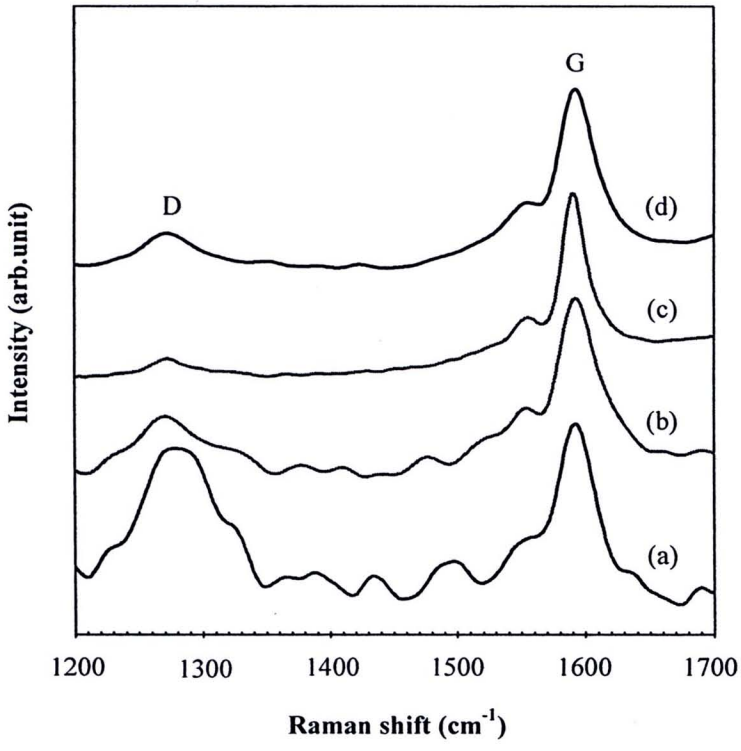

Figure 4.15 Raman spectra of the MWCNTs deposited at zone 2 with different nitrogen flow rates: (a) 50 mL/min, (b) 200 mL/min, (c) 350 mL/min and (d) 500 mL/min.

Zone 3

SEM images as shown in Figure 4.16 revealed the carbon nanoparticles deposited at zone 3 with different nitrogen flow rates. At nitrogen flow rate of 50 mL/min, the synthesized carbon nanoparticles shown in Figure 4.16(a) was MWCNTs with outer diameter and length of the tubes about 170 nm and 1-3 μm, respectively. While the longer MWCNTs were clearly observed at higher nitrogen flow rate. At nitrogen flow rate of 200 mL/min, the MWCNTs with outer diameters and length of the tubes in range of 80-170 nm and more than 3 μm, respectively were

synthesized as shown in Figure 4.16(b). While the morphology of synthesized carbon nanoparticles at the nitrogen flow rate of 350 mL/min was carpet-like MWCNT structure which the tubes with the outer diameters in range of 40-80 nm as shown in Figure 4.16(c). At nitrogen flow rate of 500 mL/min, the synthesized carbon nanoparticles were the combination of the straight MWCNTs with the outer diameters about 50 nm and agglomerated particles as shown in Figure 4.16(d).

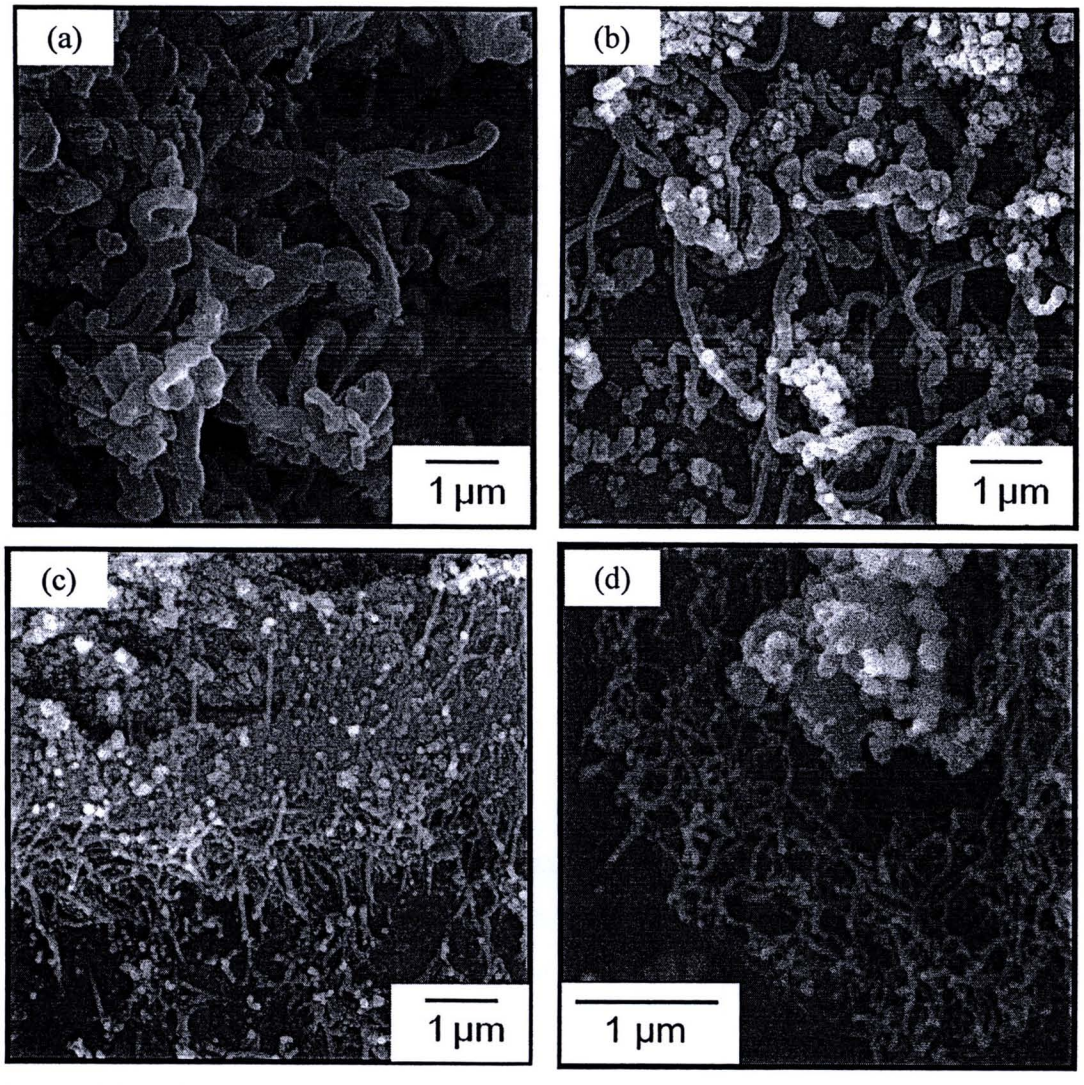

Figure 4.16 SEM images of the MWCNTs deposited at zone 3 with different nitrogen flow rates: (a) 50 mL/min, (b) 200 mL/min, (c) 350 mL/min and (d) 500 mL/min.

Raman spectra of the MWCNTs deposited at zone 3 synthesized with different nitrogen flow rates were shown in Figure 4.17. Their responses were at G peak and D peaks. The I_D/ I_G ratios of the MWCNTs deposited at zone 3 with the

nitrogen flow rate of 50, 200, 350 and 500 mL/min were 0.59, 0.43, 0.22 and 0.31, respectively.

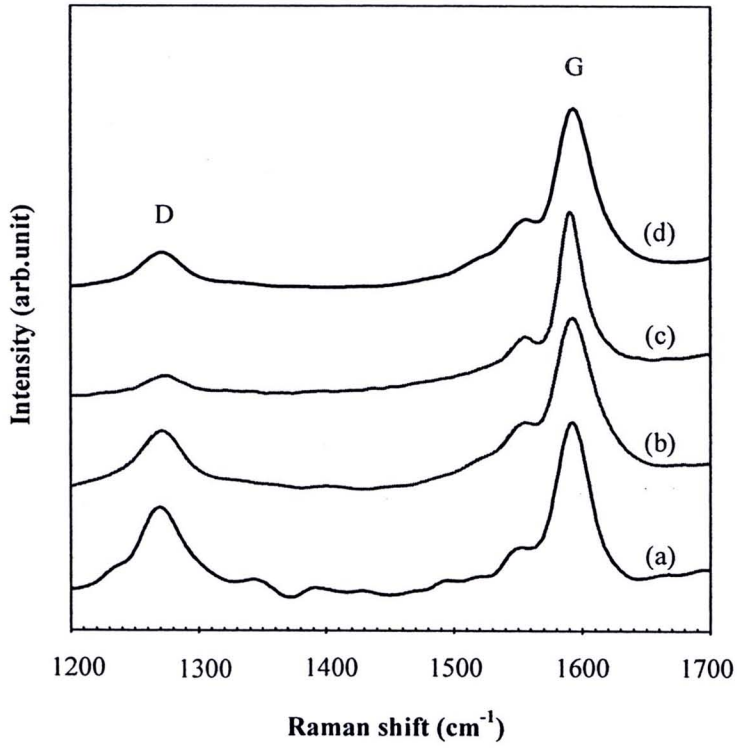

Figure 4.17 Raman spectra of the MWCNTs deposited at zone 3 with different nitrogen flow rates: (a) 50 mL/min, (b) 200 mL/min, (c) 350 mL/min and (d) 500 mL/min.

The I_D/I_G ratios in Figure 4.18 revealed that the nitrogen flow rate strongly affected on crystallinity and purity of the synthesized carbon nanoparticles. At nitrogen flow rate of 50 mL/min, the carbon nanoparticles deposited at begin, middle and zone 3 had the lowest crystallinity and purity compared to the carbon nanoparticles synthesized at higher flow rate deposited at the same positions. While the carbon nanoparticles synthesized at nitrogen flow rate of 350 mL/min had the highest crystallinity and purity. Therefore, in this work, the nitrogen flow rate of 350 mL/min was optimal flow rate for the synthesis of the CNTs.

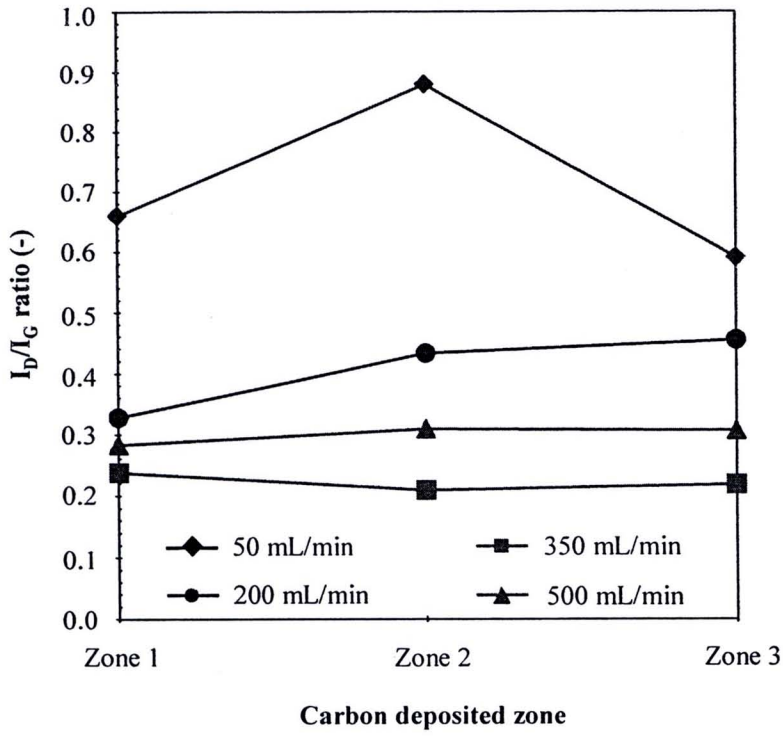

Figure 4.18 I_D/I_G ratios of the synthesized MWCNTs at different nitrogen flow rates.

Carbon yields of the synthesized carbon products can be defined in equation 4.4.

$$\text{Carbon yield}\,(\%) = \frac{W_{C,1} + W_{C,2} + W_{C,3}}{W_{\text{glycerol}} + W_{\text{ferrocene}}} \times 100 \qquad (4.4)$$

where $W_{C,1}$ = Weight of synthesized carbon at zone 1

$W_{C,2}$ = Weight of synthesized carbon at zone 2

$W_{C,3}$ = Weight of synthesized carbon at zone 3

W_{glycerol} = Weight of used glycerol

$W_{\text{ferrocene}}$ = Weight of used ferrocene

Figure 4.19 shows the carbon yields of the synthesized carbon nanoparticles with different nitrogen flow rates. At the nitrogen flow rate of 50 mL/min, the carbon yield was 6.1 %. While the yield gradually decreased as 4.2, 2.1 and 1.7 % at the nitrogen flow rate of 200, 350 and 500 mL/min, respectively.

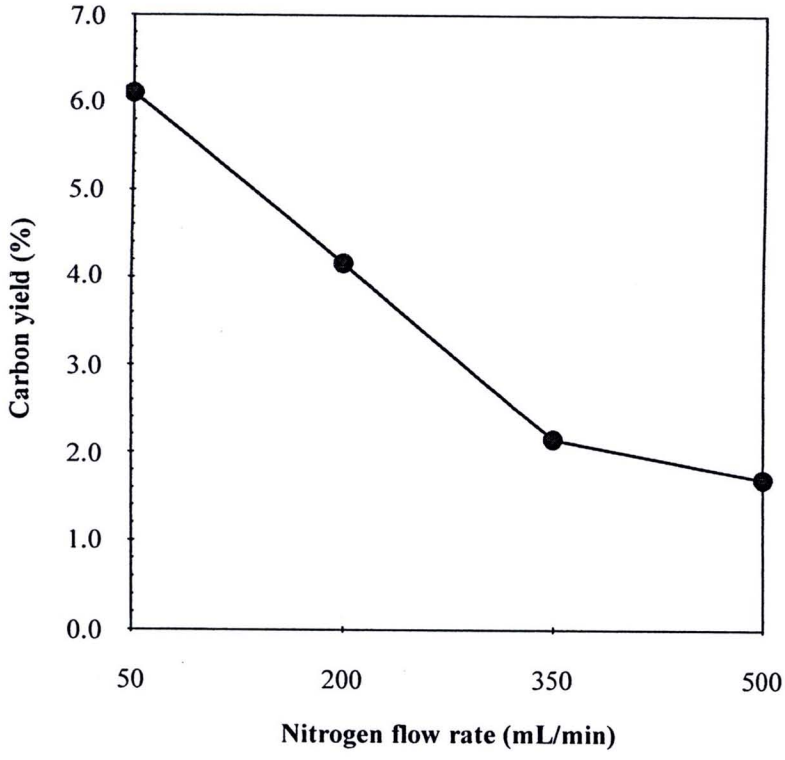

Figure 4.19 Yields of the synthesized carbon nanoparticles at different nitrogen flow rates.

It is well known that residence time is the time that a particle spends in a particular system which is the inversely proportional function of a flow rate. From Figure 4.20, it could be clearly observed that residence time was significantly decreased from 11.5 to 2.9, 1.6 and 1.2 when the nitrogen flow rate was increased from 50 to 200, 350 and 500 mL/min.

From the experimental results, the increase in the nitrogen flow rate resulted in significant decrease in the tube diameters which could be explained by residence time. From previous work (Kobayashi et al., 2004), it should be noted that the diameters of the synthesized CNTs were closely correlated with those of the catalytic nanoparticles and tended to be slightly smaller than the particle size. It means that decrease in the Fe size resulted in decrease in diameters of the tubes. The decrease in the Fe size could be occurred when aggregation of the Fe nanoparticles was decreased. Endo et al., 2001 reported that the aggregation of the Fe nanoparticles was decreased when the nitrogen flow rate was increased because of decrease in residence time. Therefore, in this part, the synthesized MWCNTs at the nitrogen flow rate of 50 mL/min with large tube diameters were found. While, at higher nitrogen

flow rate, the tube diameters of the synthesized MWCNTs significantly decreased because at higher nitrogen flow rate, the residence time was shorter, leading smaller size of the Fe nanoparticles as discussed above.

Increase in the nitrogen flow rate also resulted in significant decrease in the carbon yield. At the nitrogen flow rate of 50 mL/min, the residence time for contacting of the catalytic nanoparticles in liquid phase and carbon atoms was the maximum, leading to the highest yield of the carbon products. However, the maximum residence time for the contacting of the molten catalytic nanoparticles and the carbon atoms was too much, leading to excess carbon atoms could diffuse into the catalytic nanoparticles and then the catalytic nanoparticles were no longer activate the carbon atoms to form the CNTs. It is a reasonable that why the morphologies of the carbon nanoparticles synthesized at the lowest nitrogen flow rate were warm-like MWCNTs with the lowest purity and crystallinity compared to those at higher nitrogen flow rate. While decreasing of the carbon yield was taken place by decreasing of the residence time when the nitrogen flow rate was increased, leading to lower contacting of the catalytic nanoparticles and carbon atoms (Chaisitsak, Nukeaw and Tuantranont, 2007).

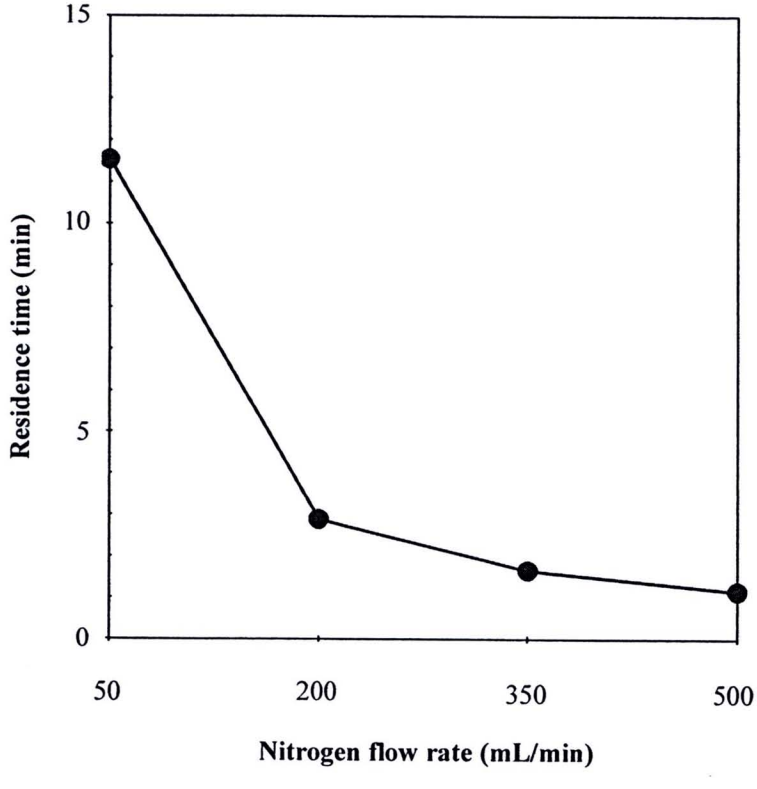

Figure 4.20 Residence time by varying nitrogen flow rate.

4.2.2 Effect of synthesizing temperature

In this part, the effect of the synthesizing temperature on the quality and quantity of the synthesized carbon nanoparticles was studied at condition of nitrogen flow rate of 350 mL/min and glycerol to ferrocene molar ratio at 5 to 1.

Zone 1

SEM images as shown in Figure 4.21 revealed the carbon nanoparticles deposited at zone 1 with different synthesizing temperatures. At the synthesizing temperature of 800 °C, the morphology of the synthesized carbon nanoparticles shown in Figure 4.21(a) was combination of the MWCNTs with outer diameters of the tubes in range of 30-80 nm and some of amorphous carbon. The MWCNTs with bigger outer diameter were clearly found at higher synthesizing temperature. At the synthesizing temperature of 850 °C, the uniform MWCNTs with outer diameter and length of the tubes in range of 50-125 nm and more than 10 nm, respectively were synthesized shown in Figure 4.21(b). While the synthesized carbon nanoparticles at the synthesizing temperature of 900 °C were combination of the MWCNTs with the diameters and length of the tubes in range of 90-190 nm and more than 10 nm, respectively and deposited amorphous carbon on the outer wall of the synthesized MWCNTs as shown in Figure 4.21(c).

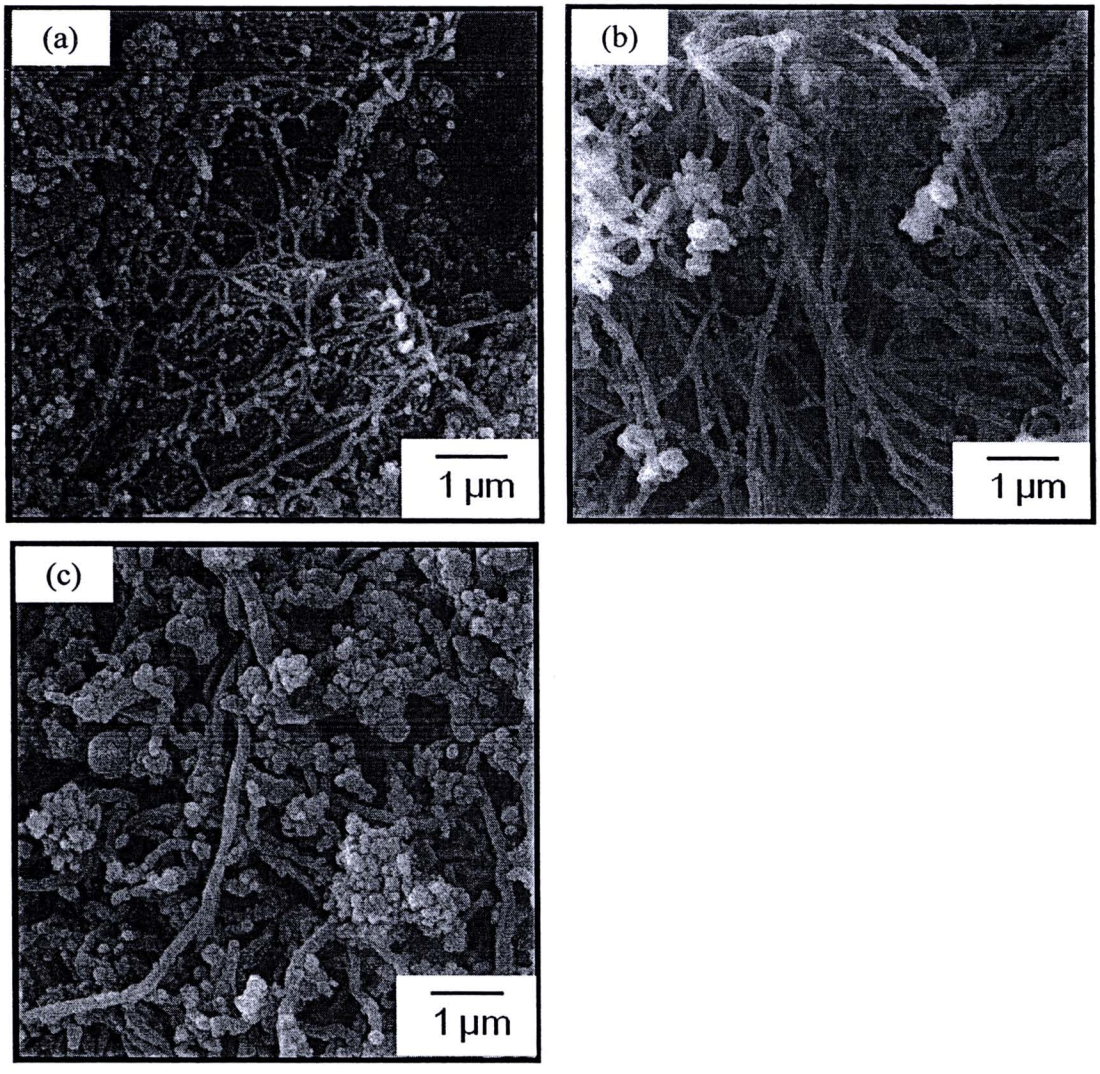

Figure 4.21 SEM images of the MWCNTs deposited at zone 1 with different synthesizing temperatures: (a) 800 °C, (b) 850 °C and (c) 900 °C

Zone 2

SEM images as shown in Figure 4.22 revealed the carbon nanoparticles deposited at zone 2 with different synthesizing temperatures. At the synthesizing temperature of 800 °C, the synthesized carbon nanoparticles shown in Figure 4.22(a) were straight MWCNTs with outer diameters of the tubes in range of 40-80 nm. While larger outer diameters of the MWCNTs were found at higher the synthesizing temperatures. At the synthesizing temperature of 850 °C, the MWCNTs with outer diameters in range of 60-190 nm, respectively were synthesized as shown in Figure 4.22(b). At the synthesizing temperature of 900 °C, the MWCNTs with outer diameters in range of 180-320 nm were synthesized as shown in Figure 4.22(c).

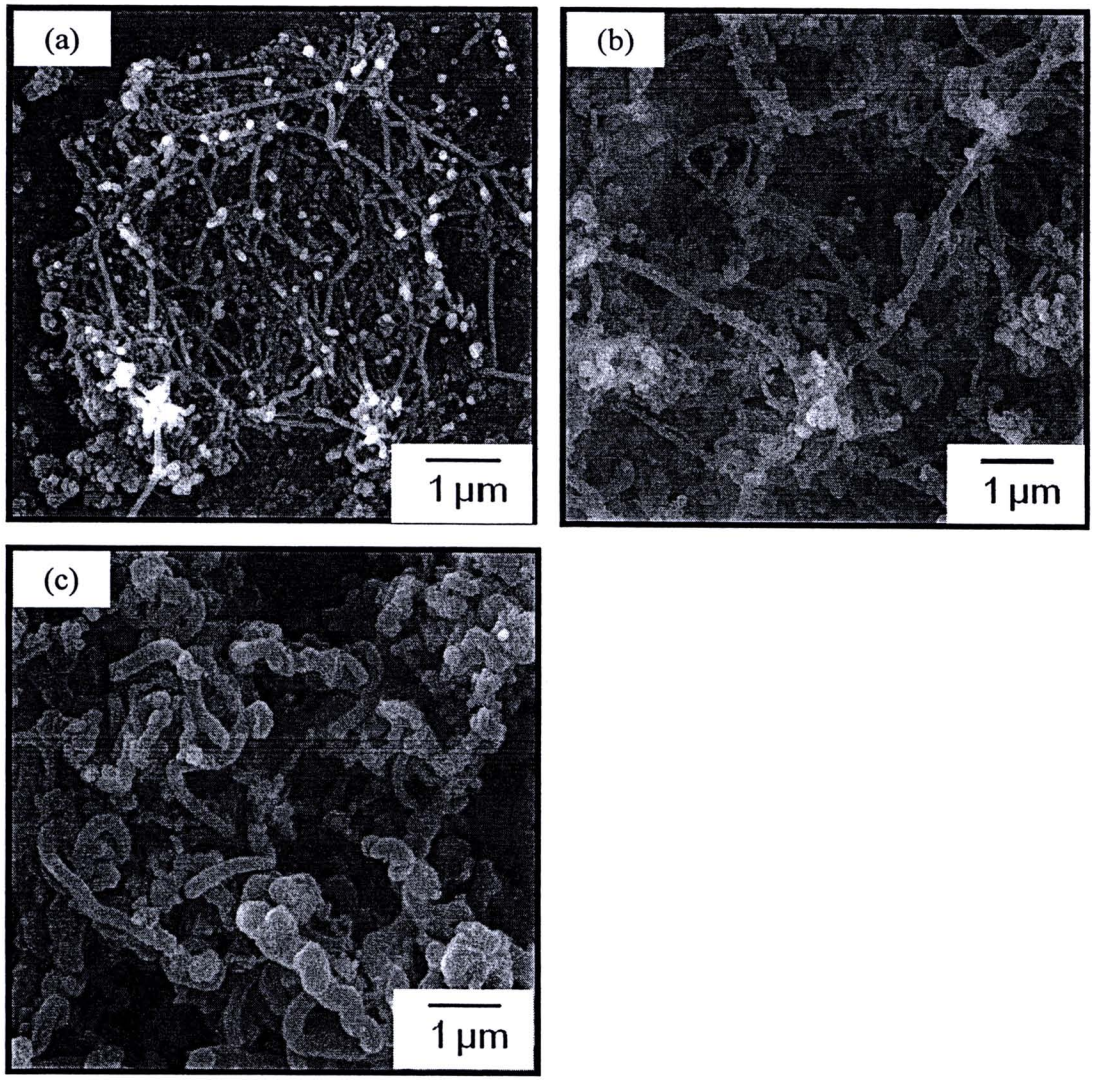

Figure 4.22 SEM images of the MWCNTs deposited at zone 2 with different synthesizing temperatures: (a) 800 °C, (b) 850 °C and (c) 900 °C.

Zone 3

SEM images the carbon nanoparticles deposited at zone 3 with different synthesizing temperatures were shown in Figure 4.23. At the synthesizing temperature of 800 °C, the morphology of the synthesized carbon nanoparticles shown in Figure 4.23(a) was the carpet-like MWCNTs with outer diameters of the tubes in range of 40-80 nm. The bigger diameters of the MWCNTs were clearly seen at higher synthesizing temperatures. At the synthesizing temperature of 850 °C, the straight MWCNTs with outer diameters and length of the tubes in range of 80-90 nm and more than 15 μm, respectively were synthesized as shown in Figure 4.23(b). At the synthesizing temperature of 900 °C, the synthesized carbon nanoparticles were

combination of the straight MWCNTs with the outer diameters of the tubes in range of 250-340 nm and helical MWCNTs as shown in Figure 4.23(c).

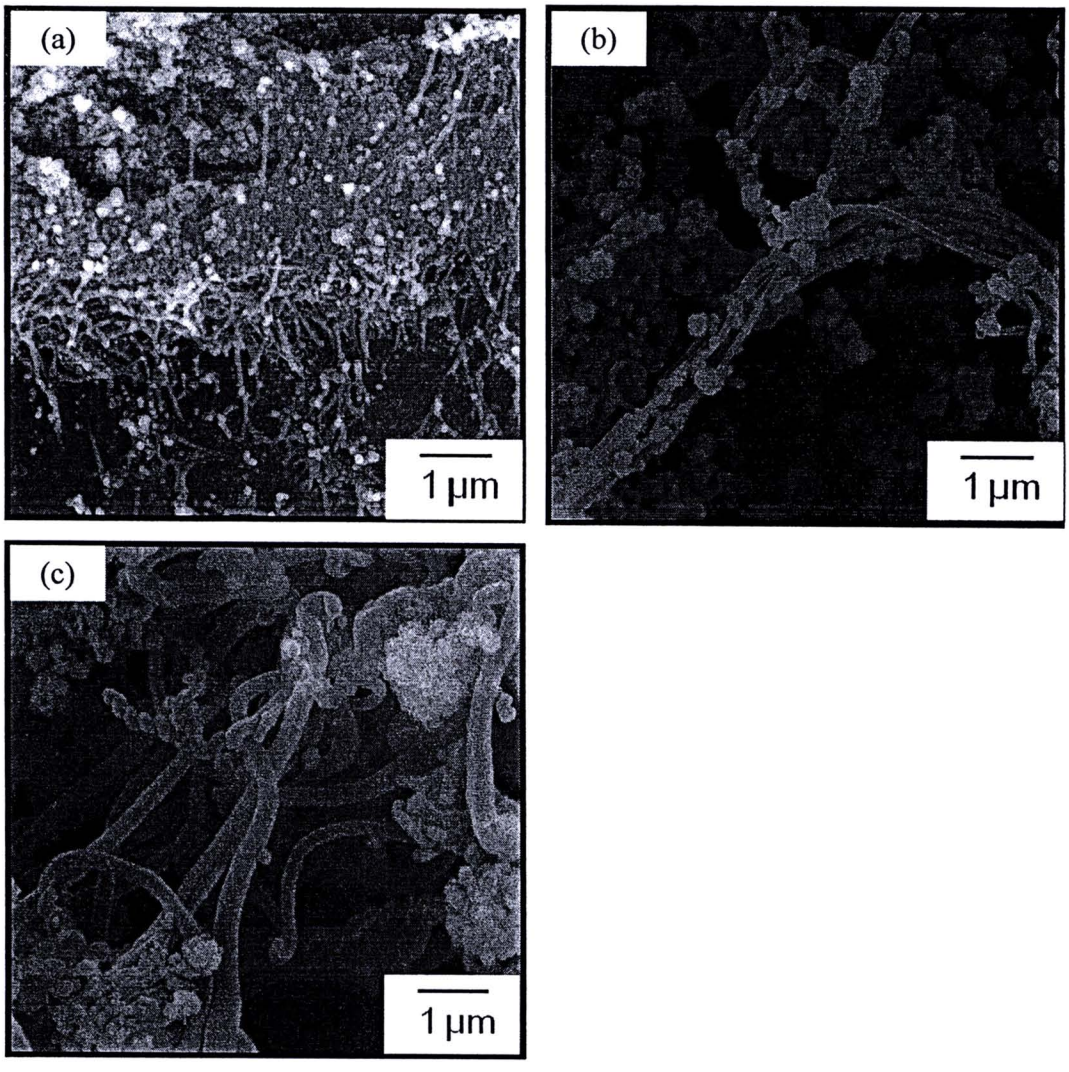

Figure 4.23 SEM images of the MWCNTs deposited at zone 3 with different synthesizing temperatures: (a) 800 °C, (b) 850 °C and (c) 900 °C.

The experimental results revealed that the tube diameters were increased when the synthesizing temperature was increased. The increase in the synthesizing temperature resulted in higher aggregation of the Fe nanoparticles (Stanek et al., 1995), leading to larger sizes of the Fe nanoparticles. Referring to above discussion, the tube diameters were controlled by the sizes of the Fe nanoparticles. Therefore, in this part, the larger sizes of the Fe nanoparticles at higher synthesizing temperature resulted in the larger tube diameters.

Raman spectra of the MWCNTs deposited at zone 1, zone 2 and zone 3 with different synthesizing temperatures exhibited their strong responses including D peak and G peak as same as the MWCNTs synthesized at different nitrogen flow rates. The I_D/I_G ratios of the synthesized MWCNTs with different synthesizing temperatures were shown in Figure 4.24.

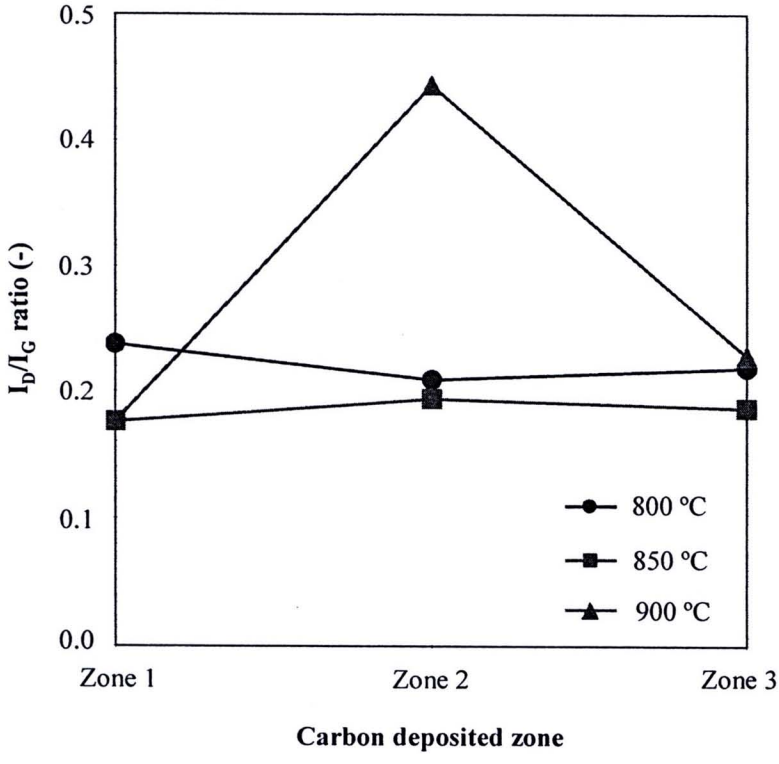

Figure 4.24 I_D/I_G ratios of the synthesized MWCNTs at different synthesizing temperatures.

The I_D/I_G ratios revealed that the synthesizing temperature strongly affected on crystallinity and purity of the synthesized carbon nanoparticles. At the synthesizing temperature of 800 °C, the I_D/I_G ratios of the carbon nanoparticles deposited at zone 1, zone 2 and zone 3 were 0.24, 0.21 and 0.22, respectively. It could be clearly observed that, at the synthesizing temperature of 850 °C, the I_D/I_G ratios of the carbon nanoparticles were few decreased compared to those synthesized at the temperature of 800 °C. At the synthesizing temperature of 850 °C, the I_D/I_G ratios carbon nanoparticles deposited at zone 1, zone 2 and zone 3 were 0.18, 0.19 and 0.19, respectively. While, at the synthesizing temperature of 900 °C, the I_D/I_G ratio of the carbon nanoparticles at zone 1 and zone 3 were nearly the same as those of

synthesizing at the temperatures of 800 and 850 °C which reported above. However, the I_D/I_G ratio of the carbon nanoparticles at zone 2 was significantly increased at the ratio of 0.44. Therefore, in this work, the synthesizing temperature of 850 °C was found to be the optimal temperature for the synthesis of the CNTs.

From the experimental results, at the synthesizing temperature of 900 °C, the I_D/I_G ratio of the carbon nanoparticles at zone 2 was increased significantly because decomposition of glycerol was higher than that of the synthesizing temperature of 800 and 850 °C, leading to the Fe nanoparticles surrounded by higher amount of carbon atoms. These carbon atoms could diffuse continuously although the Fe catalyst was saturated by those former carbon atoms. Therefore, excess carbon atoms could not be dissolved into the Fe catalyst. Therefore, crystalline carbon could not be formed, leading to increase in the I_D/I_G ratio.

The carbon yields of the synthesized carbon nanoparticles at different synthesizing temperatures were shown in Figure 4.25. When the synthesizing temperature was increased from 800 to 850 and 900 °C, the carbon yield was increased from 2.2 to 3.0 and 3.6 %, respectively.

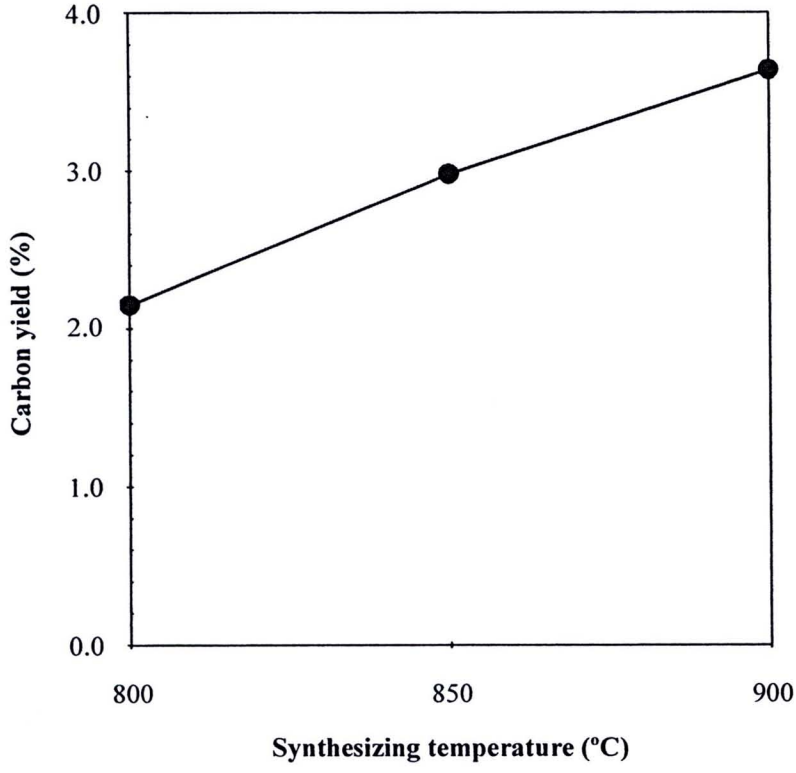

Figure 4.25 Yields of the synthesized carbon nanoparticles at different synthesizing temperatures

Lee et al., 2002 proposed alternative kinetic models of carbon nanoparticle formation and growth based on an assumption that the rate of the carbon nanoparticle formation could be assumed as a zero-order reaction. The rate constant of CNTs in equation 4.5 shows that increasing of synthesizing temperature makes increasing of rate constant of the CNTs as shown in Figure 4.26. Therefore, the increasing of the synthesizing temperature could promote the reaction rate of the formation of the CNTs which in term affected their yields.

$$-\ln k_{CNTs} = -3.8 + 1.51 \times \frac{10^4}{T} \tag{4.5}$$

where k_{CNTs} = Rate constant of the CNTs (min^{-1})

T = Synthesizing temperature (K)

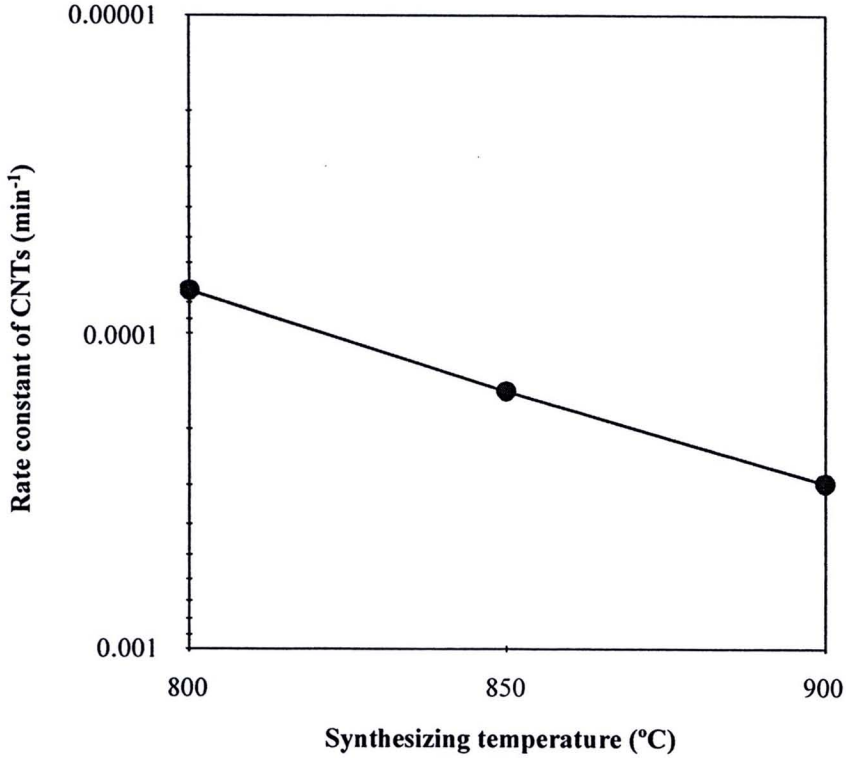

Figure 4.26 Rate constant of CNTs by varying synthesizing temperature

4.2.3 Effect of glycerol to ferrocene molar ratio

In this part, the effect of glycerol to ferrocene molar ratio on the quality and quantity of the synthesized carbon nanoparticles was studied at condition of synthesizing temperature of 800 °C and nitrogen flow rate of 350 mL/min.

Zone 1

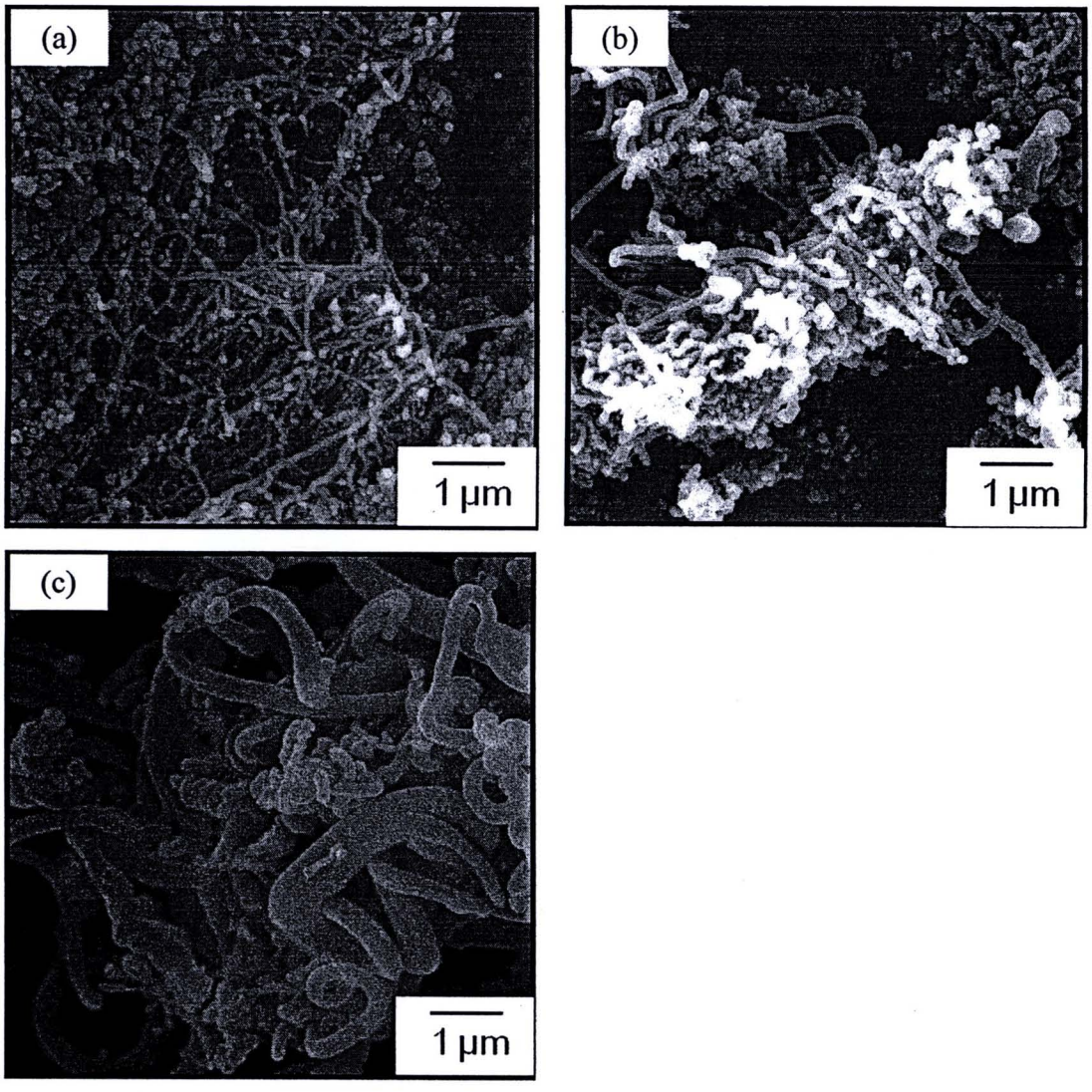

Figure 4.27 SEM images of the carbon nanoparticles deposited at zone 1 with different molar ratios of glycerol to ferrocene: (a) 5/1, (b) 10/1 and (c) 20/1.

SEM images as shown in Figure 4.27 revealed the carbon nanoparticles deposited at zone 1 with different molar ratios of glycerol to ferrocene. At the ratio of 5/1, the morphology of the synthesized carbon nanoparticles shown in

Figure 4.27(a) was uniform carpet-like MWCNTs with outer diameters of the tubes in range of 30-80nm. While, increasing of molar ratios of glycerol to ferrocene, the tubes with larger outer diameters were clearly observed. At the molar ratio of 10/1, the MWCNTs with outer diameter of the tubes in range of 50-125 nm were synthesized as shown in Figure 4.27(b). While at the molar ratio of 20/1, the tubes as shown in Figure 4.27(c) had the tube diameters larger than 250 nm.

Zone 2

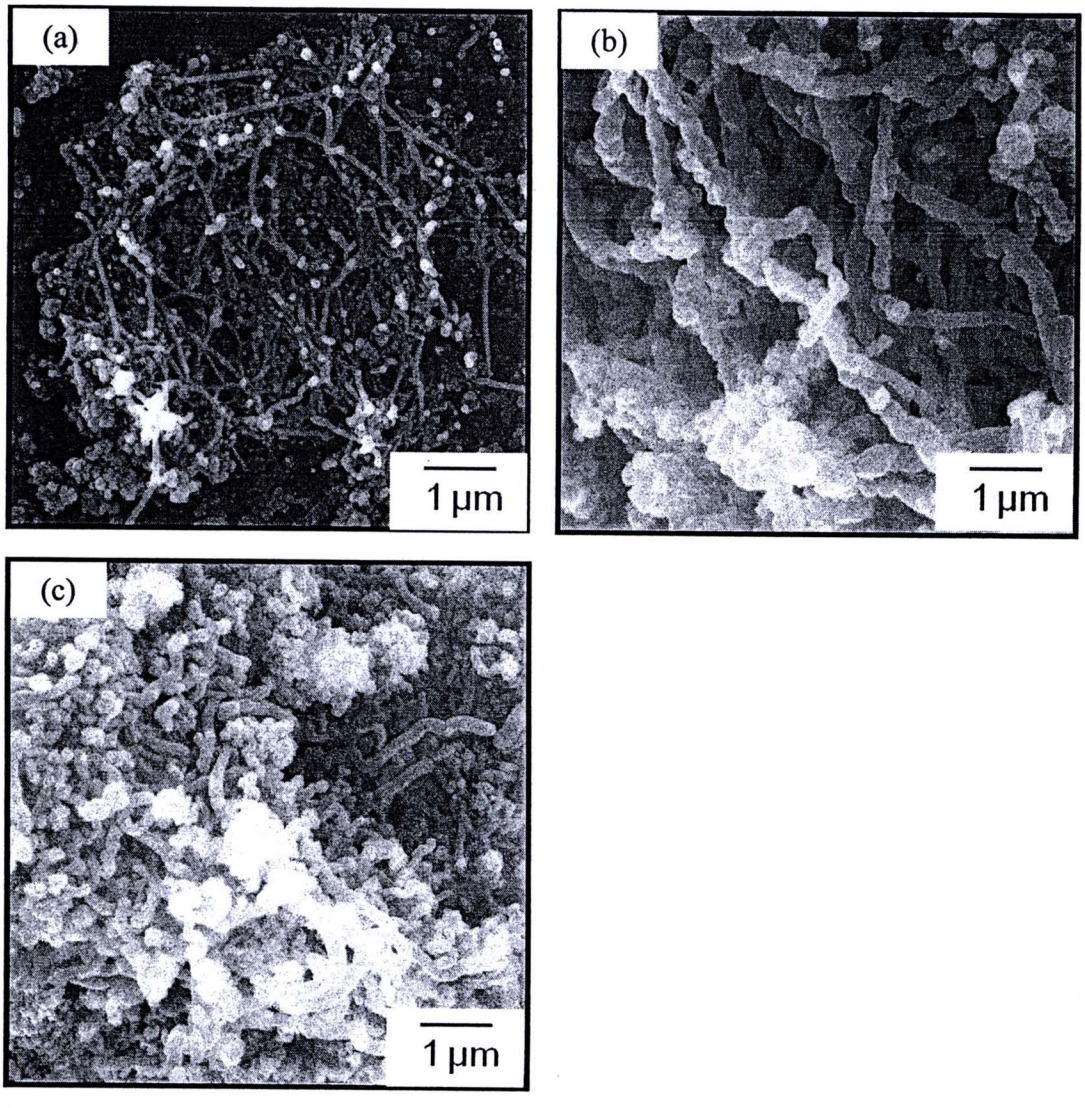

Figure 4.28 SEM images of the carbon nanoparticles deposited at zone 2 with different molar ratios of glycerol to ferrocene: (a) 5/1, (b) 10/1 and (c) 20/1.

SEM images as shown in Figure 4.28 revealed the carbon nanoparticles deposited at zone 2 with different molar ratios of glycerol to ferrocene.

At the ratio of 5/1, the synthesized carbon nanoparticles shown in Figure 4.28(a) were straight MWCNTs with outer diameters of the tubes in range of 40-80 nm. The MWCNTs at the ratio of 10/1 were synthesized which those outer diameters about 300 nm as shown in Figure 4.28(b). At the molar ratio of 20/1, the morphology of the synthesized carbon nanoparticles shown in Figure 4.28(c) was warm-like MWCNTs with outer diameters of the tubes in range of 100-250 nm, respectively.

Zone 3

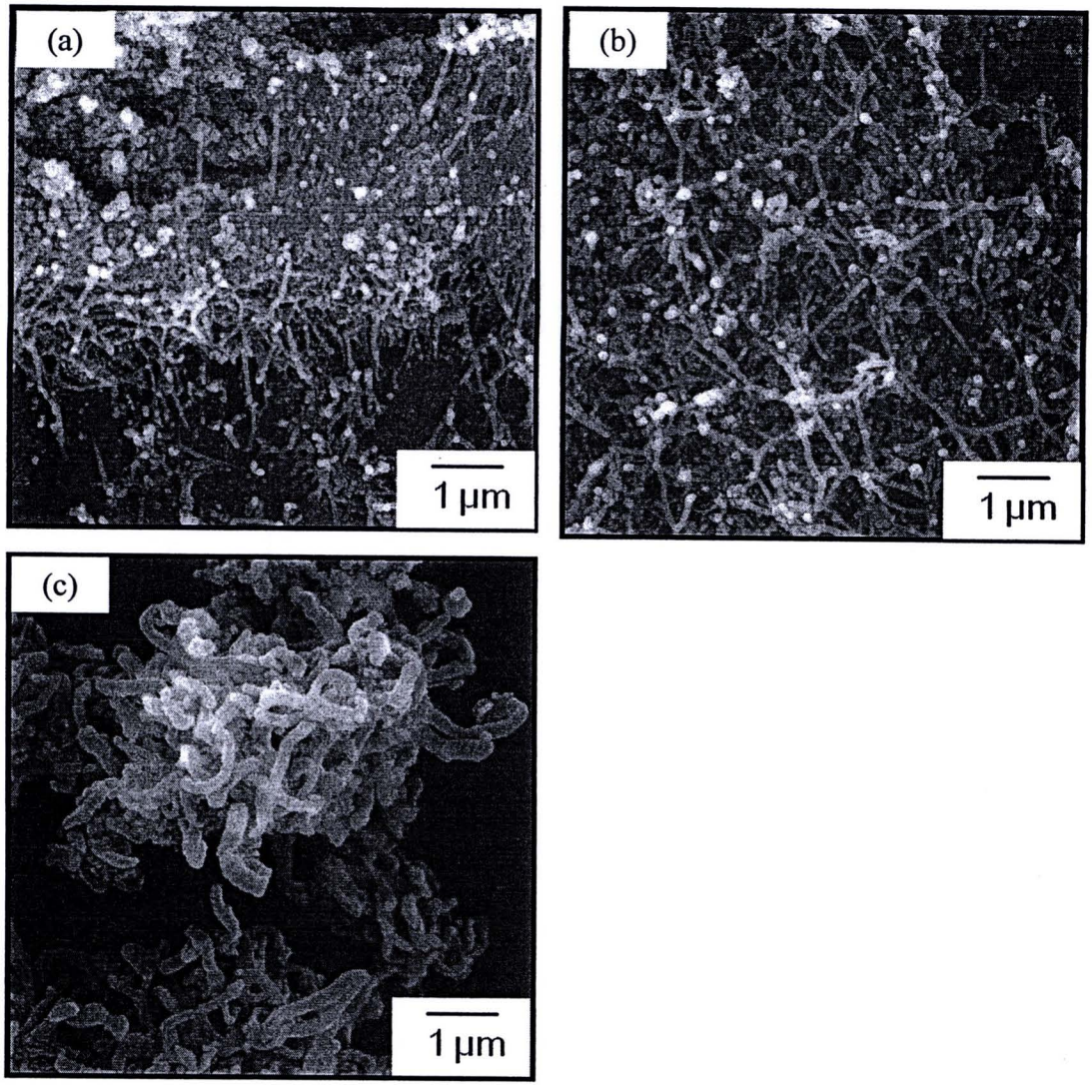

Figure 4.29 SEM images of the carbon nanoparticles deposited at zone 3 with different molar ratios of glycerol to ferrocene: (a) 5/1, (b) 10/1 and (c) 20/1.

SEM images the carbon nanoparticles deposited at zone 3 with different molar ratios of glycerol to ferrocene were shown in Figure 4.29. At the ratio

of 5/1, the morphology of the synthesized carbon nanoparticles shown in Figure 4.29(a) was the carpet-like MWCNTs with outer diameters of the tubes in range of 40-80 nm. The bigger diameters of the MWCNTs were synthesized at higher ratios of glycerol to ferrocene. At the ratio of 10/1, the straight MWCNTs with outer diameter of the tubes in range of 50-100 nm were synthesized as shown in Figure 4.29(b). While, at the ratio of 20/1, the curvature of MWCNTs with the outer diameters of the tubes about 125 nm were synthesized shown in Figure 4.29(c).

Raman spectra of the MWCNTs deposited at zone 1, zone 2 and zone 3 with different molar ratios of glycerol to ferrocene exhibited their strong responses of D peak and G peak. The I_D/I_G ratios of the synthesized MWCNTs with different molar ratios of glycerol to ferrocene were shown in Figure 4.30.

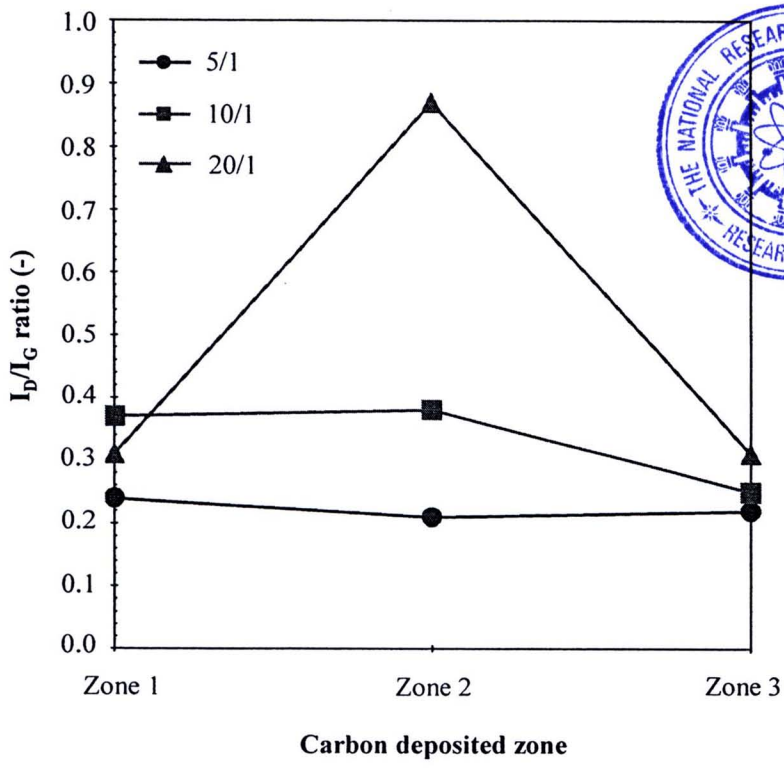

Figure 4.30 I_D/I_G ratios of the synthesized MWCNTs at different molar ratios of glycerol to ferrocene.

The I_D/I_G ratios revealed that the molar ratio of glycerol to ferrocene also strongly affected on crystallinity and purity of the synthesized carbon nanoparticles. At the molar ratio of 5/1, the I_D/I_G ratios of the carbon nanoparticles deposited at zone 1, zone 2 and zone 3 were 0.24, 0.21 and 0.22, respectively. It could

be observed that the I_D/I_G ratios of the carbon nanoparticles synthesized at higher ratio of glycerol to ferrocene were increased, especially the carbon nanoparticles deposited at zone 2 with the molar ratio of 20/1. At the molar ratio of 10/1, the I_D/I_G ratios of the carbon nanoparticles deposited at zone 1, zone 2 and zone 3 were 0.37, 0.38 and 0.25, respectively. While, at the molar ratio of 20/1, the I_D/I_G ratios of the carbon nanoparticles at zone 1, zone 2 and zone 3 were 0.31, 0.87 and 0.31, respectively. Therefore, in this work, the molar ratio of 5/1 was found to be the optimal ratio for the synthesis of the MWCNTs.

The carbon yields of the synthesized carbon nanoparticles at different molar ratios of glycerol to ferrocene were shown in Figure 4.31. At the molar ratio of glycerol to ferrocene was 5/1, the carbon yield was 2.2 %. The yield was decreased to 1.9 and 1.5 % when the molar ratio was increased to 10/1 and 20/1, respectively.

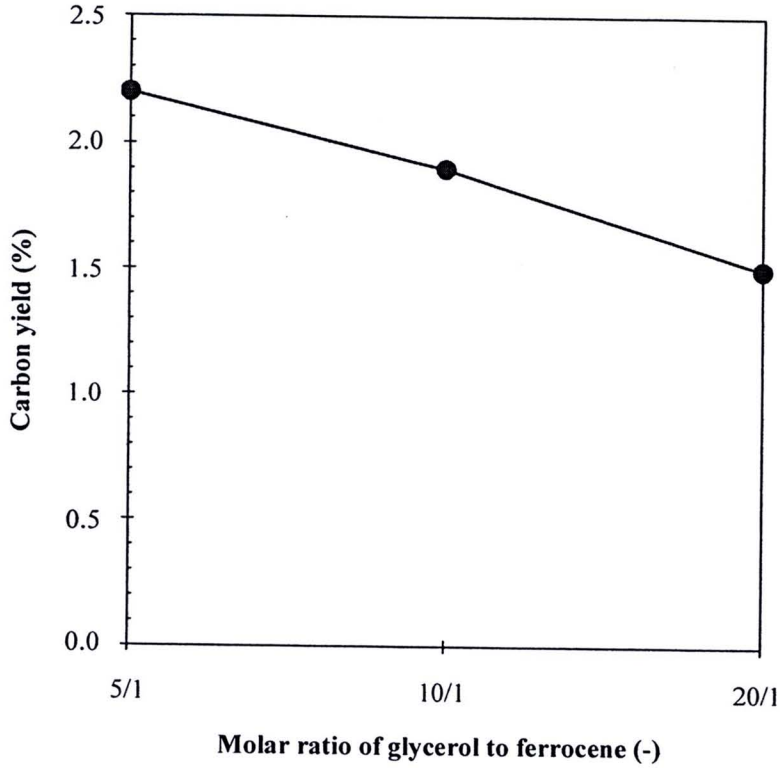

Figure 4.31 Yields of the synthesized carbon nanoparticles at different molar ratios of glycerol to ferrocene.

It is well known that catalytic nanoparticles such as Fe, Ni and Co and their mixture, are very important for the formation of the CNTs. The formation of the CNTs consists of diffusion and dissolution of carbon atom into the catalytic

nanoparticles, and precipitation to form the tubes, respectively. The diffusion and precipitation processes are competitor for each other. It means that if the diffusion process takes place with its rate slower than that of the precipitation process, the diffusion process is rate limiting step, leading to continuous CNT formation with less amount of amorphous carbon. On the other hand, the precipitation process is rate limiting step if the rate of precipitation takes place slower than the rate of diffusion. Therefore, at first, continuous feeding of the carbon atoms into the catalytic particles makes the formation of the CNTs with larger diameters. Finally, the continuous feeding leads excess amount of the carbon atoms into the catalytic nanoparticles. Therefore, the catalytic nanoparticles are not active, leading to the formation of shorter and larger diameters of the CNTs and also amorphous carbon can be taken place.

In this part, the C atoms were 15, 30 and 60 times to Fe atoms when the molar ratio of glycerol to ferrocene was 5/1 to 10/1 and 20/1, respectively which the atomic ratio of C to Fe was significantly increased. At higher molar ratio of glycerol and ferrocene, especially in case of the ratio of 20/1, the carbon atoms was too much, leading to the tubes had larger diameters and shorter than those at the molar ratio of 5/1. Therefore, it was possible to conclude that the formation of the MWCNTs at the ratio of 20/1 was controlled by the precipitation process which could be confirmed by SEM images and the I_D/I_G ratios.

Although diffusion of the C atoms was increased at higher molar ratio of glycerol to ferrocene, the yield of the synthesized carbon products was decreased. The increasing of the C atoms with the same of the Fe atoms increased the diffusion rate of the C atoms. When the diffusion was much faster than the precipitation of the C atoms to form the tubes, poisoning of the Fe particles took place, which the Fe particles were not activate the C atoms to form the tube. The remaining of the C atoms could not dissolve into the Fe particles, leading to, the tubes were not formed. Therefore, the yield of the synthesized products was decreased at higher molar ratio of glycerol to ferrocene.

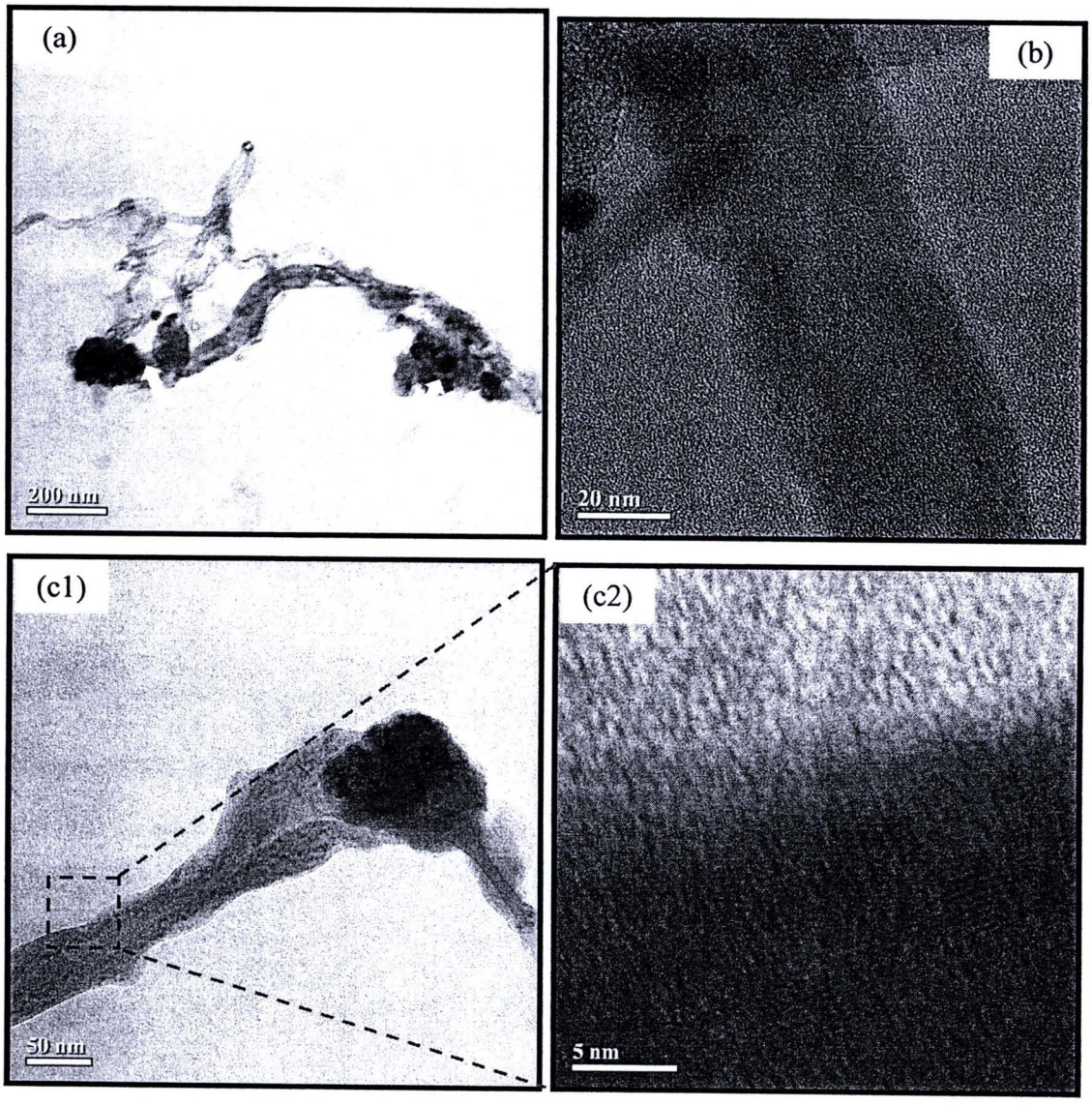

Figure 4.32 TEM images of the synthesized MWCNTs under the condition of the nitrogen flow rate of 350 mL/min, the synthesizing temperature of 800 °C and the molar ratio of glycerol to ferrocene of 5/1 at different deposited positions: (a) zone 1, (b) zone 2 and (c1) and (c2) zone 3.

TEM images of the MWCNTs deposited at different positions within the quartz tube reactor were shown in Figure 4.32. Fe nanoparticles, indicated with arrowhead, were at the one tip of the MWCNTs. High magnified TEM image of the MWCNTs as shown Figure 4.32(c2) revealed the tubes were made of parallel graphene planes oriented along the tube axis with the interplanar distance between two adjacent graphene planes about 0.34 nm which is close to that of the (002) interplanar distance in graphite, i.e. 0.335 nm. Furthermore, it could be clearly observed the amorphous carbon covered on the outer wall of the tubes.

XRD patterns of the synthesized MWCNTs shown in Figure 4.33 consisted of X-ray diffraction peak at 26.3° could be assigned to the (002) planes of hexagonal graphite structure with an interplanar distance of 0.35 nm while another peak at 43.7 ° indicates that the iron nanoparticles exhibited the (111) plane of the face-centered cubic (fcc) γ-Fe. In addition, it could also be observed the existence of Fe were body-centered cubic (bcc) α-Fe (110) at 44.7° (Cheng et al., 2009). Furthermore, a large fraction of orthorhombic cementite Fe_3C phase was also found in the XRD patterns.

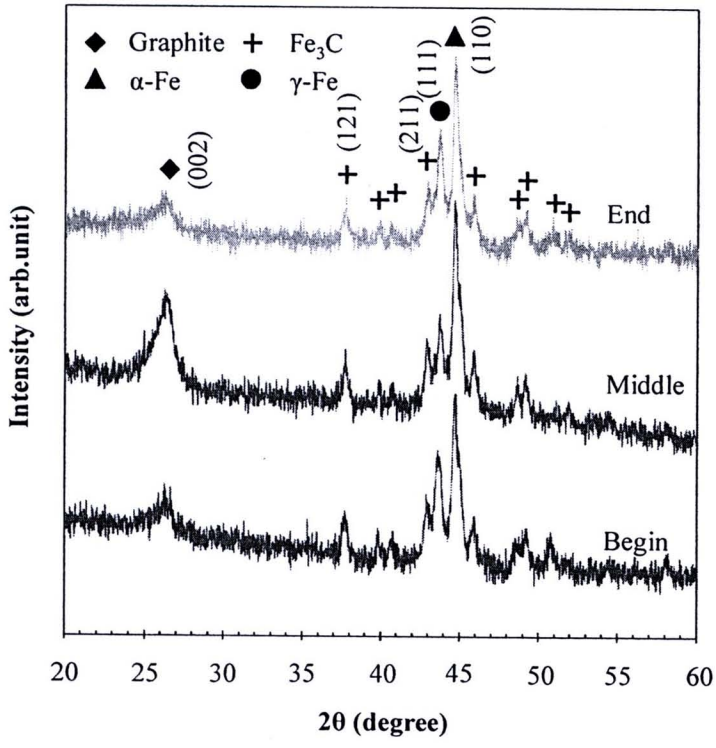

Figure 4.33 XRD patterns of the synthesized MWCNTs under the condition of the nitrogen flow rate of 350 mL/min, the synthesizing temperature of 800 °C and the molar ratio of glycerol to ferrocene of 5/1 at different deposited positions.

From Fe-C phase diagram as shown in Figure 4.34, it could be clearly seen that γ-Fe (in γ phase and γ + Fe_3C phase) were mostly transformed into α-Fe during the cooling down phase because α-Fe is the thermodynamically stable phase at room temperature (Cheng et al., 2009). This phenomenon was consistent with the appearance of small fraction of the γ-Fe compared to the α-Fe in the XRD patterns as shown in Figure 4.33. While the Fe_3C is not stable at high temperature, therefore, the decomposition of the carbide into α-Fe and C atoms was occur, leading to the

precipitation of the C atoms to form the CNTs at the surface of the Fe particles (Snoeck, Froment and Fowles, 1997).

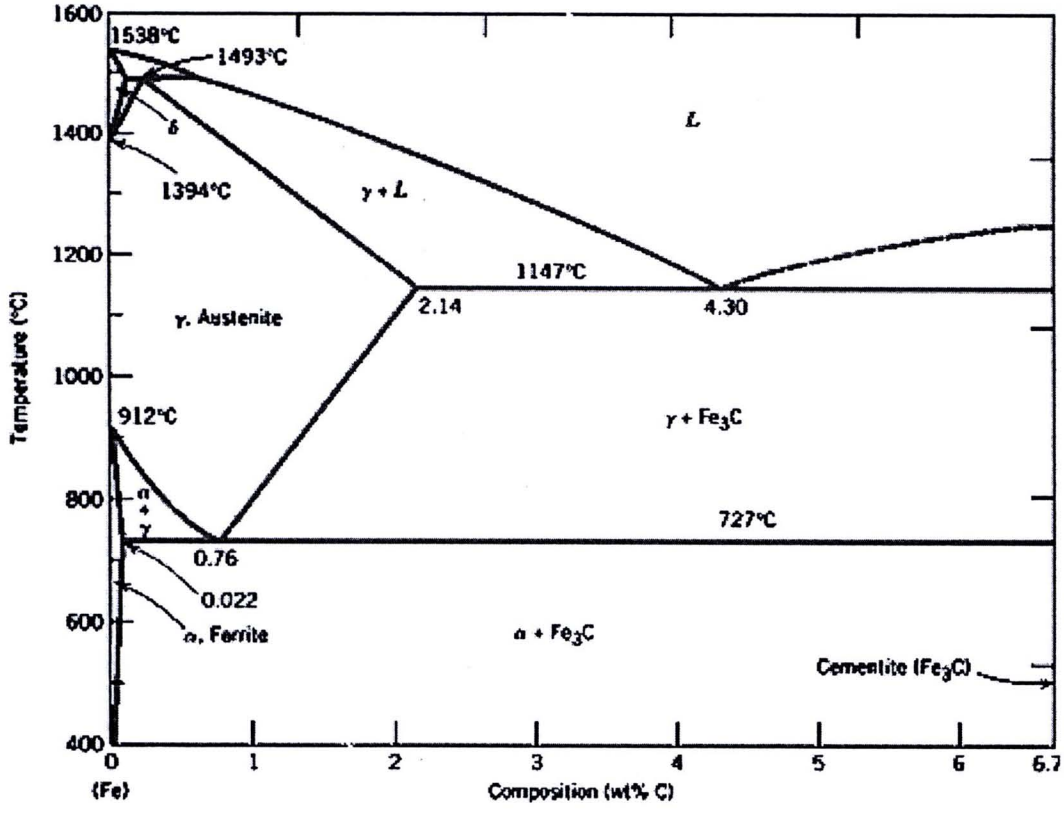

Figure 4.34 Fe-C phase diagram (http://www.docstoc.com/docs/56224939/Iron-Carbon-Phase-Diagram-(a-review)-see-Callister-Chapter-9).

4.2.4 Possible mechanisms

Based on above experimental results, it could be realized that the formation mechanisms of the carbon nanoparticles was strongly dependence on the existence of the Fe catalytic nanoparticles generated from decomposition of ferrocene as well as their diffusion, dissolution and precipitation processes. The formation mechanisms, proposed here, was believed that vapor-liquid-solid (VLS) growth mechanisms of carbon catalyzed by molten Fe nanoparticles consists of diffusion, dissolution and precipitation of the carbon atoms (Weissker et al., 2010) as shown in Figure 4.35. At first, the mixture of glycerol and ferrocene as the carbon and Fe precursors was vaporized by heat transfer from the electrical furnace. The vaporized

precursors were instantly introduced by nitrogen gas into the maximum temperature zone, simultaneously with decomposition of the vaporized precursors to form carbon and Fe vapors. The Fe vapors initially formed nuclei, after that the nuclei condensed and coagulated to form molten Fe particles, respectively. The C vapors around the molten Fe diffused on the surface of the molten Fe and dissolved until saturation inside the Fe particles, leading to form γ-Fe and an intermetallic compound of metastable Fe_3C in carbon diffusion, dissolution and saturation of carbon process, respectively. The γ-Fe and Fe_3C were then transformed and decomposed into α-Fe and C atoms, respectively. Finally, the C atoms were precipitated to form the CNTs at the surface of the Fe particles.

Referring to these experimental results of the synthesis of the SWCNTs by laser ablation of C/Ni/Co rod and the MWCNTs by CVD of glycerol and ferrocene, it could be clearly observed that the formation mechanisms of both CNTs (SWCNTs and MWCNTs) were vapor-liquid-solid (VLS) mechanisms, although their carbon and catalyst sources were produced differently. Furthermore, it also revealed that the formation mechanisms of the CNTs consist of the diffusion, dissolution and precipitation processes. The dissolution of the C atoms into the catalytic metals was related to solubility of the C atoms into the metals to form carbon-metal alloys. Therefore, selection of proper catalyst for the synthesis of the CNTs was significantly considered.

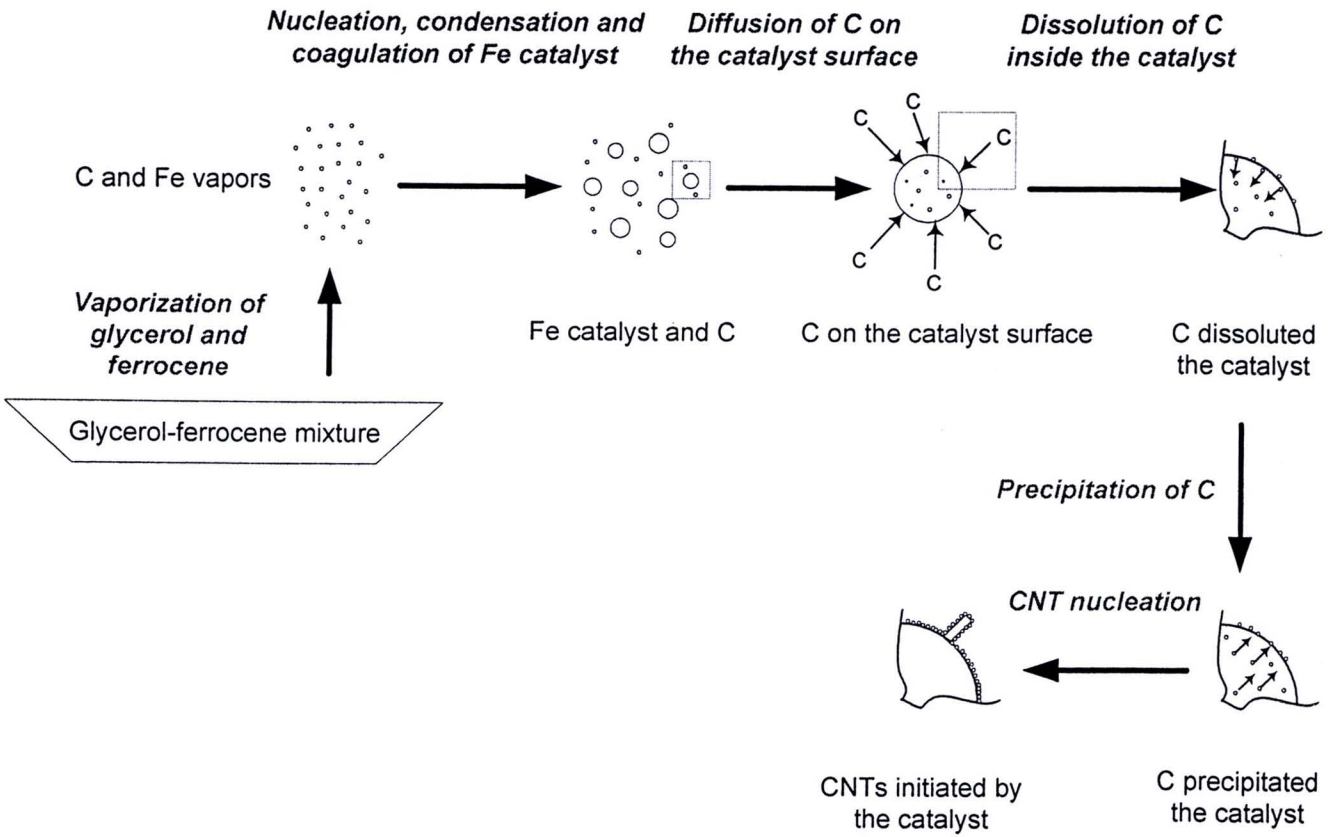

Figure 4.35 Vapor-liquid-solid mechanisms of the formation of the MWCNTs by CVD of glycerol and ferrocene.

4.3 Synthesis of the ZnO nanoparticles by oxidation of Zn

Referring to many experimental results reported in other previous works, this part has set its aim to study effect of synthetic parameters on the morphology, size and yield of the ZnO nanoparticles synthesized by the oxidation of pure Zn powder. Effect of synthesizing temperature, nitrogen flow rate and oxygen flow rate on the morphology, size and yield of the synthesized ZnO nanoparticles were thoroughly investigated and then reported and discussed in this part.

From the previous part of the synthesis of the carbon nanoparticles (see page 56), it could be clearly observed that the temperature gradients and velocity gradients took place throughout the quartz tube reactor and could affect on the formation of the carbon nanoparticles, leading to the study of the synthesized carbon nanoparticles at 3 different zones including zone 1 (0-15 cm from inlet) where the temperature increased from the lowest to the highest, zone 2 (15-45 cm from inlet) where the temperature was the highest and zone 3 (45-60 cm from inlet) where the temperature decreased from the highest to the lowest. In this part, the temperature gradients and velocity gradients could also affect on the formation of the ZnO nanoparticles. Therefore, the synthesized ZnO nanoparticles were also distinguish studied into 3 zones as zone 1, zone 2 and zone 3. However, it should be noted that few ZnO nanoparticles deposited at zone 1. Therefore, in this part, the synthesized ZnO nanoparticles were only studied at zone 2 and zone 3.

4.3.1 Effect of nitrogen flow rate

The effect of nitrogen flow rate on the formation of the synthesized ZnO nanoparticles was studied in a range of 200, 350 and 500 mL/min under condition of the synthesizing temperature of 800 °C and O_2 flow rate of 100 mL/min.

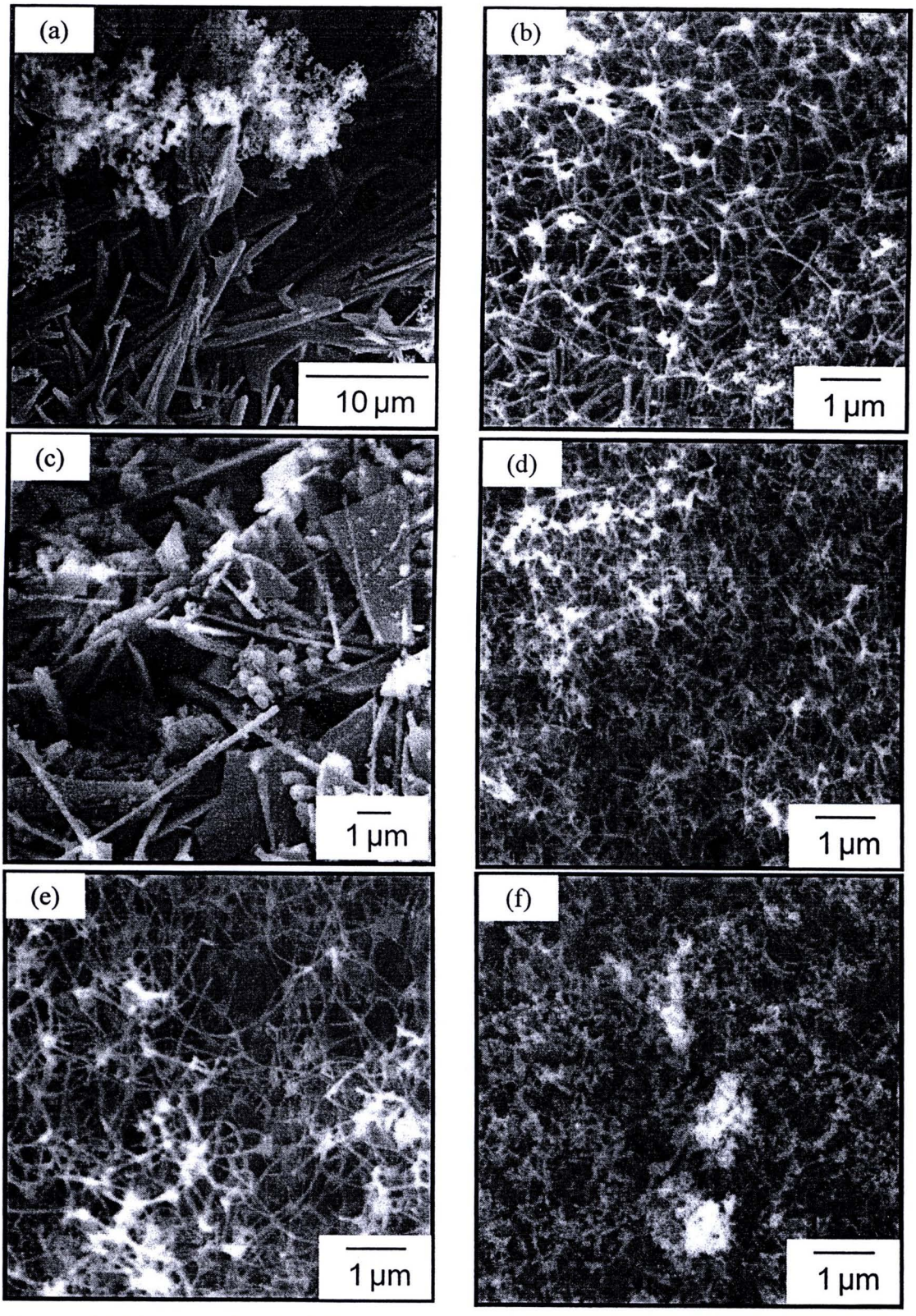

Figure 4.36 The synthesized ZnO deposited at zone 2 and zone 3 with different N_2 flow rates: (a) and (b) 200 mL/min, (c) and (d) 350 mL/min and (e) and (f) 500 mL/min.

Morphologies of the ZnO nanoparticles deposited at the zone 2 and zone 3 with different nitrogen flow rates were shown in Figure 4.36. At nitrogen flow rate of 200 mL/min, the synthesized ZnO deposited at zone 2 as shown in Figure 4.36(a) was rod-like microstructure with the diameter about 100 nm and the length more than 10 um. Furthermore, few amount of agglomerated nanoparticle was also found. While, the synthesized ZnO deposited at zone 3 as shown in Figure 4.36(b) was uniform tetrapod nanostructure with the diameters and length of pod about 60-80 nm and 500-600 nm, respectively.

At nitrogen flow rate of 350 mL/min, the morphology of ZnO deposited at zone 2 as shown in Figure 4.36(c) was combination of various structures including spherical particles with diameters more than 200 nm, rod-like microstructure with the diameter about 100 nm and the length more than 5 um and micro-sheets. While, the ZnO deposited at zone 3 as shown in Figure 4.36(d) was uniform tetrapod nanostructure with the diameters and length of pod about 50-60 nm and 320-340 nm, respectively.

At nitrogen flow rate of 500 mL/min, the morphology of ZnO deposited at zone 2 and zone 3 as shown in Figure 4.36(e) and (f), respectively was the same morphology of tetrapod ZnO. However, their diameter and length were significantly different. The diameter and length of the ZnO deposited at zone 2 were about 30-40 nm and more than 800 nm, respectively. While those of the ZnO deposited at zone 3 were about 50-60 nm and 160-180 nm, respectively.

It could be clearly observed that the nitrogen flow rate affected on the morphologies of the ZnO deposited on the zone 2 of the quartz tube reactor. While the nitrogen flow rate did not affect on the morphology but on the diameters and length of the tetrapod ZnO deposited at zone 3 which were significantly decreased.

ZnO yields could be defined in equation 4.6

$$\text{ZnO yield}(\%) = \frac{W_{ZnO,2} + W_{ZnO,3}}{W_{Zn}} \times 100 \qquad (4.6)$$

where $W_{ZnO,2}$ = Weight of synthesized ZnO at zone 2

$W_{ZnO,3}$ = Weight of synthesized ZnO at zone 3

Yields of the synthesized ZnO nanoparticles at different nitrogen flow rates were shown in Figure 4.37. At the nitrogen flow rate of 200 mL/min, the ZnO yield was 61 %. While the yield significantly decreased as 52 and 37 % at the nitrogen flow rate of 350 and 500 mL/min, respectively.

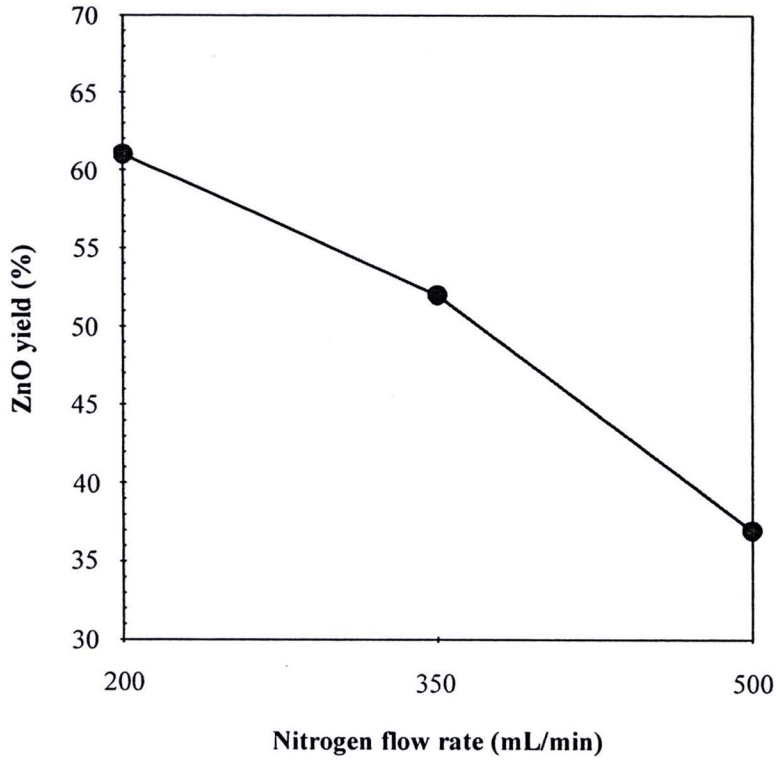

Figure 4.37 Yields of the synthesized ZnO nanoparticles at different nitrogen flow rates.

The nitrogen flow rate was found to be a main parameter of this study which direct affected to the formation of the synthesized ZnO nanostructures. Increase in the nitrogen flow rate decreased residence time within the quartz tube reactor. Furthermore, increase in the nitrogen flow rate also diluted oxygen, leading to partial pressure of oxygen was decreased.

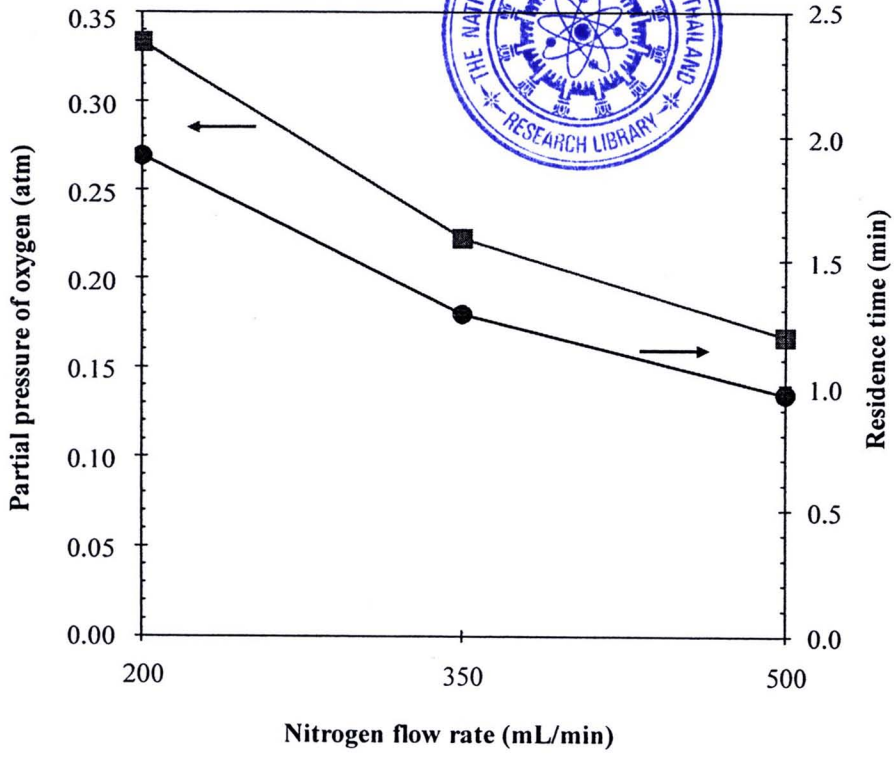

Figure 4.38 Partial pressure of oxygen and residence time by varying nitrogen flow rate.

The partial pressure of oxygen inside the quartz tube reactor was decreased from 0.33 to 0.22 and 0.17 atm, while residence time was also decreased from 1.9 to 1.3 and 1.0 min when the nitrogen flow rate was increased from 200 to 350 and 500 mL/min, respectively as shown in Figure 4.38.

The ZnO could be synthesized by oxidation of zinc as shown in equation 4.7.

$$Zn\ (s) + 1/2O_2 \rightarrow ZnO\ (s) \qquad (4.7)$$

From kinetic consideration (Delalu et al., 2000), conversion of the synthesized ZnO from the oxidation can be defined by expression 4.8.

$$\alpha = \frac{m^0_{Zn} - m^t_{Zn}}{m^0_{Zn}} \qquad (4.8)$$

where α = Conversion of the ZnO

m_{Zn}^{0} = Initial mass of zinc (t = 0)

m_{Zn}^{t} = Mass of zinc at time t (t > 0)

The experiments were assumed isothermally. Furthermore, Zn was also approximated as spherical particles. Under the conditions, designation by r_0, r_1 and r_2, the initial radius of Zn particle, of the reaction interface (metal/oxide) and of the oxide layer, respectively as shown in Figure 4.39.

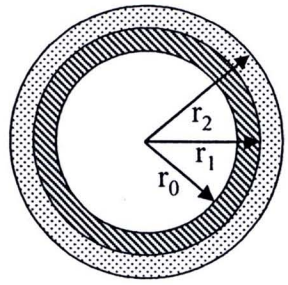

Figure 4.39 Diffusion of oxygen through Zn spherical particle.

We demonstrate the following relations:

$$r_1 = r_0(1-\alpha)^{1/3} \tag{4.9}$$

$$r_2 = r_0(1+\alpha(\Delta-1))^{1/3} \tag{4.10}$$

$$\Delta = \frac{V_{ZnO}}{V_{Zn}^{0} - V_{Zn}} \tag{4.11}$$

where Δ = Coefficient of Pilling and Bedworth (Moore et al., 1962)

V_{ZnO} = Volume of ZnO

V_{Zn}^{0} = Initial volume of Zn

V_{Zn} = Volume of Zn

The conversion, α, could be derived with respect to time as shown in equation 4.12.

$$\frac{d\alpha}{dt} = -\frac{2}{m_{Zn}^{0}} \frac{dm_{O_2}}{dt} \tag{4.12}$$

Assuming, the diffusion of the reactants through the thickness of the oxide layer was the limiting factor. Fick's Law of O_2 as shown in equation 4.13, respectively are substituted into equation 4.12.

$$N_{O_2} S_1 = -D_{O_2} S_1 \left\{ \frac{dC_{O_2}}{dr} \right\}_{r=r_1} \tag{4.13}$$

where N_{O_2} = Diffusion flux of O_2

D_{O_2} = Diffusion coefficient

S_1 = Surface area of the reaction interface = $4\pi r_1^2$

$\left\{ \frac{dC_{O_2}}{dr} \right\}_{r=r_1}$ = Local concentration gradient of O_2

Therefore, equation 4.12 could be reduced into following rate equation as shown in equation 4.14:

$$\frac{d\alpha}{dt} = \frac{2}{m_{Zn}^{0}} D_{O_2} 4\pi r_1^2 \left\{ \frac{dC_{O_2}}{dr} \right\}_{r=r_1} \tag{4.14}$$

The relation could be integral if r_1 and the concentration gradient of O_2 at $r = r_1$ are expressed as function of α. From the lack of accumulation of reactant in the reaction zone (steady-state hypothesis), equation 4.14 could be deduced into equation 4.15.

$$r^2 \left\{ \frac{dC_{O_2}}{dr} \right\} = r_1^2 \left\{ \frac{dC_{O_2}}{dr} \right\}_{r=r_1} \tag{4.15}$$

From the limiting conditions;

(i) $C_{O_2} = C^{i}_{O_2} = 0$ for $r = r_1$ where i is initial condition

(ii) $C_{O_2} = C^{e}_{O_2}$ for $r = r_2$ where e is equilibrium condition

Therefore, local concentration gradient of O_2 could be deduced as shown in equation 4.16.

$$\left\{\frac{dC_{O_2}}{dr}\right\}_{r=r_1} = \frac{r_2}{r_1(r_2 - r_1)} C^{e}_{O_2} \tag{4.16}$$

Substitution of equation 4.16 into equation 4.14, a differential equation dependence only on the variables α and t could be obtained as shown in equation 4.17.

$$\frac{d\alpha}{dt} = \frac{8\pi D_{O_2} C^{e}_{O_2}}{m^{0}_{Zn}} \left[\frac{1}{r_0(1-\alpha)^{1/3}} - \frac{1}{r_0(1-\alpha(\Delta-1))^{1/3}}\right] \tag{4.17}$$

After integration, the final equation could be obtained as shown in equation 4.18.

$$\frac{\Delta}{\Delta-1} - (1-\alpha)^{2/3} - \frac{1}{\Delta-1}[1+\alpha(\Delta-1)]^{2/3} = \frac{D_{O_2} C^{e}_{O_2}}{d_{Zn} r_0^2} \tau \tag{4.18}$$

where d_{Zn} = Density of Zn

One can define:

$$k^{0}_{Zn} = \frac{D_{O_2} C^{e}_{O_2}}{d_{Zn} r_0^2} \tag{4.19}$$

k_{Zn}^{0} is proportional to the diffusion constant, could be related to the observed rate constant of the reaction (Delalu et al., 2000). Therefore, the time necessary to totally consume Zn ($\alpha = 1$) was equal to:

$$\tau = \frac{1}{k_{Zn}^{0}} \frac{\Delta}{\Delta - 1} \left[1 - \frac{[1 + \alpha(\Delta - 1)]^{2/3}}{\Delta} \right] \tag{4.20}$$

The necessary time as shown in equation 4.20 was function of various parameters including conversion of the ZnO or α. Therefore, increase in nitrogen flow rate or decrease in residence time resulted in lower diffusion of O_2 into the surface of the Zn spherical particles, leading to decrease in diameters and length of the ZnO pods.

4.3.2 Effect of synthesizing temperature

In this part, the effect of synthesizing temperature at 800, 850 and 900 °C on the formation of the synthesized ZnO was studied at constant N_2 flow rate of 500 mL/min and O_2 flow rate of 100 mL/min.

At synthesizing temperature of 800 °C, the ZnO deposited at zone 2 shown in Figure 4.40(a) was tetrapod ZnO structure with diameters and length of pod about 30-40 nm and more than 800 nm, respectively. While, the ZnO deposited at zone 3 as shown in Figure 4.40(b) was also tetrapod nanostructure with smaller diameters and shorter length of pod about 50-60 and 160-180 nm, respectively.

As same as the results of the ZnO synthesized at the synthesizing temperature of 800 °C, the morphology of the synthesized ZnO at the synthesizing temperature of 850 °C was also tetrapod ZnO structure shown in Figure 4.40(c) and (d). The diameters and length of the pod from the zone 2 as shown in Figure 4.40(c) were about 100 nm and 500-600 nm, respectively. While, those of the pod at zone 3 as shown in Figure 4.40(d) were about 50-60 and 440-560 nm, respectively.

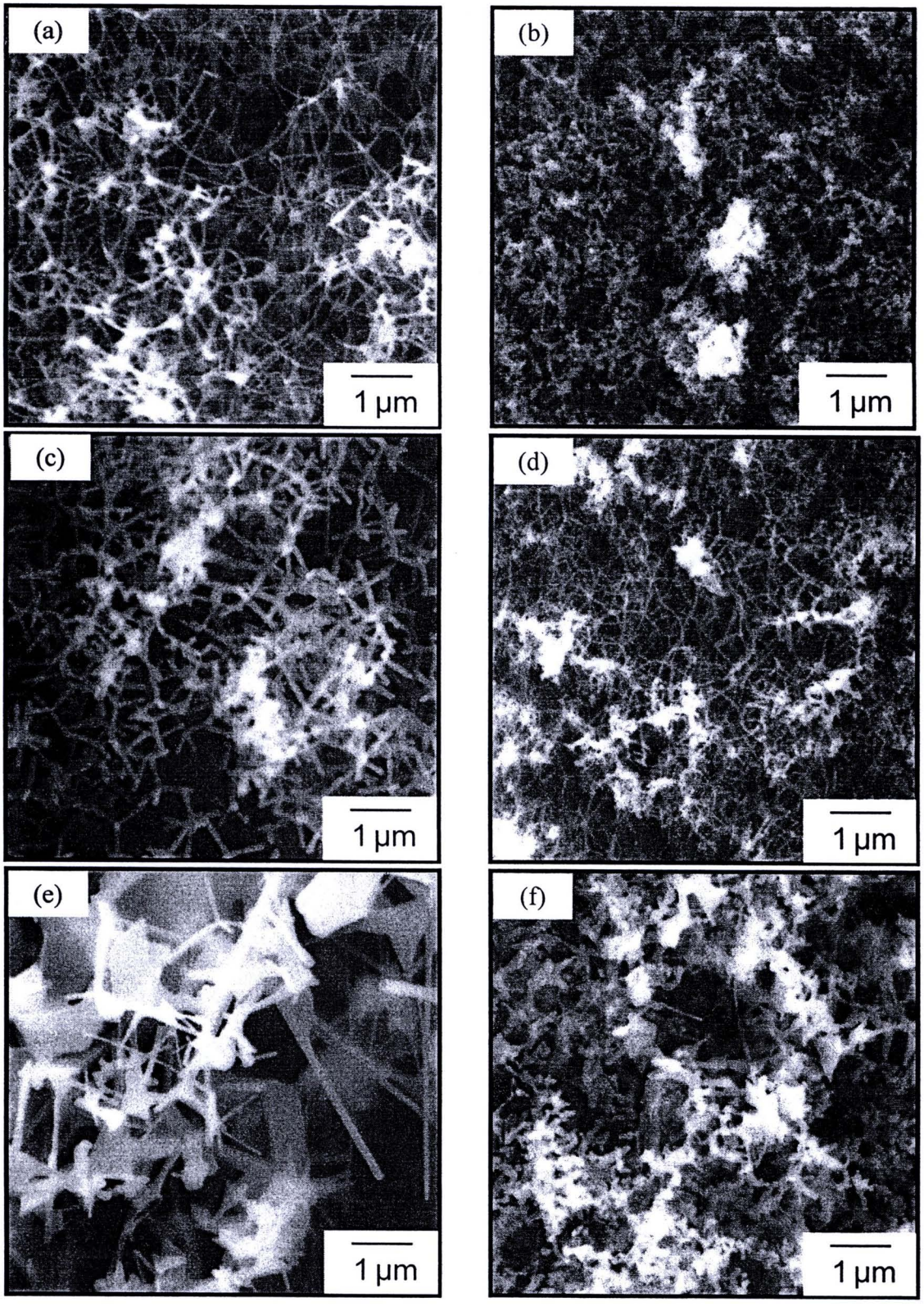

Figure 4.40 The synthesized ZnO deposited at zone 2 and zone 3 with different synthesizing temperatures: (a) and (b) 800 °C, (c) and (d) 850 °C and (e) and (f) 900 °C.

At synthesizing temperature of 900 °C, the morphology of the ZnO deposited at zone 2 and zone 3 as shown in Figure 4.40(e) and (f), respectively were significantly different. The morphology of the ZnO deposited at zone 2 shown in Figure 4.40(e) was combination of various structures such as rod-like structure with the diameters about 100 nm and length about 3 um, micro-sheets and tetrapod structure. These might be caused by overgrowth of lamellae (Zhou, Liu and Hu, 2005) which can take place at high synthesizing temperature. While the morphology of ZnO deposited at zone 3 as shown in Figure 4.40(f) was agglomerated particles with primary diameters about 100-200 nm. Furthermore, few amount of rod-like structure was also found.

It was clearly observed that the ZnO deposited at zone 2 and zone 3 was still tetrapod structure although the synthesizing temperature was increased from 800 to 850 °C. However, the increasing of these temperatures resulted inn increasing of the diameters and length of the pod of ZnO. While the morphologies of the ZnO synthesized at the synthesizing temperature of 900 °C was significant changed.

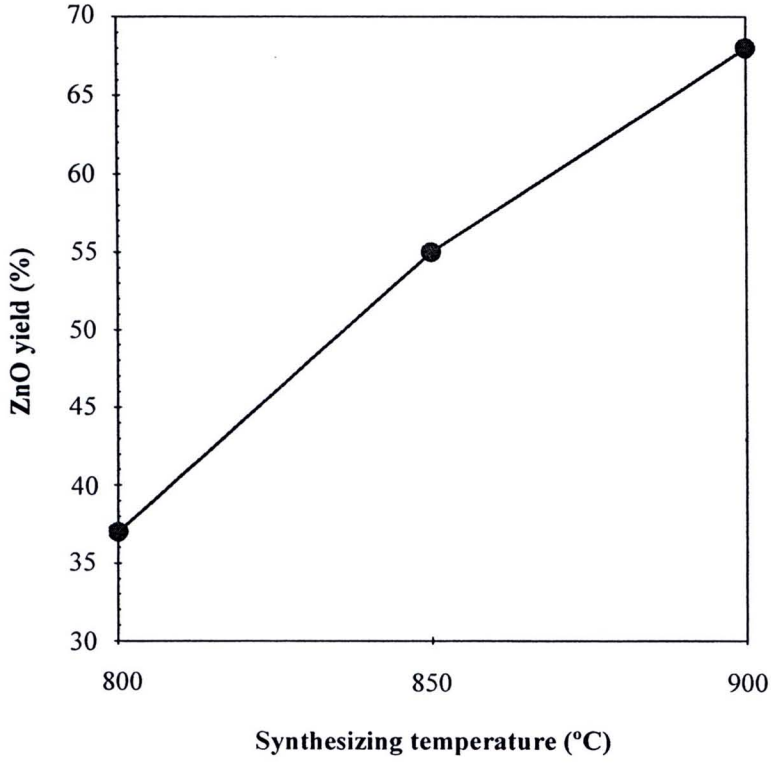

Figure 4.41 Yields of the synthesized ZnO nanoparticles at different synthesizing temperatures

Yields of the synthesized ZnO nanoparticles at different synthesizing temperatures were shown in Figure 4.41. At the synthesizing temperature of 800 °C, the ZnO yield was 37 %. While the yield significantly increased as 55 and 68 % at the synthesizing temperatures of 850 and 900 °C, respectively.

Rate constant of zinc oxidation (Delalu et al., 2000) shown in equation 4.21 revealed that increase in the synthesizing temperature exhibited rate constant of zinc as shown in Figure 4.42. Therefore, the increase in the synthesizing temperature could promote the reaction rate of ZnO formation.

$$-\ln k_{Zn} = -10.3 + 1.56 \times \frac{10^4}{T} \qquad (4.21)$$

where k_{Zn} = Rate constant of zinc oxidation (min^{-1})

T = Synthesizing temperature (K)

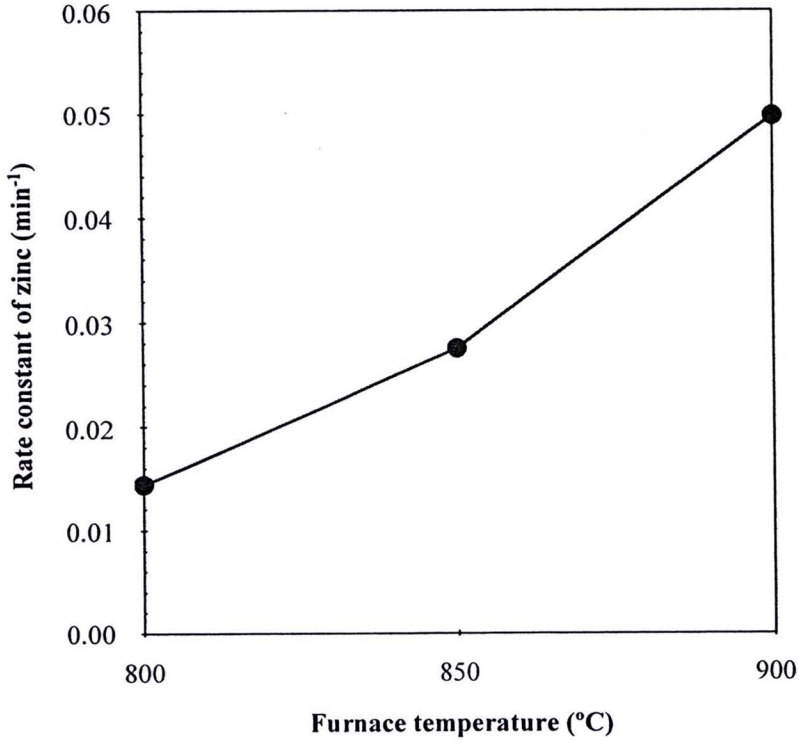

Figure 4.42 Rate constant of zinc by varying synthesizing temperature.

From above experimental results, morphology of synthesized ZnO nanoparticles changed from tetrapod structure to combination of various structures

such as rod-like structure, micro-sheet and tetrapod structure as shown in Figure 4.40(e) and agglomerated particles with rod like structure as shown in Figure 4.40(f) when the synthesizing temperature were changed from 800 and 850 °C to 900 °C. Therefore, morphology, size and yield of the synthesized ZnO depend upon partial pressure of zinc vapor and kinetic reaction of ZnO.

4.3.3 Effect of oxygen flow rate

In this part, the effect of oxygen flow rate on the formation of the synthesized ZnO was studied at N_2 flow rate of 500 mL/min and synthesizing temperature of 800 °C.

From SEM images as shown in Figure 4.43, morphology of the synthesized ZnO was also tetrapod nanostructure although the oxygen flow rate was increased from 100 to 150 mL/min. At oxygen flow rate of 100 mL/min, the diameter and length of pod deposited at zone 2 were about 30-40 nm and 800 nm, respectively as shown in Figure 4.43(a). The diameter and length of the pods deposited at zone 3 were in range of 50-60 nm and 160-180 nm, respectively as shown in Figure 4.43(b).

At oxygen flow rate of 150 mL/min, the diameter and length of pod deposited at zone 2 were about 50-60 nm and 310-370 nm, respectively as shown in Figure 4.43(c). The diameters and length of pod deposited at zone 3 were about 35-55 nm and 140-150 nm, respectively as shown in Figure 4.43(d).

From these results, it could be clearly observed that the oxygen flow rate only affected on the size of the ZnO deposited on the zone 2 and zone 3 of the quartz tube reactor. Based on the assumption of oxygen diffusion into Zn spherical particle shown in Figure 4.39, diffusion rate of oxygen at higher oxygen flow rate were faster. Therefore, nucleation process was relative high rate, leading to more generated nuclei. Under this condition, the lateral growth of the originally formed oxide particles is inhibited to a certain degree, resulting in small oxide size. On the other hand, the supply of oxygen to the surface of the Zn particle was highly limited under lower oxygen partial pressure since there was little oxygen in the atmosphere. Therefore, the surface reaction will be dominated by the continuing growth of the oxide particles already formed, leading to a relatively larger size (Gao et al., 2003).

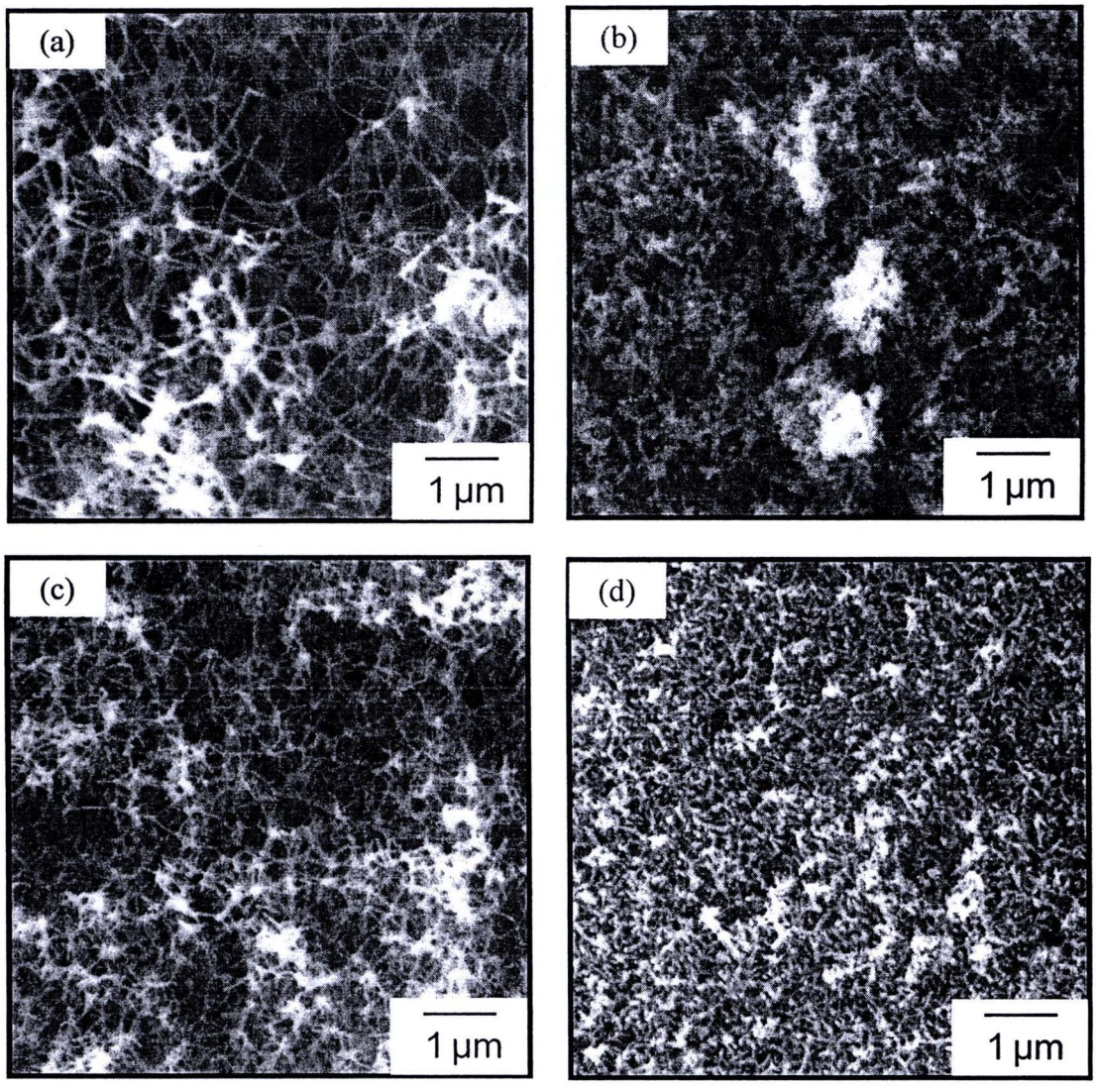

Figure 4.43 The synthesized ZnO deposited at zone 2 and zone 3 with different O_2 flow rates: (a) and (b) 100 mL/min, (c) and (d) 150 mL/min.

TEM image as shown in Figure 4.44 exhibited individual ZnO tetrapods which each pod was extended from the central part. Inset indicated selected area electron diffraction (SAED) which revealed a single-crystalline structure of the one leg of the synthesized ZnO.

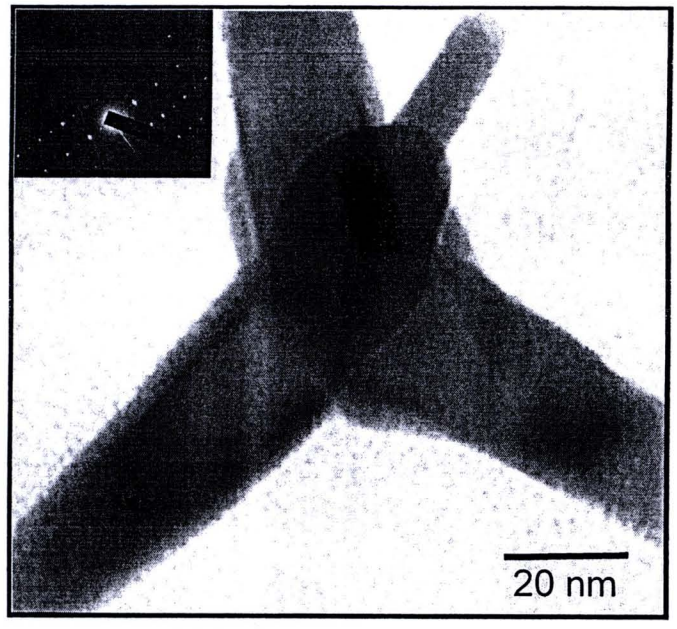

Figure 4.44 TEM image of the synthesized ZnO.

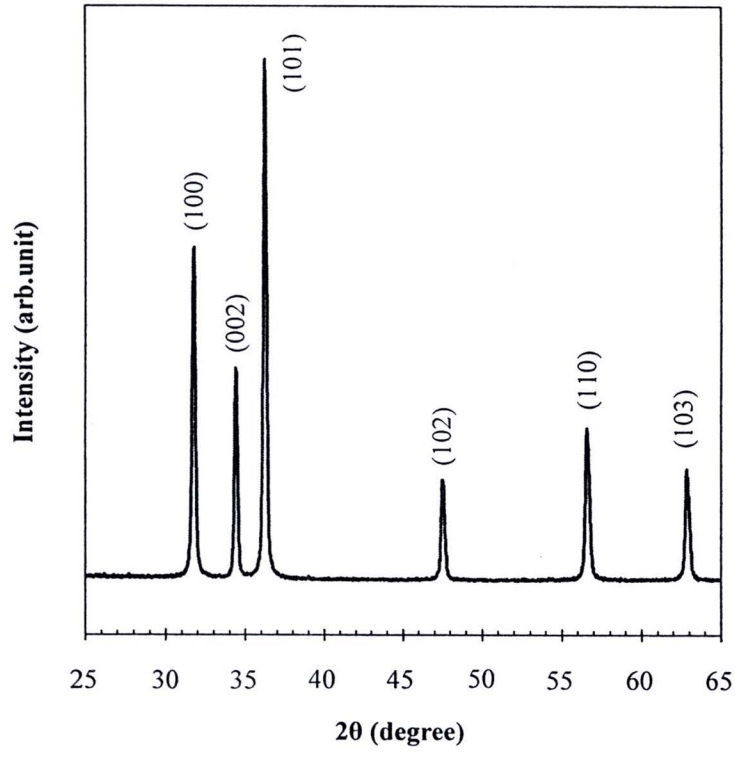

Figure 4.45 XRD pattern of the synthesized ZnO.

XRD pattern of the synthesized tetrapod ZnO was shown in Figure 4.45 which the diffraction peaks of the tetrapod ZnO were shape and narrow half width, while the peaks of other impurity phase were not found. The main peaks of the synthesized ZnO appeared at 31.8°, 34.3° and 36.2° that were typical diffraction peaks

from hexagonal ZnO planes of (100), (002) and (101), respectively. As indexed in Figure 4.42, all other peaks also matched the hexagonal ZnO structure with lattice constants of a = 3.250 Å and c = 5.207 Å. This indicated that the synthesized ZnO was composed of wurtzite structural ZnO.

4.3.4 Possible mechanisms

To explain the mechanisms for the formation of the synthesized tetrapod ZnO, the vapor-solid (VS) mechanisms was proposed which consisted of 2 stages: nucleation and growth stages.

Nucleation at the initial stage is a crucial role on the formation of the tetrapod ZnO (Xu and Sun, 2005). It was clearly seen that there was a knot in the center of the tetrapods as shown in Figure 4.44. The Zn vapor at high temperature diffused and immediately oxidized the environment of oxygen. The process of the initial nucleation was combination of diffusion, collision of atoms and reaction between the vapor molecules (including vapor Zn and O_2). When the supersaturation increase to a level at which nuclei formed, the produced ZnO nuclei grown to sizes larger than the critical size. The ZnO nuclei formed homogeneous as carried by the gas phase.

According to the octa-twin nucleus model (Takeuchi et al., 1994), ZnO nuclei formed in an environment of oxygen are octa-twin nuclei which consists of eight tetrahedral-shape crystals, each consists of three $\{11\bar{2}2\}$ pyramidal facets and one (0001) basal facet. The eight tetrahedral crystals are connected together by making the pyramidal faces contact one with another to form an octahedron. The surfaces of the octa-twin are all basal planes. An important additional condition is that every twin is of the inversion type including the polarities of the twinned crystals are not mirror-symmetric with respect to the contact plane but anti-symmetric. Therefore, the eight basal surfaces of the octa-twin are alternately the plus (0001) surface (+c) and the minus surface (-c), as shown in Figure 4.46.

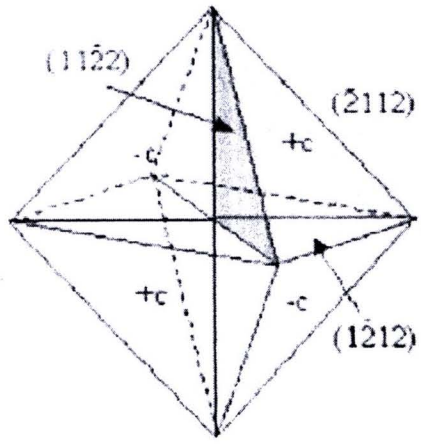

Figure 4.46 Octa-twin ZnO nuclei (Takeuchi et al., 1994)

The formation of the tetrapod structure has to do with the following two factors based on the octa-twin nucleus. It was known through the study of ZnO nanowires and nanobelts (Pan, Dai, and Wang, 2001), [0001] was the fastest growth direction in the formation of these structures. The octa-twin had 4 positive charged (0001) surfaces and 4 negative charged (0001) surfaces. The positive charged surfaces were likely to terminated with Zn, which might be favorable sites to attract vapor species, leading to the growth of whiskers along four [0001] directions.

4.4 Synthesis of the ZnO/MWCNT composites by single-step gas phase reaction

4.4.1 Investigation of thermodynamics

In this part, ZnO nanoparticles and carbon nanoparticles with iron nanoparticles inside were expected to be main compounds of the ZnO/MWCNT composites. The synthesis of the ZnO/MWCNT composites within a single-step process was more complexity than the isolated synthesis process of the ZnO nanoparticles and carbon nanoparticles. During the formation of the ZnO nanoparticles, introduced O_2 into the synthesis system was important for reacting with vaporized Zn under high synthesizing temperature. However, the introduced O_2 could possible react with the other elements including C and Fe which in form of encapsulated Fe in carbon nanoparticles. Oxidation of related elements within the synthesis system of the ZnO/MWCNT composites was carefully considered including oxidation of zinc, oxidation of carbon and oxidation of iron as shown in equation 4.22, 4.23(a)-(b), and 4.24(a)-(c), respectively.

Oxidation of zinc;

$$2Zn + O_2 = 2ZnO \tag{4.22}$$

Oxidation of carbon;

$$C + O_2 = CO_2 \tag{4.23a}$$

$$2C + O_2 = 2CO \tag{4.23b}$$

$$2CO + O_2 = 2CO_2 \tag{4.23c}$$

Oxidation of iron;

$$2Fe + O_2 = 2FeO \tag{4.24a}$$

$$\frac{3}{2}Fe + O_2 = \frac{1}{2}Fe_3O_4 \tag{4.24b}$$

$$4Fe_3O_4 + O_2 = 6Fe_2O_3 \qquad (4.24c)$$

Gibb free energy of reaction (ΔG) which is thermodynamic potential was considered for each oxidation. A negative value for ΔG indicates that a reaction can proceed spontaneously (Gaskell, 1981). Standard free energy change of oxidation (ΔG^o) of related elements at different synthesizing temperatures was revealed from Ellingham diagram as shown in Figure 4.47.

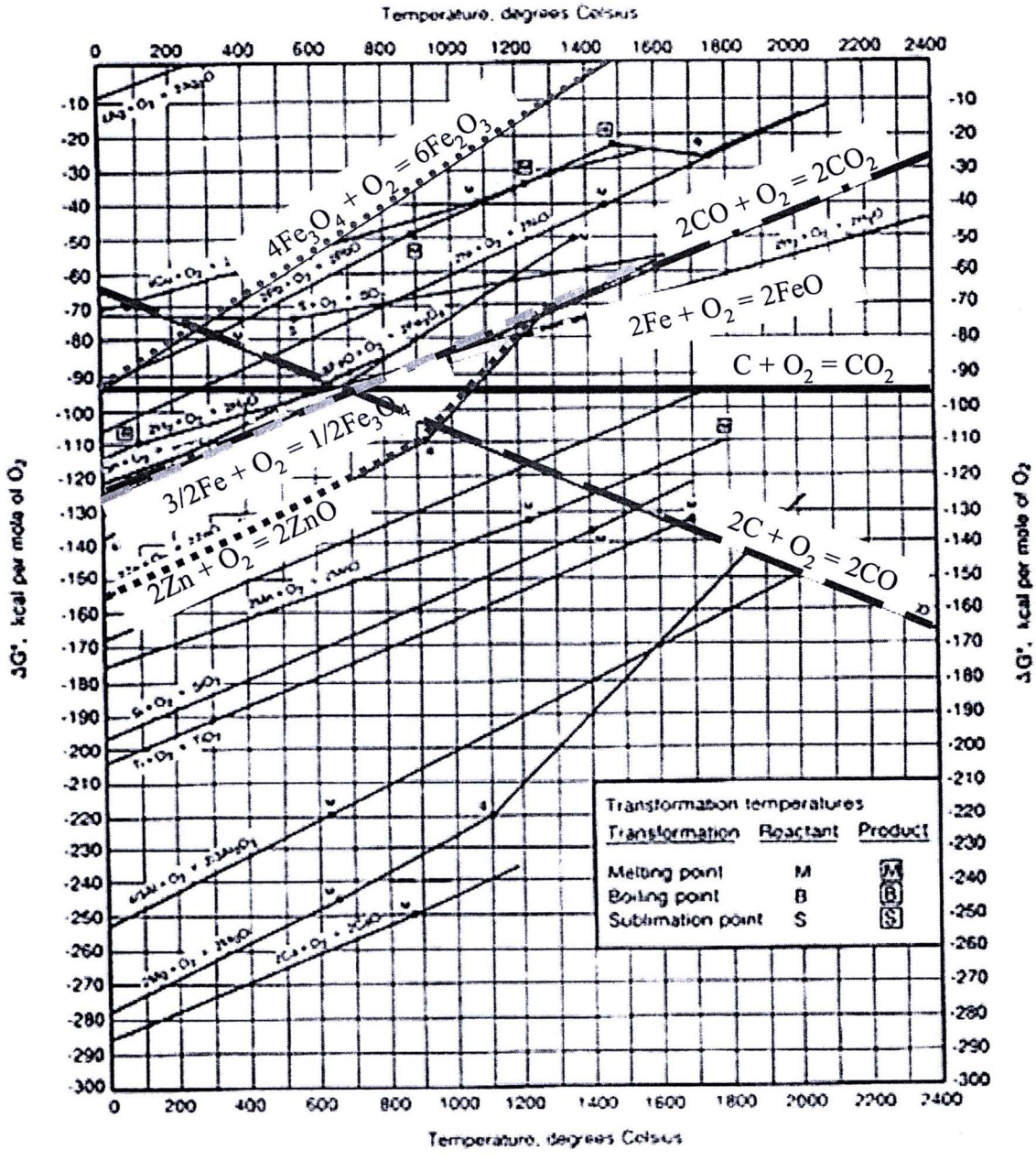

Figure 4.47 Ellingham diagram for oxides of Zn, C and Fe.
(http://www.nss.org/settlement/nasa/spaceresvol3/images/pmofld-fig33.jpg)

From Figure 4.47, it could be clearly seen negative value of ΔG° of the oxidation of Zn, C and Fe over wide ranges of the synthesizing temperature. At any synthesizing temperature, highly negative value of ΔG° shows more spontaneous reaction. Therefore, at the same synthesizing temperature, the oxidation of Zn, C and Fe could simultaneously take place within this system with different abilities. Decreasing of the synthesizing temperature commonly exhibit the highly negative value of ΔG° of oxidation. However, oxidation of CO as shown in equation 4.23b shows highly negative value of ΔG° at higher synthesizing temperature. While, complete oxidation of C as shown in equation 4.23a reveals constant negative value of ΔG° although the temperature is increased.

ΔG° of the oxidation of Zn, C and Fe at the synthesizing temperatures of 800 and 900 °C was shown in Table 4.1. It could be clearly observed that, at the synthesizing temperatures of 800 and 900 °C, the negative value of ΔG° of the Zn oxidation was the highest, leading to the oxidation of Zn could take place easily compared to the oxidation of the other elements.

Table 4.1 Standard free energy change of oxidation of Zn, C and Fe at different synthesizing temperatures

Reaction	ΔG° (kcal/mol of O_2)	
	T = 800 °C	T = 900 °C
$2Zn + O_2 = 2ZnO$	-115	-110
$C + O_2 = CO_2$	-93	-93
$2C + O_2 = 2CO$	-96	-102
$2CO + O_2 = 2CO_2$	-92	-88
$2Fe + O_2 = 2FeO$	-92	-89
$3/2Fe + O_2 = 1/2Fe_3O_4$	-92	-88
$4Fe_3O_4 + O_2 = 6Fe_2O_3$	-42	-35

The major oxidation of carbon nanoparticles could be considered into 2 reactions including complete and incomplete oxidation of carbon nanoparticles, while oxidation of CO which is sequentially reaction of the incomplete oxidation was considered as minor oxidation. At the synthesizing temperature of 800 and 900 °C, the negative value of ΔG° of the complete oxidation was the same of 93 kcal/mol. While,

the negative value of ΔG^{o} of the incomplete oxidation was higher at higher synthesizing temperature. Therefore, decrease in oxidation of carbon could be taken place by decrease in the synthesizing temperature. Because of iron nanoparticles encapsulated in the carbon nanoparticles, the oxidation of the iron nanoparticles was also taken place unavoidable after partial oxidation of the carbon nanoparticles. The oxidation of the iron nanoparticles could be initiated by 2 major oxidations as shown in equation 4.24a and 4.24b, respectively.

4.4.2 Effect of synthesizing temperature

From clues of the thermodynamic data, it could be clearly realized that, among various parameters of the synthesizing temperature, nitrogen flow rate, oxygen flow rate and glycerol to ferrocene molar ratio, the synthesizing temperature was the major parameter of this study. Therefore, in this part, the effect of synthesizing temperature on the formation of the synthesized ZnO/MWCNT composites was studied under the same condition of nitrogen flow rate and oxygen flow rate of 500 and 100 mL/min, respectively and glycerol to ferrocene molar ratio of 5 to 1. From preliminary study, it should be noted that color of products deposited at zone 3 was found to be gray color which was the combination of black color of the synthesized MWCNTs and white color of the synthesized ZnO nanoparticles. The gray color could be implied that the synthesized products might be the ZnO/MWCNT composites. Therefore, the synthesized products at zone 3 were kept and characterized and then reported and discussed in this part.

Synthesizing temperature of 800 °C

Morphology of the synthesized products at the synthesizing temperature of 800 °C was shown in Figure 4.48.

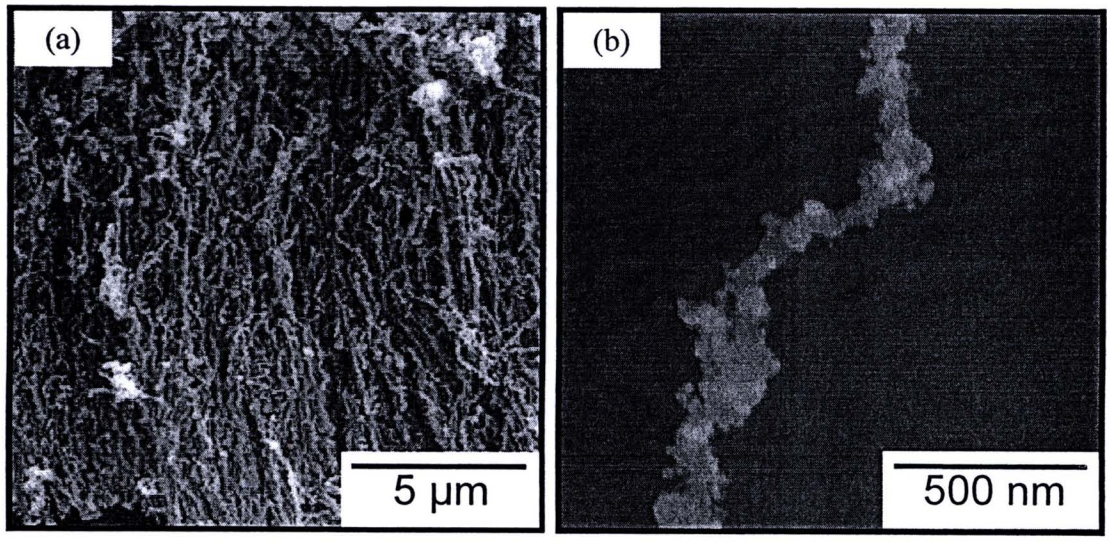

Figure 4.48 SEM images of the synthesized products at the synthesizing temperature of 800 °C.

The typical SEM images as shown in Figure 4.48(a) revealed the MWCNT bundles coated with ZnO nanoparticles. The synthesized MWCNTs exhibit relatively uniform diameter and length with a high aspect ratio. Figure 4.48(b) exhibited a highly magnified SEM image of the composites of which the estimated diameter is 60–70 nm. The coated layer on the surface of the MWCNTs consisted of a large number of much smaller ZnO nanoparticles.

Referring to the synthesized MWCNTs within the isolated synthesis of the MWCNTs (see page 62) under the same condition of the nitrogen flow rate of 500 mL/min, the synthesizing temperature of 800 °C and glycerol to ferrocene molar ratio of 5/1, the synthesized carbon nanoparticles at zone 3 were the MWCNTs with tube diameter about 50 nm. It could be clearly observed that the synthesized MWCNTs within the composite synthesis system were similarity of the tube diameter ranges.

Under the same condition of the nitrogen flow rate of 500 mL/min, the oxygen flow rate of 100 mL/min and the synthesizing temperature of 800 °C, the synthesized ZnO nanoparticles at zone 3 of the isolated synthesis system of the ZnO nanoparticles (see page 87) were tetrapod structure which their pod diameter and length were about 50-60 nm and 160-180 nm, respectively. It could be clearly observed that morphology of the synthesized ZnO nanoparticles of the composite synthesis system were significantly changed from the tetrapod structure of the isolated synthesis system into spherical structure with diameter in range of 20-30 nm.

XRD pattern of the synthesized products at the synthesizing temperature of 800 °C shown in Figure 4.49 consisted of a peak from (002) planes of hexagonal graphite structure at $2\theta = 27°$ and main peaks from (100), (002), (101), (102) and (110) planes at $2\theta = 31.8°$, 34.3°, 36.2°, 47.5° and 57.6°, respectively which corresponded to typical diffraction peaks from hexagonal ZnO with lattice constants of a = 3.250 Å and c = 5.207 Å. This indicated that the synthesized ZnO was composed of wurtzite structural ZnO. It could be clearly observed that the diffraction peaks were combination of the peak of the MWCNTs as shown in Figure 4.33 and the ZnO nanoparticles as shown in Figure 4.45. Furthermore, response of α-Fe_2O_3 was also found at $2\theta = 54.3°$. Any response of (111) plane of the face-centered cubic (fcc) γ-Fe at $2\theta = 43.7°$ and (110) plane of body-centered cubic (bcc) α-Fe at $2\theta = 44.7°$ was found in the composites. Furthermore, any orthorhombic cementite Fe_3C phase was also found in the XRD pattern. Referring to the XRD pattern of the synthesized MWCNTs as shown in Figure 4.33, it could be clearly observed that crystal phase of the Fe nanoparticles were the combination of γ-Fe, α-Fe and Fe_3C phases while the crystal phase of the Fe nanoparticles of the synthesized products within the ZnO/MWCNT composite synthesis system was α-Fe_2O_3 phase. Therefore, it could be realized that the Fe nanoparticles in γ-Fe, α-Fe and Fe_3C phases of the synthesized products within the ZnO/MWCNT composite synthesis system was oxidized into the iron form.

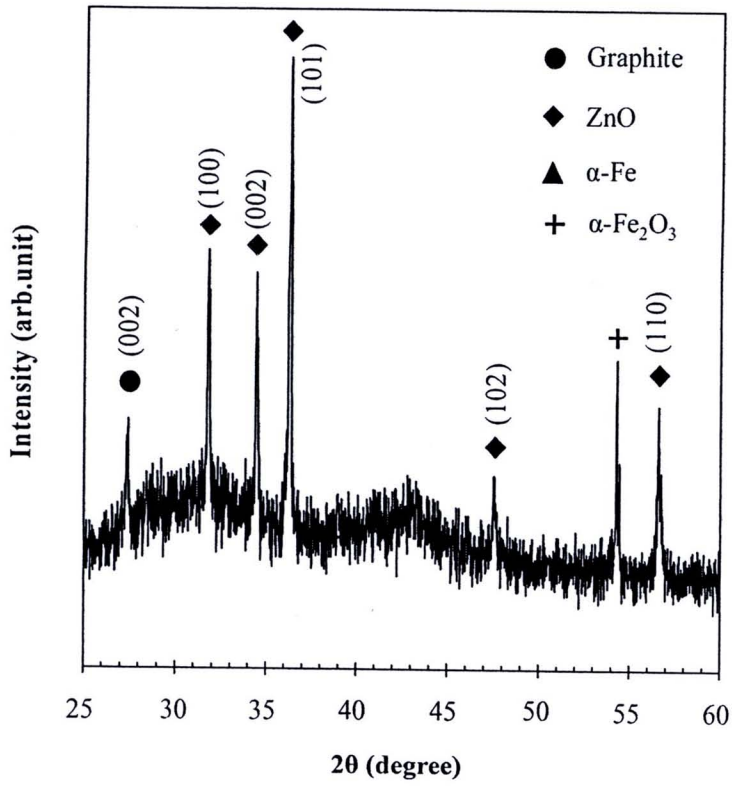

Figure 4.49 XRD pattern the synthesized products at the synthesizing temperature of 800 °C.

Synthesizing temperature of 900 °C

Morphology of the synthesized products at the synthesizing temperature of 900 °C was shown in Figure 4.50. The typical SEM image and its highly magnified SEM image as shown in Figure 4.50(a) and (b), respectively, clearly exhibited agglomerated particles with primary diameters about 100-200 nm, while any of MWCNTs was observed.

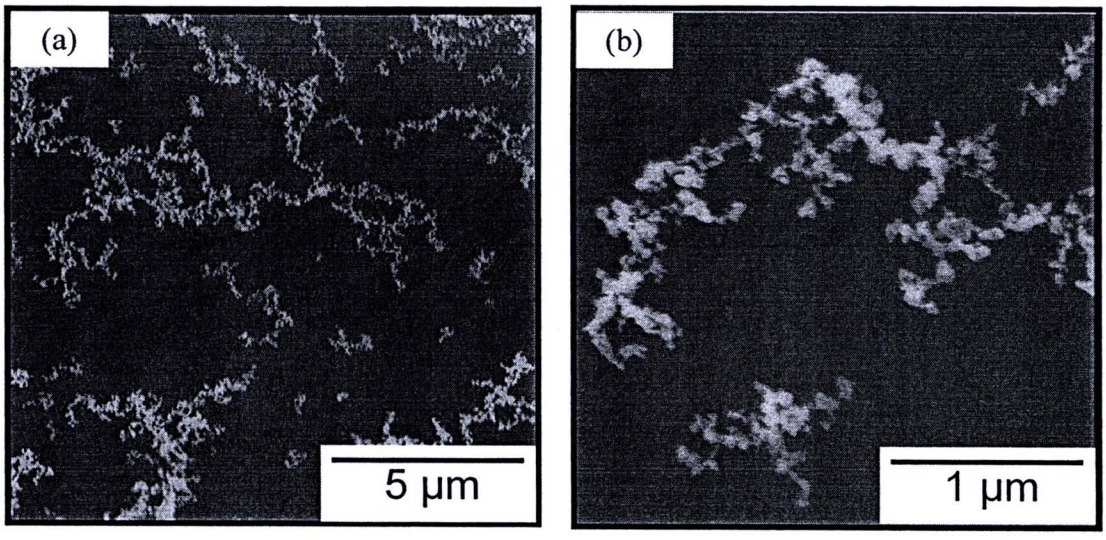

Figure 4.50 SEM images of the synthesized products at the synthesizing temperature of 900 °C.

The XRD pattern of the synthesized products at the synthesizing temperature of 900 °C was shown in Figure 4.51. It exhibited (100), (002), (101), (102) and (110) planes of the synthesized ZnO at 2θ = 31.8°, 34.4°, 36.2°, 47.4° and 57.6°, respectively which corresponded to typical diffraction peaks from hexagonal ZnO with lattice constants of a = 3.250 Å and c = 5.207 Å. This indicated that the synthesized ZnO was composed of wurtzite structural ZnO. However, it could be also observed responses of pure Zn at 2θ = 39.3° and 43.1° which could recognize non-oxidation of the vaporized Zn. Furthermore, response of α-Fe_2O_3 was revealed at 2θ = 54.3°, while pure Fe were also exhibited at 2θ = 54.3°. However, any response of C could be found which could indicate that most of carbon nanoparticles reacted with the introduced O_2.

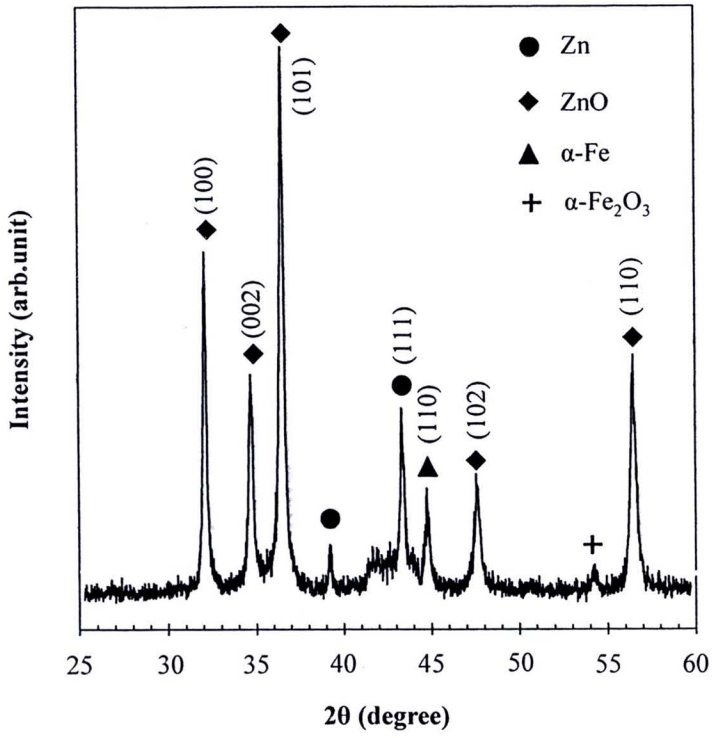

Figure 4.51 XRD pattern the synthesized products at the synthesizing temperature of 900 °C.

The experimental results exhibited that the synthesizing temperature affected on the formation of the ZnO/MWCNT composites. From the XRD patterns, both of the synthesizing temperatures, the ZnO nanoparticles were formed. However, it could be clearly seen that at the synthesizing temperature of 900 °C, extra response of Zn was observed. Referring to the isolated synthesis of the ZnO nanoparticles at the same condition of the N_2 flow rate, synthesizing temperature and O_2 flow rate of 500 mL/min, 900 °C and 100 mL/min, respectively, as reported and discussed above (see page 91), this could identify that within the composite synthesis system, amount of O_2 for reacting with Zn was lower due to competitive oxidation of C and Fe atoms as shown in Figure 4.47, leading to the amount of O_2 was not enough for the oxidation of Zn and then remains of Zn were observed.

The XRD patterns also revealed the response of C from the MWCNTs within the synthesized composites at the synthesizing temperature of 800 °C. However, the response of C was disappeared when the synthesizing temperature was increased to 900 °C. The disappeared C peak exhibited that at the synthesizing temperature of 900 °C, all MWCNTs were oxidized. Referring to Ellingham diagram as shown in Figure 4.47, the incomplete oxidation of C at higher temperature is found

to be more spontaneous due to its highly negative value of ΔG^{o}. Therefore, at the synthesizing temperature of 900 °C, the synthesized MWCNTs could be oxidized easier than those of 800 °C. Furthermore, it could be implied that the synthesizing temperature of 900 °C was too high for the formation of the ZnO/MWCNT composites. Previous work (Misra et al., 2006) revealed the burning property of the MWCNTs by using Thermal Gravimatric Analysis (TGA). There could be found that the MWCNTs were initially oxidized around 400 °C and completely oxidized at 900 °C, suggesting that at this temperature amorphous carbon was well as MWCNTs converted to gaseous form. Therefore, in this work, the disappearance of the synthesized MWCNTs within the composite synthesis system was caused by complete oxidation of the MWCNTs. After the complete oxidation of the MWCNTs at the synthesizing temperature of 900 °, the Fe nanoparticles inside the MWCNTs were exposed by surrounding O_2, leading to the formation of the iron oxide in form of α-Fe_2O_3 (Wu et al., 2009) simultaneous with the formation of the ZnO nanoparticles.

Although the XRD pattern of the synthesized composites at the synthesizing temperature of 800 °C exhibited the response of C from the MWCNTs, the compete oxidations of C and Fe unavoidably took place and simultaneously with the oxidation of Zn as shown in Figure 4.47. This could be assured by response of Fe_2O_3 which was from the oxidation of Fe. Therefore, these experimental results could inform that some of the MWCNTs were oxidized resulted in the Fe nanoparticles inside the MWCNTs were exposed to surrounding O_2 and then were simultaneous oxidized to form the iron oxide. Referring to TGA analysis as discussed above, it was well known that the MWCNTs were initially and completely oxidized around 400 and 900 °C, respectively. Therefore, at the synthesizing temperature of 800 °C, partial oxidation of the synthesized MWCNTs was occurred, leading to the appearance of the Fe_2O_3 of this work.

ZnO/MWCNT composite yield at the synthesizing temperature of 800 °C can be defined in equation 4.25.

$$\text{ZnO / MWCNT composite yield}\,(\%) = \frac{W_{\text{ZnO / MWCNT}}}{W_{\text{glycerol}} + W_{\text{ferrocene}} + W_{\text{Zn}}} \times 100 \qquad (4.25)$$

Where $W_{ZnO/MWCNT}$ = Weight of synthesized ZnO/MWCNT composites

$W_{glycerol}$ = Weight of glycerol

$W_{ferrocene}$ = Weight of ferrocene

W_{Zn} = Weight of zinc

Yield of the ZnO/MWCNT composite which were synthesized at the synthesizing temperature of 800 °C were 1.46 %.

TEM analysis of the synthesized ZnO/MWCNT composites at the synthesizing temperature of 800 °C in Figure 4.52 revealed that the ZnO nanoparticles were well attached to the MWCNT surface. The narrow size distribution of the ZnO nanoparticles with an average particle size of 20–30 nm could be obtained. This was ascribed to the growth of the ZnO nanoparticles on the outer surface of MWCNTs after the oxidation of zinc vapor which took place after the formation of the MWCNTs (Beker et al., 2002)

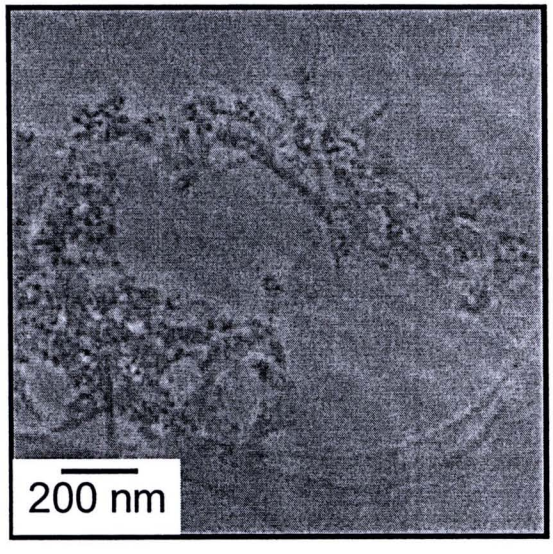

Figure 4.52 TEM image of the synthesized ZnO/MWCNT composites at the synthesizing temperature of 800 °C.

FT-IR spectrum of the synthesized MWCNT/ZnO composites at the synthesizing temperature of 800 °C was shown in Figure 4.53 which revealed surface chemistry of the MWCNT/ZnO composite. In the high frequency region, band around 3420 cm^{-1} could be assigned to the bending vibrations of adsorbed molecular water and stretching vibrations of OH groups. The peaks around 1600 cm^{-1} could be inferred as CO_2 stretching vibration. Furthermore, in the low frequency region, peak

around 500 cm^{-1} in ZnO/MWCNT composite was assigned to the Zn–O. From the FT-IR spectrum, it could be assured that the synthesized products at the synthesizing temperature of 800 °C were the ZnO/MWCNT composites.

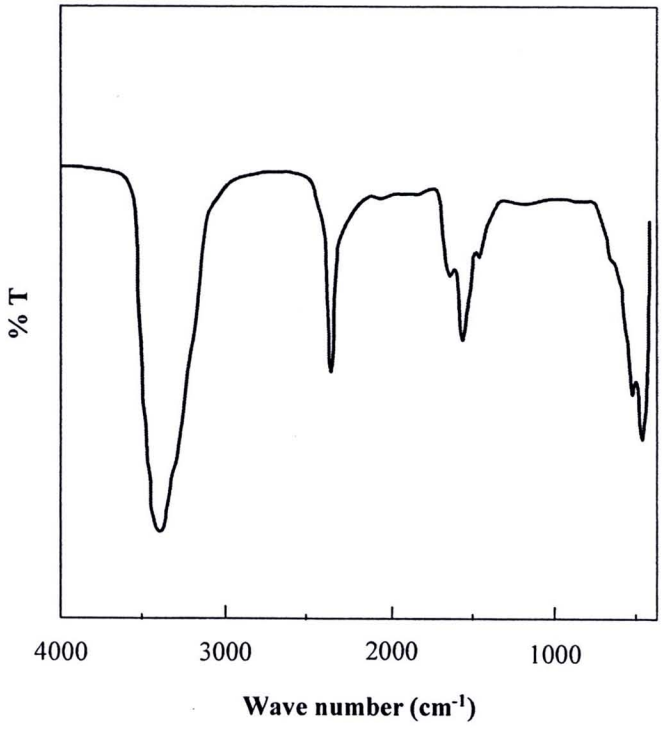

Figure 4.53 FT-IR spectrum of the synthesized ZnO/MWCNT composites at the synthesizing temperature of 800 °C.

Furthermore, elemental composition of the synthesized products at the synthesizing temperature of 800 °C was also affirmed by EDX as shown in Figure 4.54. The presence of Zn, O, Fe and C peaks could reveal the existence of the ZnO nanoparticles on the surface of MWCNTs containing Fe nanoparticles inside (Chen et al., 2005). The Cu signal originated from the copper microgrid employed for the microscopic analysis. The elemental composition of the C, O and Zn atoms within the ZnO/MWCNT composite as shown in inset was 18.27, 41.66 and 40.07 %, respectively. It could be clearly observed that atomic ratio of the Zn to O was 1.04 which could identify that all of the vaporized Zn could react with the introduced O_2 to form the ZnO nanoparticles.

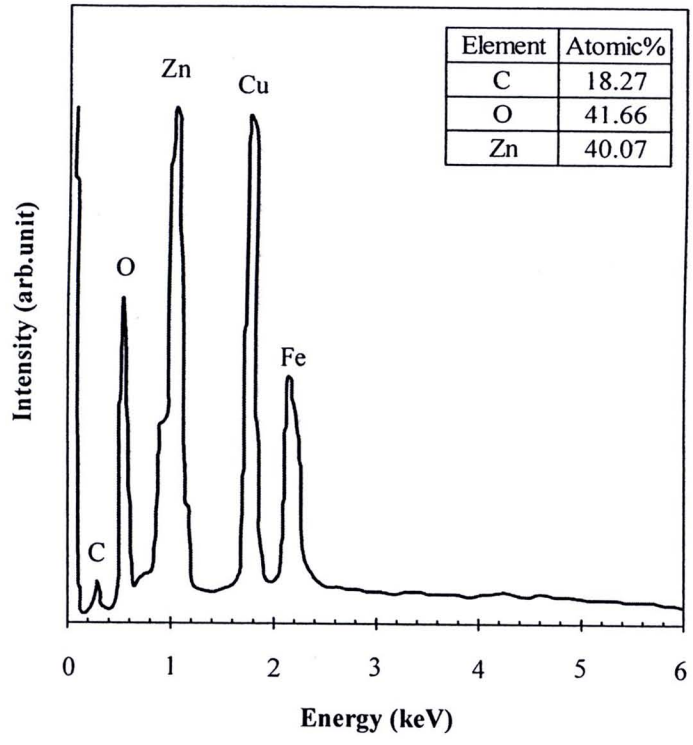

Figure 4.54 EDX pattern of the synthesized ZnO/MWCNT composites at the synthesizing temperature of 800 °C.

For comparison, the UV–vis absorbance of the synthesized MWCNTs, the synthesized ZnO and the synthesized ZnO/MWCNT composites dispersed in deionized water were depicted in Figure 4.55. In curve (a), a broad absorption peak at 262 nm was originated from the C=C structure of the synthesized MWCNTs (Chen et al, 2002). Meanwhile, the absorption peak at 368 nm in curve (b) would represent dispersion of the synthesized ZnO nanoparticles in deionized water. The absorption peak of the synthesized ZnO/MWCNT composites was dominated by the characteristic absorption of ZnO, which was observed at about 363 nm in curve (c). As light blue shift of the absorption band of the composites regarding to that of pure ZnO nanoparticles would be attributed to the quantum size effect of the synthesized ZnO nanoparticles.

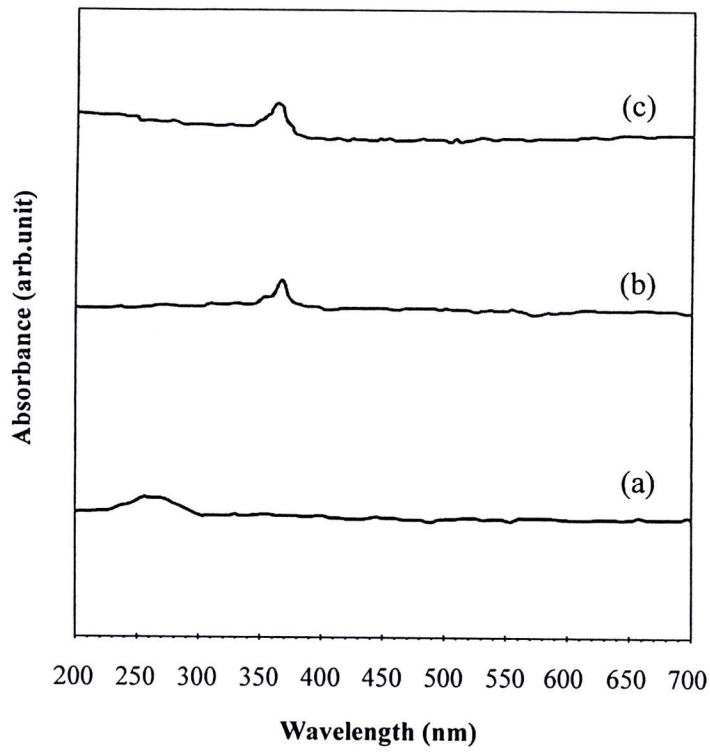

Figure 4.55 UV–visible absorbance of the samples in distillation water: (a) the synthesized MWCNTs, (b) the synthesized ZnO and (c) the synthesized ZnO/MWCNT composites.

4.4.3 Possible Mechanisms

Based on experimental results, it could be ascribed to the formation of the ZnO nanoparticles on the outer surface of MWCNTs after the oxidation of zinc vapor which took place after the formation of MWCNTs as shown in Figure 4.56.

The possible mechanisms, proposed here, were believed that, at the synthesizing temperature of 800 °C, the MWCNTs which were synthesized firstly were surrounded by Zn vapor and O_2. Zn vapor was then oxidized by O_2 to form ZnO nanoparticles, while most of the MWCNTs were not oxidized, leading to appearance of the MWCNTs surrounded with ZnO nanoparticles. Finally, attachment of the ZnO nanoparticles on the outer surface of the MWCNTs was occured. The formation of the composites of ZnO nanoparticles and MWCNTs were formed.

At the synthesizing temperature of 900 °C, the possible mechanisms were proposed that the synthesized MWCNTs which were surrounded by Zn vapor and O_2 were oxidized by O_2 simultaneously with the oxidation of Zn vapor, leading to

complete disappearance of the MWCNTs. Iron catalytic nanoparticles inside the MWCNTs were then exposed to surrounding O_2 and oxidized to form α-Fe_2O_3 nanoparticles. Because of competition of the oxidation of Zn nanoparticles, MWCNTs and Fe nanoparticles, the introduced O_2 were not enough for remaining Zn. Therefore, some of Zn vapor were not used for the formation of ZnO nanoparticles. Finally, the ZnO nanoparticles, Zn nanoparticles and Fe_2O_3 nanoparticle were agglomerated each other to form agglomerated nanoparticles.

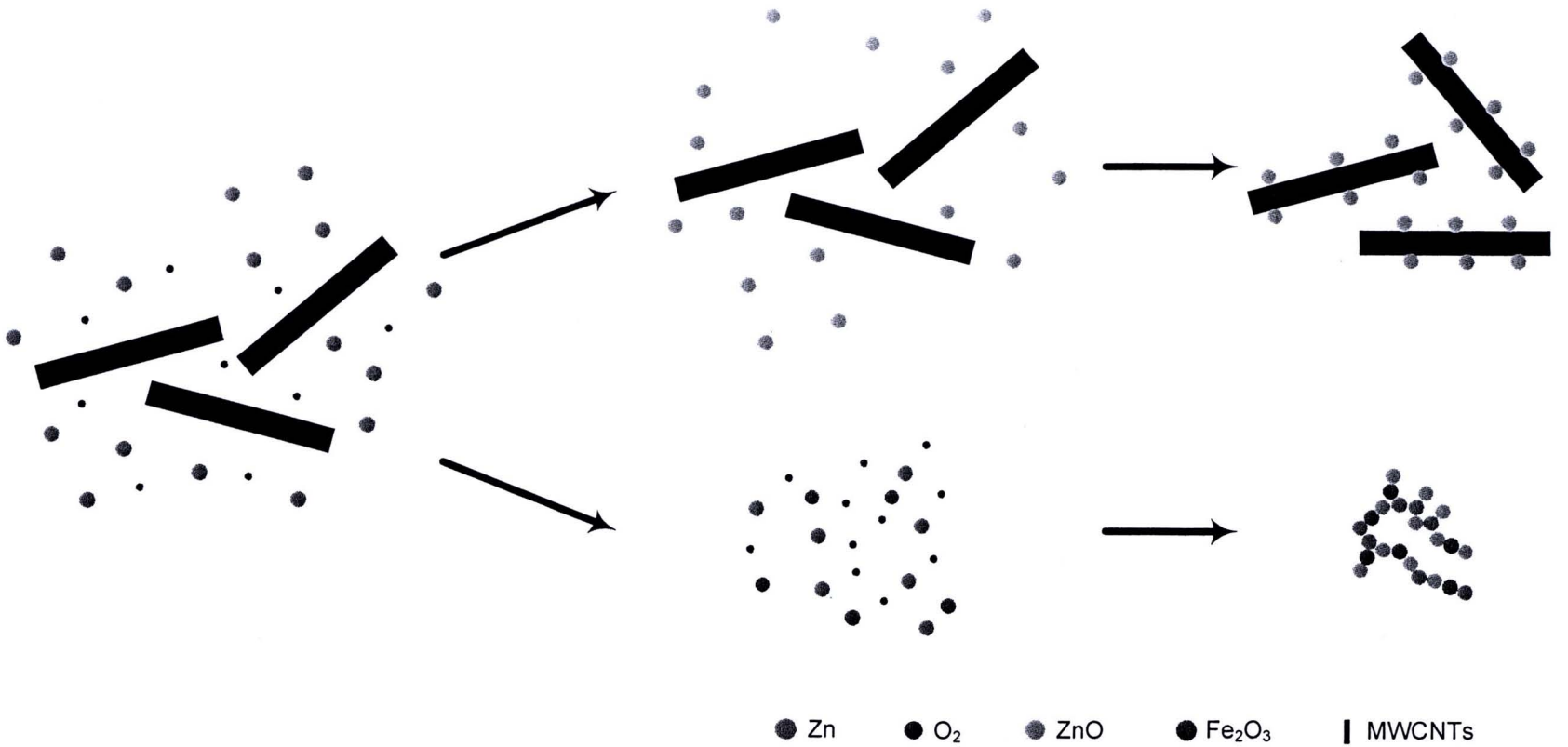

Figure 4.56 Possible mechanisms of the ZnO/MWCNT composites.